

**University of Alberta**

Laser Acceleration of MeV to GeV Electrons

by

Navid Vafaei-Najafabadi

A thesis submitted to the Faculty of Graduate Studies and Research  
in partial fulfillment of the requirements for the degree of

Master of Science  
in  
Photonics and Plasmas

Department of Electrical and Computer Engineering

©Navid Vafaei-Najafabadi  
Fall 2010  
Edmonton, Alberta

Permission is hereby granted to the University of Alberta Libraries to reproduce single copies of this thesis and to lend or sell such copies for private, scholarly or scientific research purposes only. Where the thesis is converted to, or otherwise made available in digital form, the University of Alberta will advise potential users of the thesis of these terms.

The author reserves all other publication and other rights in association with the copyright in the thesis and, except as herein before provided, neither the thesis nor any substantial portion thereof may be printed or otherwise reproduced in any material form whatsoever without the author's prior written permission.

## **Examining Committee**

Robert Fedosejevs, Electrical and Computer Engineering

Ying Tsui, Electrical and Computer Engineering

Wojciech Rozmus, Physics

*To my parents, who made the right decisions at the right times*

# Abstract

In this thesis electron generation is studied via laser plasma interaction known as laser wakefield acceleration in two regimes of weakly relativistic and highly relativistic laser intensity regimes. The plasma targets consisted of gas jets photonized by rising edge of the laser pulse to densities as high as  $10^{20}\text{cm}^{-3}$ . In the weakly relativistic regime, 210 mJ at 33 fs were focused to intensities of up to  $3 \times 10^{18}\text{Wcm}^{-2}$  on the gas targets of 2.4 mm length. In the highly relativistic regime, 3 J of energy compressed in 30 fs were delivered at intensity as high as  $6.5 \times 10^{18}\text{Wcm}^{-2}$  on targets of 2.4, 5, and 10 mm. Monoenergetic electrons in tens of MeV were observed in weakly relativistic regime, while electron energies as high as 300 MeV were observed in highly relativistic regime. Higher input laser intensity and prepulse levels were found to enhance electron production. Scaling of energy and stability of electron generation were also studied.

# Acknowledgements

The author gratefully acknowledges the technical support from Blair Harwood, the machine shop and the nanofabrication facility of the Electrical Computer Engineering Department of the University of Alberta. Particular appreciation is due to Herbert Dixel and the nanofab training staff. This work could not have been completed without the help of the great staff at the INRS, particularly Sylvain Fourmaux and Stphane Payeur who operated the 200 TW laser, Mark O. the technician for 200 TW system, and Antoine Laramée and Francois Poitras who were the technical staff of the 10 TW system. Additionally, significant contributions by Atif Ali to the experiments are acknowledged. I would also like to gratefully acknowledge my supervisor Dr. Fedosejevs for the opportunity to do research in the field of laser acceleration of electrons, which in Canada is only possible to do under his supervision. Moreover I would like to acknowledge Dr. Rozmus and his group at the Department of Physics for carrying out instructive simulations for the work presented.

On a personal level, I would like to thank Joshua Allen for fruitful discussion on computer programs and algorithms and other members of our household as well as my parents for their unflinching help and support during all stages of my life through graduate school.

Finally financial support from the Natural Sciences and Engineering Research Council of Canada and the Canadian Institute for Photonic Innovations is gratefully acknowledged.

# Contents

<b>1</b>	<b>Introduction</b>	<b>1</b>
<b>2</b>	<b>Theory</b>	<b>5</b>
2.1	Plasma Wake . . . . .	6
2.2	Laser Guiding . . . . .	9
2.2.1	Relativistic Optical Guiding . . . . .	11
2.2.2	Ponderomotive Self Channelling . . . . .	12
2.3	Electron Injection . . . . .	14
2.3.1	Wavebreaking Injection . . . . .	14
2.3.2	Ionization Injection . . . . .	16
2.3.3	Other Methods of Injection . . . . .	19
2.4	Acceleration Limiting Parameters . . . . .	20
2.4.1	Pump Depletion Length . . . . .	21
2.4.2	Dephasing Length . . . . .	22
2.5	Energy Gain . . . . .	23
2.6	Interferometry . . . . .	24
2.7	Electron Energy Spectrometer . . . . .	28
<b>3</b>	<b>Experimental Setup</b>	<b>31</b>
3.1	10 TW System . . . . .	31

3.1.1	Laser . . . . .	31
3.1.2	Targets . . . . .	34
3.1.3	Electron Diagnostics . . . . .	37
3.2	200 TW System . . . . .	37
3.2.1	Laser . . . . .	37
3.2.2	Gas Jet Targets . . . . .	39
3.2.3	Passive Waveguide Targets . . . . .	43
3.2.4	Output Mode Monitor . . . . .	46
3.2.5	New Electron Spectrometer . . . . .	47
3.2.6	Other Diagnostics . . . . .	50
<b>4</b>	<b>Results and Discussion of 10 TW Experiments</b>	<b>52</b>
4.1	The Prepulse Effect . . . . .	53
4.2	Longer Focal Length Parabola . . . . .	58
<b>5</b>	<b>Results and Discussion of 100 TW Experiments</b>	<b>63</b>
5.1	Electron Energy Calculation . . . . .	63
5.2	2.4 mm Gas Jet Results . . . . .	65
5.3	5 mm Gas Jet Results . . . . .	73
5.3.1	Electron Features Using Helium Gas Jet . . . . .	74
5.3.2	Electron Trends for Electron Produced by Helium Targets	83
5.3.3	Mixed Gas and Nitrogen Results . . . . .	91
5.3.4	Laser Guiding . . . . .	95
5.3.5	Other Features to be Further Investigated . . . . .	98
5.4	10 mm Gasjet Results . . . . .	101
5.5	10 mm Passive Capillary . . . . .	101
<b>6</b>	<b>PIC Simulations</b>	<b>105</b>

<b>7 Conclusions</b>	<b>114</b>
<b>Bibliography</b>	<b>118</b>
<b>Appendix</b>	<b>130</b>
<b>A Waveguide Fabrication Process</b>	<b>130</b>
<b>B Electron Trends in Individually Grouped Parameters</b>	<b>135</b>
<b>C Shot Conditions of All Figures Used in Chapter 5</b>	<b>140</b>

# List of Figures

2.1	A schematic view of the Mach-Zhender interferometer . . . . .	25
2.2	The laser probe traverses a circularly symmetric target such as a gas jet . . . . .	26
2.3	Electron deflection follows an arc in the magnetic field and a line after them. . . . .	29
3.1	The schematic diagram of the typical experimental setup and vacuum chamber used in the 10TW experiments . . . . .	32
3.2	The curves from the frequency doubling experiment and autocor- relator measurement . . . . .	35
3.3	(a) shows the density contour of the 2.4 mm nozzle as determined by interferometry and (b) the super Gaussian fit to the data . . .	36
3.4	The schematic view of the conical gas jet nozzles used in the experiments. The 2.4 mm nozzle could produce electron density as high as $10^{20}\text{cm}^{-3}$ . . . . .	40
3.5	The gas network used for mixed gas experiments . . . . .	42

3.6	Passive waveguide gas feeding structure. The common design cell is shown in (a) where gas flows in the capillary along the route indicated by arrows. The white space indicates the channel and the circle at the center indicates where gas is introduced to capillary. The cross section of the gas feeder apparatus is shown in (b). Gas enters the capillary through one hole while the other is sealed to the glass with a plastic o-ring . . . . .	44
3.7	A series of waveguides on 4" long substrates were produced using nanofabrication methods . . . . .	45
3.8	The output mode monitor setup . . . . .	46
3.9	Schematics of the new electron spectrometer . . . . .	48
3.10	The electron deflection on the back Linac calculated for different number of magnets. . . . .	49
4.1	Third order autocorrelator measurement of ALLS laser system . . . . .	54
4.2	Examples of prepulse signals observed during the experiments. (a) and (b) show nanosecond foot and the main laser pulse for two different shots, where the level of prepulse was increased in (b). (c) shows an example of femtosecond prepulse . . . . .	55
4.3	Contour plots of electron densities of preionized channels created by prepulses. A peak intensity of $1 \times 10^{14} \text{Wcm}^{-2}$ is assumed for the prepulse. The plots are made using MPI rates for Helium (bottom) and Nitrogen (top) at backing gas pressure 1000 psi for both. The x-axis is distance along the axis of the laser with zero being at the center of the nozzle and y-axis is the transverse distance from nozzle surface. The laser is incidental from the right and is focused at 1.3 mm . . . . .	56

4.4	An electron spectra obtained with prepulse contrast of $2 \times 10^{-5}$ with helium at 1100 psig ( $n_e \sim 4.6 \times 10^{19}$ ) . . . . .	57
4.5	Time resolved interferograms of 6 TW pulse using a 15 cm focal length parabola and Helium gas at 1000 psi, with fspp intensity contrast of $\simeq 5 \times 10^{-6}$ . The interferograms are recorded from 7.7 ps before the pulse arrives to 8 ps after. The preplasma generated is indicated with a circle in the frame for t=-7.7 ps . . . . .	59
4.6	Examples of monoenergetic and Maxwellian electron shots with nitrogen at 1000 psi $n_e \sim 1.8 \times 10^{20}$ and high prepulse . . . . .	62
5.1	The data from the 2.4 mm gas jet and peak laser power of 77 TW	66
5.2	Parameters of laser wakefield acceleration according to theory . .	67
5.3	Example of top emission for 2.4 mm gas jet at $n_e = 2.1 \times 10^{19} \text{cm}^{-3}$ (shot 100302.74). The laser enters from the lower right and propagates forward towards the top left. All three images belong to the same shot . . . . .	68
5.4	Top emission images for 2.4 mm gas jet (a) for different densities and (b) for several shots for the same density. Axis of propagation is shown in Fig. 5.3c . . . . .	70
5.5	The PMT value recorded in electron density and electron bunch energy space are plotted. Electron bunch energy of -100 MeV denotes Maxwellian spectrum for electrons . . . . .	72
5.6	Example spectrum of electron signals using a nozzle with exit diameter of 2.4 mm. (a) is shot 100302.74 and (b) is shot 100302.77. $n_e = 2.1 \times 10^{19} \text{cm}^{-3}$ for both shots and peak laser power is 77 TW	73

5.7	Commonly observed types of electron signals. (a) and (b) show monoenergetic signals. (c) shows a signal with two peaks and (d) shows monoenergetic spots superimposed on quasi-Maxwellian. Peak laser power is 77 TW and estimated electron density was about $5 \times 10^{18} \text{cm}^{-3}$ . The electrons go through the mid Lanex screen before being dispersed by magnets . . . . .	75
5.8	Horizontal plots for the commonly occurring electron features. (a), (b), (c), and (d) are horizontal outlines of 5.7a, 5.7b, 5.7c, and 5.7d respectively . . . . .	76
5.9	Two rare shots with faint signal at high energy and prominent lower energy spot. (a) and (b) are high brightness images. (c) and (d) are low brightness images of (a) and (b) respectively. (c) and (d) have the same settings. (e) and (f) show vertical profiles of high energy and low energy features normalized to one and superimposed . . . . .	78
5.10	X-ray shadows. (a) shows betatron radiation. (b) shows Bremsstrahlung radiation from Lanex screen and glass wedge in electrons path. (c) and (d) are horizontal lineouts of (a) and (b) respectively . . . . .	79
5.11	100316_42. (a) shows a high brightness image and (b) the same image with decreased brightness. The vertical profiles for high and low features are plotted in (c) . . . . .	82
5.12	Average of electron energies with changing density (left column) and focus depth (right column). Rows one, two, and three belonging to 100309, 100310, 100316 respectively. The equation for each curve fit to the data is in each image's caption. . . . .	86

5.13	Theoretical estimates of variables as functions of electron density. (a) shows plasma wavelength in black circles, dephasing length in red squares and depletion length in green symbols. plasma wavelength is read from the right vertical axis while depletion and dephasing length values are read from the left axis. (b) shows the maximum electron energy from theoretical estimates at different densities . . . . .	87
5.14	Exit plane images with 5 mm gas jet nozzle for consecutive shots on 100316. These images show some prominent features on the edge of the beam in addition to their central feature . . . . .	90
5.15	Example of several shots of mid Lanex which had multiple electron signatures, taken on the same day as 5.14 . . . . .	91
5.16	Percentage of monoenergetic and quasi-Maxwellian shots on 100309, 100310, and 100316 shown in rows 1, 2, and 3 respectively. Left column shows the percentage as a function of estimated electron density and right column as a function of focus depth . . . . .	92
5.17	Electron energies with mixed gases and 5 mm nozzle. The focus depth of each shot is written next to its data point. the 10% nitrogen curve (the green curve) is exclusively taken at $fd = 2.5mm$	94
5.18	Output monitor images for varying laser energy with $n_e = 3 \times 10^{18}cm^{-3}$ . . . . .	96
5.19	This figure shows that the ring effect is dependent on the nature of the initial beam. . . . .	100

5.20	100317 10 mm gas jet data. (a) and (b) show the average electron energy as functions of electron density (left) and focus depth (right). (c) and (d) show the percentage of shots yielding monoenergetic (black circles) or quasi-Maxwellian spectrum (red squares) as functions of electron density (left) and focus depth (right)	102
5.21	Laser modes at the output of the interaction from the waveguides at different backing pressures of He gas for a pulse power of 77 TW	103
6.1	Results of Simulation 1. The top and bottom figures show snapshots of electron density contour and the electron energy spectra after laser has travelled 910 microns	107
6.1	Results of Simulation 1 continued. The top and bottom figures show snapshots of electron density contour and the electron energy spectra after laser has travelled 1730 microns	108
6.1	Results of Simulation 1 continued. The top and bottom figures show snapshots of electron density contour and the electron energy spectra after laser has travelled 2400 microns	109
6.2	Results of Simulation 2. Fig. (a) shows the significant growth of the bubble as it propagates about 700 microns from $x=400$ to $x=1100$ microns (b) shows the spot size reduction by nearly a factor of two in 300 microns of propagation	111
6.3	Results of Simulation 2: Fig. 6.3a shows reappearance of the ring structure as the pulse keeps evolving and 6.3b shows two samples of electron energy spectra at two different times.	112
6.4	An example of electron density spectra which shows evidence of continuous injection. Shot 100310_110 (side Lanex screen), with estimated electron density $7 \times 10^{18} \text{cm}^{-3}$	113

A.1	Schematic outline of nanofabrication process used in digging gas path for capillaries into glass . . . . .	133
A.2	Rising edge of glass channel after 100 micron was etch into the glass; dated 091207 . . . . .	134
B.1	Average electron density for 5 mm gas jet as a function of electron density for 100309, 100310, 100316 from top to bottom . . . . .	136
B.2	Average electron density for 5 mm gas jet as a function of focus depth for 100309, 100310, 100316 from top to bottom . . . . .	137
B.3	Total number of shots for 100317 as a function of electron density (left) and focus depth (right) . . . . .	138
B.4	Total number of shots for different days. The graphs for 100309, 100310, 100316 are shown from top to bottom. Figures on the left are plotted as a function of estimated electron density and on the right are plotted as focus depth . . . . .	139

# List of Tables

3.1	The measured FWHM of the focal spot (Horizontal $\times$ Vertical) on various experimental days. This variation lead to having different average values of intensities and $a_0$ on different days . . . . .	38
3.2	Gas jet nozzles dimensions and calculated densities for the nozzles used in the experiments. In electron density calculation, the ionization states of nitrogen and helium are assumed to be +5 and +2 respectively . . . . .	41
5.1	Magnetic configuration used in different days including maximum error due to presence of slit. $\Delta x_{space}$ is the distance of the last magnet from the back Lanex screen. See sections 2.7 and 3.2.5 . . . . .	64
5.2	The distribution of different behaviours of electron bunches according to their energies . . . . .	72
5.3	Energy of monoenergetic signals using nitrogen as the only target gas . . . . .	95
5.4	Values of matched spot size for powers used during the experiment with a vacuum focal spot of $30 \times 35\mu\text{m}$ horizontal and vertical FWHM and $\lambda_p = 18\mu\text{m}$ . . . . .	97
6.1	Parameter for simulations . . . . .	106

C.1 Conditions for different shots during the 100 TW experiment . . 141

# Nomenclature

$\delta\phi$	Phase shift
$\Delta n_c$	Critical channel depth
$\epsilon_n$	Normalized emittance
$\eta_r$	Index of refraction
$\gamma$	Lorentz factor for electrons in plasma
$\gamma_p$	Lorentz factor for wake's phase in 1D
$\lambda$	Laser wavelength
$\lambda_p$	Plasma wavelength
$\omega$	Laser frequency
$\omega_0$	relativistic gyration frequency of electrons
$\omega_p$	Plasma frequency
$\Phi$	Electrostatic potential
$\phi$	Normalized electrostatic potential
$\rho$	Molecular density, used for gases

$\tau$	Laser duration at FWHM
$\varepsilon$	Laser energy
$A$	Vector potential
$a$	normalized vector potential
$a_0$	Laser strength parameter, peak amplitude of normalized vector potential
$c$	Speed of light in vacuum
$D_{crit}$	Critical diameter of conical gas nozzle
$D_{exit}$	Exit diameter of conical gas nozzle
$E$	Electric field amplitude in wakes
$e$	Electron charge
$E_0$	Cold nonrelativistic wave breaking field
$E_L$	Peak laser electric field
$F_p$	Ponderomotive force
$I$	Peak laser intensity
$k$	Laser wavenumber
$L$	Pulse length
$L_d$	Dephasing length
$L_{pd}$	Pump depletion length
$m_e$	Electron rest mass
$n_0$	Uniform (initial) plasma density

$n_e$	plasma density
$P$	Laser power
$p$	momentum
$P_c$	Critical power for self focusing
$r_0$	vacuum spot size
$r_e$	Classical electron radius
$r_s$	Laser spot size
$v_{etch}$	Etch rate for the front of laser pulse
$v_{Np}$	Nonlinear phase velocity of the wake
$W$	Maximum energy gain
$Z_R$	Rayleigh length
ASE	Amplified stimulated emission
fspp	femtosecond prepulse
FWHM	Full Width at Half Maximum
LBNL	Lawrence Berkeley National Laboratory
PIC	Particle in Cell
PMT	Photomultiplier
SHG	Second harmonic generation

# Chapter 1

## Introduction

Laser wakefield acceleration, first proposed in 1979 [1], is a process where a high energy monoenergetic electron bunch can be generated from the interaction between a high intensity short duration laser pulse and an under dense plasma medium. At the time the authors proposed this method, high intensity short pulse lasers required for these experiments were not available. With the advent of chirped pulse amplification [2], laser systems with tens of terawatts of power started to become available in the laboratories. In their pioneering work in 2004, references [3, 4, 5] reported electron beams up to 170 MeV with low divergence and very small energy spread (less than three percent) from intense laser-plasma interaction in underdense plasma. Since then there has been a flurry of studies in this field by many groups with the best results todate achieved by a 2006 experiment at the Lawrence Berkeley National Laboratory (LBNL) where electron bunches with 1 GeV energy and 2.5% rms spread in energy were generated by a 40 TW peak power laser pulse guided over 33 mm in an electrically ionized plasma channel [6].

Conventionally such electron beams are generated in a linear accelerator

using large oscillating radio frequency electric fields. Plasma accelerators are of great interest because they can generate very high acceleration gradients. The accelerating gradients in the conventional radio frequency linear accelerators are limited to 100MV/m, due to the breakdown that occurs at the walls. This is not the case in the plasma accelerators since the plasma is already ionized. In cold nonrelativistic plasma limit For example, a plasma with density of  $n_e = 10^{18}\text{cm}^{-3}$  can support electric fields as high as  $E_0 \simeq 100\text{GV/m}$  [7]. As a result, the Stanford Linear Accelerator takes 3.2 km to accelerate electrons to 50 GeV of energy, compared to 1 GeV in 33 mm attained at LBNL [6].

The intense laser pulse drives a travelling plasma wave which travels at the same phase velocity as the laser pulse's group velocity in plasma. Regions of high and low electron density are the wave's crests and troughs respectively. An electron can be accelerated by being injected in the appropriate phase of the wave where the electric field pushes in the direction of wave travel. As electrons gain momentum from the wave, their velocity eventually surpasses that of the plasma wave's. Presently electrons reach their maximum energy and subsequent travel of the electrons lead to outrunning the accelerating phase of the wave and entering a region of the plasma where the wave's electric field acts against their motion. Under the right circumstances then, this process generates a high charge electron bunch with a very short duration (10's fs [8]) and few percent energy spread, or in other words a monoenergetic electron beam.

Once the technology for staging these accelerators has been developed, electron energies of multi hundred GeV or TeV (tera-electron-volts) can be generated in less than a km real estate, making studies of fundamental particle physics more readily available. Obtaining an electron bunch of such energy will lead to creation of a new generation of scientific tools and enable significant new advances. Having a monoenergetic energy distribution, ultrashort duration, and

low spatial spread, a new generation of laser plasma based radiation sources tunable from X-ray to THz frequencies will be available using magnet arrays of different undulator spacing. For instance, coherent soft X-rays with wavelength of 3 nm could be generated from 1 GeV electrons in a magnetic field undulator of about 3 meters in length [9]. Such tunable ultrashort radiation sources may be used for medical imaging and radiotherapy in medicine, or ultrafast probing experiments in chemistry. Finally, the physics of generation, propagation, and energy deposition of electron beams could contribute to fast ignition fusion research, a new technique to enhance proposed laser fusion energy schemes.

This thesis' aim is to explore acceleration of electrons in laser wakefield and parameters related to it in two particular laser power regimes of 10 and 100 TW. The experiments were carried out at the Advanced Laser Light Source (ALLS) lab of Institut National de la Recherche Scientifique (INRS) which has recently completed the construction of the upgraded 200TW laser, used for the latter part of the experiments. Of particular interest in the experiments were scaling of electron energy with different factors, ability of plasma to guide the laser pulse over the length of the interaction, and the possibility of using mixed gases to improve the quality of electron bunches.

The rest of the chapters are as follows: Chapter 2 is dedicated to the theory of laser wakefield acceleration. Parameters related to wake generation and trapping and acceleration of electrons, will be described. Additionally, the theory for interferometry and electron spectrometer are provided. Chapter 3 describes the experimental setup in detail. This will include laser and target systems as well as the diagnostic setups. A brief discussion of results obtained with the 10 TW system will be given in Chapter 4. Chapter 5 will present the discussion of results obtained with the 100 TW system in detail. Finally, results of Particle in Cell simulations, which were carried out by the plasma group in the Physics

Department, will be presented in Chapter 6.

## Chapter 2

# Theory

Laser wakefield acceleration is the process by which a short duration electron bunch could be trapped and accelerated in a plasma wake with the aid of an ultra short laser pulse. The laser pulse drives a wake whose amplitude increases as the pulse propagates due to nonlinear effects. Electrons get trapped in this wake and accelerate until they outrun the pulse or the pulse runs out of energy. The aim of this chapter is to convey a theoretical understanding of the underlying physics of these processes.

An important parameter in the discussion of the high intensity laser plasma interaction is the laser strength parameter,  $a_0$ . This parameter is the peak amplitude of the normalized vector potential of the laser field, noting that the normalized potentials are defined as

$$\phi = e\Phi/m_e c^2 \tag{2.1}$$

for the normalized electrostatic potential and

$$\mathbf{a} = e\mathbf{A}/m_e c^2 \tag{2.2}$$

for the normalized vector potential. Electric and magnetic fields are defined as  $\mathbf{E} = -\partial\mathbf{A}/\partial ct$  and  $\mathbf{B} = \nabla \times \mathbf{A}$ . In these equations, as in all to follow, bold letters indicate vector quantities. The laser strength parameter,  $a_0$ , can be related to peak intensity and power of a linearly polarized Gaussian laser beam with the normalized vector potential  $\mathbf{a} = a_0 \exp(-r^2/r_0^2) \cos(kz - \omega t)\mathbf{e}_x$  [7]:

$$\begin{aligned} a_0 &= (2e^2\lambda^2 I/\pi m_e^2 c^5)^{1/2} \\ &\simeq 8.6 \times 10^{-10} \lambda[\mu\text{m}] I^{1/2}[\text{W}/\text{cm}^2] \end{aligned} \quad (2.3)$$

$$P[\text{GW}] \simeq 21.5(a_0 r_0/\lambda)^2 \quad (2.4)$$

where  $r_0$  is the 1/e spot radius at focus and  $\lambda$  is the laser wavelength. furthermore, the peak laser electric field is given by  $E_L[\text{TV}/\text{m}] \simeq 3.2a_0/\lambda[\mu\text{m}]$ .

Physically  $\mathbf{a} = \mathbf{p}_\perp/m_e c$  is the normalized transverse "quiver" momentum for the electrons in the laser field, as indicated by the conservation of the transverse canonical momentum in 1-D limit  $r_0 \gg \lambda$ . This equation implies that for relativistic electron motion (i.e.  $|p| \sim m_e c$ ),  $a_0$  has to be greater than one. In other words,  $I \geq 10^{18} \text{ W}/\text{cm}^2$  for wavelengths near  $1\mu\text{m}$

## 2.1 Plasma Wake

A plasma wake is a longitudinal electron wave in the plasma which is generated by the ponderomotive force. This is a generalized force of the laser acting on the plasma, distinct from the quiver motion of single electrons induced by the laser field. In the 1D linear limit for example, this force is defined as  $\mathbf{F}_p = d\delta\mathbf{p}/dt$  where  $\delta\mathbf{p}$  is defined as a difference between the fluid element's total momentum

$\mathbf{p}$  and quiver momentum  $\mathbf{p}_q = m_e c \mathbf{a}$  [10]:

$$\delta \mathbf{p} = \mathbf{p} - \mathbf{p}_q \quad (2.5)$$

$$\mathbf{F}_p = -m_e c^2 \nabla(a^2/2) \quad (2.6)$$

$\mathbf{F}_p$  in Eq. 2.6 describes the 3D ponderomotive force in the linear limit. Thus ponderomotive force can be thought of as a pressure term in hydrodynamic plasma equations proportional to the electromagnetic energy gradient of laser. A similar equation can be derived in the 3D nonlinear regime by subtracting quiver momentum and 3D space charge force effect from the fluid element's momentum equation (see [10]).

In the weakly relativistic 3D regime ( $a \ll 1$ , also called the linear regime), the wakefield is described by solving the cold fluid equations, which are the Poisson equation, the continuity equation and the fluid momentum equation [10]. In a uniform plasma, the solutions can be described as the following convolution integrals:

$$\delta n/n_0 = (c^2/\omega_p) \int_0^t dt' \sin[\omega_p(t-t')] \nabla^2 a^2(\mathbf{r}, t)/2 \quad (2.7)$$

$$E/E_0 = -c \int_0^t dt' \sin[\omega_p(t-t')] \nabla a^2(\mathbf{r}, t)/2 \quad (2.8)$$

Where  $\delta n/n_0 = (n_e - n_0)/n_0$  is the normalized density perturbation and  $\omega_p = \sqrt{4\pi n_0 e^2/m_e}$  is the plasma frequency. These convolution equations describe plasma waves at frequency of  $\omega_p$  and are valid for  $E < E_0 = m_e c \omega_p / e$  which is the cold nonrelativistic wave breaking field. These equations indicate that wakefield is most efficiently generated when the envelope scale length, is on the order of plasma wavelength ( $L = c\tau = \lambda_p = 2\pi c/\omega_p$  [7]). Also the radial extent of the wake is on the order of laser spot size  $r_0$ .

In the nonlinear regime, that in when  $E \geq E_0$ , wake generation can be

analyzed in 1D assuming that the laser beam is non-evolving. Solutions indicate that as the plasma wave amplitude becomes nonlinear, the plasma wave steepens, making a sawtooth profile and the plasma wavelength increases in proportion with maximum electric field in the wake, i.e. [10]

$$\lambda_{NP} = \lambda_p \begin{cases} 1 + 3(E_{max}/E_0)^2/16, & E_{max}/E_0 \ll 1 \\ (2/\pi)(E_{max}/E_0 + E_0/E_{max}) & E_{max}/E_0 \gg 1 \end{cases} \quad (2.9)$$

In the 3D nonlinear regime, numerical solutions are required. The nonlinear increase in plasma wavelength in 3D causes the front of the plasma wave to become curved since the wake is driven harder on axis by a Gaussian beam with the maximum intensity on axis. Hence the wake fronts curve and for a plasma wave of fixed amplitude, the farther back within the plasma wave train, the more curved the plasma wavefront ( $\lambda_{NP}$  greater on axis than off axis). At higher laser intensities, it is possible to reach a bubble (or blowout) regime, where all the electrons are expelled by the ponderomotive force of the laser and a region of  $\delta n/n_0 \sim 1$  travels behind the laser pulse with  $n_0$  being the initial homogeneous density and  $\delta n$  being the displaced electron density by the ponderomotive force. The relativistic Lorentz factor for the phase velocity of wakes in linear regime and for densities much less than critical density, can be described by the following equation [11]

$$\gamma_p = \omega_0/\omega_p \quad (2.10)$$

In the highly nonlinear regime ( $a_0 \gg 1$  [12]), the characteristic time for laser to transform to the bubble regime, is given by equation 2.11 and evolution of this regime happens on a time scale given by 2.12.

$$\Delta t_f \propto \frac{k}{ck_p^2} \quad (2.11)$$

$$\Delta t_s \propto \frac{a_0 k}{ck_p^2} \quad (2.12)$$

Where  $k_p = \omega_p/c$ . These conditions are satisfied as long as the power threshold to reach the bubble regime is satisfied:

$$P > P_{bubble}GW = \left( \frac{\tau[\text{fs}]}{\lambda[\mu\text{m}]} \right)^2 \times 30 \quad (2.13)$$

E.g. for a 28 fs pulse at 800 nm,  $P_{bubble} \simeq 40TW$

## 2.2 Laser Guiding

In order for laser pulse to drive the wakefield beyond one Rayleigh range, it has to be guided inside the plasma. Self guiding in the nonlinear wakefield regime has been shown to be able to extend the laser plasma interaction region over thirteen Rayleigh ranges at high powers [11] without the need for preformed plasma guiding channels. Indeed it is experimentally shown that the extent of self-guiding is limited by the nonlinear pump depletion [13].

The two laser guiding processes in plasma relevant to that experiment as well as ours are relativistic and ponderomotive self focusing. There are two other mechanisms by which a laser pulse may be guided inside plasma, namely laser guiding in a preformed plasma channel and plasma wave guiding, which are inapplicable to our case. Guiding mechanisms in plasma are based on the principles of refractive guiding [10], where a modification of the radial profile of the index of refraction leads to laser beam guiding. When the radial profile of the index of refraction has a maximum on axis, the phase velocity of the outer

edges becomes greater than the phase velocity on axis, leading to a curved wavefront which focuses the beam.

The general expression for the index of refraction of the plasma for a large amplitude electromagnetic wave is [14, 15]:

$$\eta_r(r) \simeq 1 - \frac{\omega_p^2}{2\omega^2} \frac{n_e(r)}{n_0\gamma(r)} \quad (2.14)$$

which is valid for  $\omega_p^2/\omega^2 \ll 1$ . The electron quiver motion is the leading order term in the equation describing the motion of the electron [10]. Thus  $\gamma$  can be written as

$$\gamma \simeq \gamma_{\perp} = (1 + a^2)^{1/2} \quad (2.15)$$

From equation 2.14 and 2.15, there are two ways to generate self focusing: a laser profile peaked on axis (relativistic self focusing), or a modified plasma density,  $n_e(r)$  (other self focusing mechanisms). For the rest of this section, the laser shall be assumed to be in the linear, weakly relativistic regime ( $a^2 \ll 1$ ). The underlying physics can be extended to other regimes as well. In the linear regime, assuming no external plasma channel forming, we can rewrite Eq. 2.14 for a circularly polarized pulse as [7]:

$$\eta_r \simeq 1 - \frac{\omega_p^2}{2\omega^2} \left( 1 - \frac{a^2}{2} + \frac{\delta n}{n_0} \right) \quad (2.16)$$

in this expression,  $a^2/2$  is responsible for relativistic self-focusing and  $\delta n/n_0$  for laser induced density modifications, such as the modification due to the ponderomotive force. During the experiments, we monitored laser guiding using an imaging system which recorded the laser mode at the end of the interaction (See section 3.2.4).

### 2.2.1 Relativistic Optical Guiding

In the standard theory of relativistic optical guiding only electron quiver motion is considered and the effect of plasma response is ignored<sup>1</sup>. In this case, Eq. 2.16 can be written as[10]

$$\eta_r \simeq 1 - \frac{\omega_{p0}^2}{2\omega^2}(1 - a^2/2) \quad (2.17)$$

Using this expression for index of refraction, an equation describing the laser spot size can be devised from the solution to the paraxial wave equation (given in [10]):

$$\frac{d^2 R}{dz^2} = \frac{1}{Z_R^2 R^3} \left( 1 - \frac{P}{P_c} \right) \quad [16] \quad (2.18)$$

where  $R = r_s(z)/r_0$  is the normalized spot size with  $r_0$  being the minimum spot size in vacuum and  $Z_R$  vacuum Rayleigh length. The first term on the right accounts for vacuum diffraction and the second term describes relativistic self focusing.  $P_c$  in 2.18 is called the relativistic power for self focusing and is given by

$$P_c[\text{GW}] = 2c(e/r_e)^2(\omega/\omega_p)^2 = 17.4(\omega/\omega_p)^2 \quad (2.19)$$

where  $r_e = e^2/m_e c^2$  is the classical electron radius. The solution to 2.18 for the beam radius is

$$r_s^2/r_0^2 = 1 + (1 - P/P_c)z^2/Z_r^2 \quad (2.20)$$

This equation predicts indefinite focusing of laser for  $P > P_c$ . This is the result of the linear approximation  $a \ll 1$  and will not occur when higher order nonlinear terms are considered.

Finally, inclusion of self consistent density response indicates that relativistic

---

<sup>1</sup>It can be shown that with self-consistent electron density response for long pulses, in the 1D weakly relativistic limit Eq. 2.17 can still be used to describe the index of refraction

self focusing is ineffective in preventing the diffraction of short laser pulses ( $L \leq \lambda_p/\gamma_\perp$ ) since the index of refraction changes on the plasma frequency time scale and if the laser is too short in duration, there is insufficient time for the laser to be effected by relativistic motion of electrons [17, 14].

### 2.2.2 Ponderomotive Self Channelling

In high power lasers, the radial ponderomotive force of a long pulse ( $L \gg \lambda_p$ ) can expel electrons from the axis, creating a density channel which enhances the effect of relativistic self-focusing. An expression for the density perturbation due to this force can be obtained using the steady-state radial force balance [18, 14, 10]:

$$\delta n/n_0 = k_p^{-2} \nabla_\perp^2 (1 + a^2)^{-1/2} \quad (2.21)$$

assuming  $|\delta n/n_0| \leq 1$ . The corresponding index of refraction is

$$\eta_r \simeq 1 - \frac{\omega_p^2}{2\omega^2} \left[ \frac{1 + k_p^{-2} \nabla_\perp^2 (1 + a^2)^{1/2}}{(1 + a^2)^{1/2}} \right] \quad (2.22)$$

Thus in the linear limit, a Gaussian laser profile with

$$a^2 = a_0^2 e^{-2r^2/r_0^2}$$

creates a density profile with

$$\delta n = -\delta n(0) (1 - 2r^2/r_0^2) e^{-2r^2/r_0^2}$$

$\delta n(0)$  in this equation is the density perturbation on axis, or the depth of ponderomotive channel and is given by  $\delta n(0) = a_0^2 \Delta n_c$  where  $\Delta n_c [\text{cm}^{-3}] = (\pi r_e r_0^2)^{-1} = 1.13 \times 10^{20}/r_0^2 [\mu\text{m}]$  is the critical channel depth which is an important parameter in preformed plasma density channel guiding [10]. Analysis

of the paraxial wave equation with a density perturbation given by 2.21 in the weakly relativistic regime ( $a^2 \ll 1$ ) gives the following for the evolution of normalized Gaussian laser spot size [19]:

$$\frac{d^2 R}{dz^2} = \frac{1}{Z_R^2 R^3} \left( 1 - \frac{P}{P_c} - \frac{\delta n(0)}{2\Delta n_c} R^{-2} \right) \quad (2.23)$$

where  $\delta n(0) = a_0^2 \Delta n_c$  is the depth of ponderomotive channel. In the weakly relativistic regime then,  $\delta n(0) \ll \Delta n_c$  and if  $P < P_c$  the ponderomotive self channelling will not guide the laser. Thus ponderomotive self channelling can enhance the effect of relativistic self-focusing but does not dramatically alter the power threshold for guiding. More detailed studies including both relativistic and ponderomotive self focusing such as [18] concluded that the constant factor on the right hand side of Eq. 2.19 should be 16.2. However a large number of papers in literature (including [20],[21],[13],[22]) use 17 as the constant factor and so in order to keep consistent with the values reported in literature, the critical power of self focusing will be taken as

$$P_c[\text{GW}] = 17 \left( \frac{\omega^2}{\omega_p^2} \right) = 17 \frac{n_{cr}}{n_e} \quad (2.24)$$

$n_{cr}$  being critical density.

Furthermore there is a question of matched spot size for maintaining a self focused channel. Simulations indicate that in the 3D-nonlinear regime ( $a_0 \geq 2$ ) the guided spot size is described by [22]

$$k_p r_s = 2\sqrt{a_0} \quad (2.25)$$

while in linear and 1D nonlinear regimes ( $a_0 \simeq 1$ ) it is described by  $k_p r_s = 2\pi$  [22, 3, 23]. Finally in the ultrarelativistic limit ( $a_0 \gg 1$ ), the matched spot size

satisfies  $k_p r_s = \sqrt{a_0}$  [12]. It has been shown that for  $P > P_c$  and  $r_0 > r_s$  the spot size will converge to and remain at  $r_s$ , but on the contrary,  $r_0 < r_s$  will only lead to large erosion and a very small portion of the light is guided. [13]

## 2.3 Electron Injection

A wakefield set up in plasma by a guided laser pulse provides an ideal accelerating medium for electrons that can be placed between wave crests. Placing electrons in the accelerating phase of the wake is called injection or trapping. There are several different mechanism of injection that have been explored over the years. Here the focus will be on the injection mechanisms important in our experiments and other mechanism will be very briefly introduced in section 2.3.3.

### 2.3.1 Wavebreaking Injection

As previously mentioned, in the cold nonrelativistic limit, a plasma can sustain electron waves with the maximum electric fields on the order of the nonrelativistic wavebreaking field [7]

$$E_0[\text{V/cm}] = cm_e \omega_p / e \simeq 0.96 n_e^{1/2} [\text{cm}^{-3}] \quad (2.26)$$

$\omega_p$  being the electron plasma frequency,  $n_e$  the ambient electron density, and  $m_e$  the electron rest mass. In the nonlinear regime, it is possible for the maximum amplitude of the electric field to exceed  $E_0$ . Using the 1D nonlinear, relativistic, cold fluid equations, the maximum amplitude of the periodic plasma wave is [10]

$$E_{wb} = \sqrt{2}(\gamma_p - 1)^{1/2} E_0 \propto n_e^{-1/4} \quad (2.27)$$

with  $\gamma_p$  being the phase velocity Lorentz factor (Eq. 2.10). As the wave amplitude reaches the breaking limit, the cold plasma density becomes singular ( $n_e \rightarrow \infty$ ) and the cold plasma equations break down. This does not necessarily mean that the wave structure will collapse, as it is possible for a small portion of the wave to break, reducing the wave amplitude while also maintaining the wave structure [3].

The wavebreaking limit for 3D nonlinear case has not been thoroughly investigated and there are no general expressions in that regime for the maximum wake amplitude. In this regime, as described earlier a curved plasma wake forms. If the intensity of the beam is high enough, all the electrons are expelled from inside the wake. This regime of interaction is called bubble or blowout regime [10]. In the frame of the laser, sheaths of electron forming the bubble move backwards and cross at the back of the bubble. If the electrons are accelerated on a time scale shorter than their crossing, they can be trapped [24]. Two conditions have to be satisfied for the trapping to occur [22]:

- The blowout radius should be large enough so that electrons can gain enough longitudinal momentum to move almost at the speed of the laser pulse as they drift by the time they get to the back of the bubble.
- Sheath crossing occurs in a narrow enough region to provide high accelerating and focusing fields.

In simulations, self injection was routinely observed for a normalized blowout radius of  $k_p R_b \simeq 2\sqrt{a_0} \simeq 4 - 5$  [22], which leads to  $a_0 \simeq 4 - 6$ . Other sources indicate a threshold for injection with  $a_0 \simeq 3 - 4$  [25, 26, 23] either through experimental data or simulation. The experimental threshold (e.g.  $a_0 = 3.2$  in [23]) was found by finding a laser energy threshold ( $\varepsilon_{\text{th}}$ ) over which the percentage of electron shots yielding monoenergetic spectra stayed almost the same as the input energy increased. This energy threshold was inferred to be the

energy threshold for consistent electron injection. That energy was then related to the threshold value of normalized vector potential for electron injection ( $a_{\text{th}}$ ) by

$$\varepsilon_{\text{th}} = 23.3 \times 10^9 \frac{n_c}{n_e} a_{\text{th}}^2 \tau [J] \quad (2.28)$$

Which was derived assuming the laser pulse spot size evolves towards  $\lambda_p$ , pulse length towards  $\tau = \lambda_p/2$  and all the initial laser energy is compressed into the wake driving field.

When the self injection conditions are satisfied, trapping continues [11, 27] until enough charge accumulates in the bubble to counteract the bubble's electric field. This is called beam loading. Finally, it is noteworthy that the injection of multiple bunches in the wakes has also been observed in experiments and simulations [11], where the electrons are injected in the bubble as discrete bunches at different times. In these cases, the second bunch can rise to higher energies due to higher wake amplitude which exists at the later time.

### 2.3.2 Ionization Injection

Ionization injection is a new technique whereby large differences in ionization potential of the atomic species in the plasma are used for injection of electrons into the wakefield before the wake amplitude reaches wave breaking limit. This technique was reported as early as 2007 in plasma wakefield accelerators [28], where electron beams were used to drive plasma wakes instead of laser beams in laser wakefield accelerators. In [28, 29], the difference between the first electron ionization potential level of He (24.6 eV) and Li (5.39 eV) were used to create a uniform plasma with density equal to local lithium density whereby helium atoms remained largely unionized. As the wake amplitude rose in a process analogous to laser self focusing, the space charge field of the driving beam became large enough to ionize the first He electron. These newly ionized helium

electrons having been created inside the bubble can be trapped at a field level which is much lower than the wave breaking field. The trapped electron bunch had a normalized transverse emittance better than  $4 \mu\text{m}$  with a peak current greater than 9.2 kA [29].

Similar effects in laser wakefield acceleration were originally observed in capillary discharge waveguide experiments [30] where it was discovered that electron injection is very sensitive to plasma channel parameters, especially the degree of ionization. Even though the plasma channel existed for over 70 ns and wake formation was deduced to happen over 50 ns, there was only a window of 5 ns which produced electron beams. This 5 ns range appeared when some electrons have already undergone recombination. It was suggested that electrons generated near the peak of the laser pulse from either hydrogen or alumina constituents could account for the observed narrow temporal range for injection in a fashion similar to [28].

It was only recently however, that this phenomenon was systematically studied [24, 31] with helium gas being the main target in both experiments. Authors of [31] used only 9:1 mixtures of He:N<sub>2</sub> while inert gases Ar, Kr, Xe, and Ne were used in addition to 1% nitrogen as impurities in helium [24].

PIC simulations provided the main insight into the mechanism of injection by showing that the electrons were ionized at the peak laser intensity. Note that the electric field of the laser is greater than the peak bubble electric field. For  $a > 1$ , the bubble electric field scales as

$$E_{\text{bubble}} \propto \lambda_0/\lambda_p \times E_L$$

where  $E_L$  is the peak laser field. Furthermore, simulations indicate that the trapped electrons are entirely from N<sup>+6</sup> and N<sup>+7</sup>, which in [31] could be ionized by laser field after the pulse has undergone a small amount of self-focusing.

In these same simulation it was shown that the two helium and five nitrogen electrons generated by the front of the pulse only formed the wakefield and were not trapped. It was also shown that  $a_0 > 1.6$  is enough to ionize and trap the 6th electron of nitrogen.

In the absence of high Z gases, sporadic weak electron signals were only observed in [31], whereas [24] asserts that there is little difference between the mean energy of electrons produced by ionization injection and those produced by self trapping of helium. The reason for this discrepancy is that the  $a_0$  parameters used in [24], being 4.1 and 8.4, were so high that immediate wave breaking injection of electrons resulted and given the relatively long acceleration length of nearly 3 mm, there is not much difference between the energy of electrons as they are all trapped at the back of the bubble. The low  $a_0$  in [31] allows for reliable electron trapping only in the form of ionization injection. It is also noteworthy that all electron energy spectra shown with  $N_2$  were either quasi-Maxwellian, or had very wide energy spread. Also both of the experiments reported their electron densities in the range of  $1 - 3 \times 10^{19} \text{cm}^{-3}$

Where the significance of ionization injection becomes apparent in [24] is in the amount of charge and divergence. An order of magnitude increase in charge was observed compared to pure helium at the same density with beam divergence decreased by half. Authors of [31] also found decreased divergence and explained it as an artifact of electrons being generated near the axis (as opposed to the bubble boundary in wavebreaking injection) where the laser has enough power to ionize nitrogen atoms. Additionally, the fact that these electrons are ionized by the laser means that they gain additional transverse momentum in the direction of laser polarization. This leads to a beam with asymmetrical divergence

Finally, both papers warn against high number of trapped electrons as con-

tinuous electron injection leads to a decrease in the potential of the wake, limiting the trapped charge as well as final energy of the accelerated electrons. Additionally a large density of high Z gases leads to ionization defocusing which prevents wake formation.

### 2.3.3 Other Methods of Injection

Other methods of injection also aim at reducing the electric field threshold for electron injection. Such techniques would lead to lower laser energy requirements for electron acceleration and have the potential to create more stable electron beams. These techniques can be separated into two broad categories of multiple pulse injection and plasma gradient injection.

#### Plasma Gradient injection

A steep rising density gradient in a plasma formed by a shock wave created by the nanosecond pedestal, can lead to injection if the shock wave density jump occurs over a length which is less than a plasma wavelength [32, 33]. The fast rise in density can additionally increase the total charge [33]. In references [34, 35], a density down ramp is shown to induce injection where the ambient electron density is too low to support injection by wave breaking. Simulations indicate that injection observed in reference [34] occurs in the density down ramp when  $\lambda_p$  becomes resonant with laser pulse length. Additionally, 2D PIC simulations [35] indicate that in a sharp down ramp density gradient, injection occurs because of sudden change in plasma wavelength which can trap electrons in this transition.

## Multiple Pulse Injection

Crossing laser beams have also been shown to be able to produce injection in the region where the beams overlap. One beam with higher  $a_0$  is used as the driver of the wake while the second one causes injection. The polarization can be an important effect, albeit both parallel polarization [36, 37, 38] and cross polarization [39] can cause injection. Recently, a low laser power method of injection based on counter propagating pulses with circular polarization has been proposed [40], but no results have been reported as yet.

The advantages of the cross propagating beam injection are reportedly increased stability and reproducibility, in addition to the ability to control the electron beam charge and energy by controlling the parameters of the two laser beams [36].

Finally, in addition to head on collision of laser pulses, 45 degree [41, 42, 43] collision has also been demonstrated to lead to electron injection.

## 2.4 Acceleration Limiting Parameters

There are two main limiting factor in laser wakefield acceleration. The first limit is when the laser pulse loses too much energy to wake formation and can no longer maintain the bubble. The distance at which this happens is called the laser depletion length. Even if the laser could maintain its intensity indefinitely, as the electrons gain energy in the bubble, they eventually reach high enough velocity to outrun the wake, which is moving at the group velocity of the laser (Eq. 2.10). Thus as they move into the decelerating region of the wake they start losing their energy. This length, at which the maximum electron energy is obtained, is called the dephasing length.

### 2.4.1 Pump Depletion Length

Laser energy is continuously converted to wake energy. Photons that lose their energy to the wake are redshifted [44] and start falling behind due to the group velocity dispersion in plasma. Also the front of the pulse is continuously diffracted since as mentioned above, the plasma radial profile can only form a guiding channel on a time scale in the order of the plasma frequency. An analytical theory based on 1D laser wave equation coupled to nonlinear quasistatic fluid equation [44] showed that both laser wave energy ( $\varepsilon$ ) and average wavenumber ( $\langle k \rangle$ ) follow the same scale length:

$$\frac{\partial \varepsilon}{\partial ct} = -\varepsilon/L_{pd}$$

$$\frac{\partial \langle k \rangle}{\partial ct} = -\langle k \rangle /L_{pd}$$

where

$$L_{pd} = \frac{\omega^2}{\omega_p^3} \frac{E_0^2}{E_{max}^2} \varepsilon \quad (2.29)$$

In this equation,  $E_0$  is the cold nonrelativistic wavebreaking field (Eq. 2.26) and  $E_{max}$  is the maximum electric field amplitude behind the laser.  $\varepsilon = \int d(k_p \xi) |(1 + ik_0^{-1} \partial/\partial \xi) \hat{a}|^2$  is the normalized laser energy with  $\xi = ct - z$  and  $\hat{a}$  representing the complex wave envelope. For flat top pulse with optimized length for maximizing wake amplitude,

$$L_{pd} \simeq \begin{cases} \frac{\omega^2}{\omega_p^3} (4\pi/a_0^2) & a_0^2 \ll 1 \\ \frac{\omega^2}{\omega_p^3} \sqrt{8a_0} & a_0^2 \gg 1 \end{cases} \quad (2.30)$$

Another way to estimate pulse depletion is to consider the erosion of the front of the pulse. The laser etch rate in the laser pulse reference frame verified by 3D nonlinear simulations is  $v_{etch} \simeq c\omega_p^2/\omega_0^2$ . Therefore the pump depletion

length, where the energy of the pulse is etched away, can be written as [22]:

$$L_{pd} \simeq \frac{c}{v_{etch}} c\tau = \frac{\omega_0^2}{\omega_p^2} c\tau = \frac{n_{cr}}{n_e} c\tau \quad (2.31)$$

Since in our experiments we don't have a matched pulse, the term  $a_0$  could not be experimentally determined which is necessary in Eq. 2.30. Thus Eq. 2.31 was used in the analysis section as the equation for depletion length.

Also, given the laser etch rate, the phase velocity of the wake in the 3D nonlinear regime can be corrected to reflect the laser etching.:

$$v_{pN} \simeq v_l - v_{etch} \simeq c[1 - 3\omega_p^2/(2\omega_0^2)] \quad (2.32)$$

where  $v_l \simeq c[1 - \omega_p^2/(2\omega_0^2)]$  is the linear phase velocity.

### 2.4.2 Dephasing Length

In the linear regime, an expression for dephasing length is obtained by equating the maximum electron energy gain with  $eE_{max}L_d$  [7] with  $E_{max}$  representing the maximum electric field sustained in plasma [45, 7, 6] :

$$L_d \simeq \gamma_p^2 \lambda_p \simeq \lambda_p^3 / \lambda^2 \quad (2.33)$$

Where  $\gamma_p$  in the linear regime is given by Eq. 2.10

In the 3D nonlinear bubble regime, where all the electrons are removed from the accelerating bubble, the dephasing length can be written as [22]

$$L_d = \frac{c}{c - v_{pN}} R \simeq \frac{2\omega^2}{3\omega_p^2} R \quad (2.34)$$

where R is the blow out radius and  $v_{pN}$  is the phase velocity of the wake determined by 2.32. Since it was not possible to experimentally determine the size

of the bubble, Eq. 2.33 was used in analysis to estimate the dephasing length at different densities.

Finally, it is mentioned here for the sake of completeness that the acceleration limiting length in ultrarelativistic regime is given by [12]:

$$L \simeq 0.05 a_0 \frac{\omega^2}{\omega_p^2} c\tau \quad (2.35)$$

Where  $a_0$  is chosen to match plasma bubble condition given by  $k_p R \sim \sqrt{a_0}$ ;  $R$  being the bubble radius, equal to the focal spot radius.

## 2.5 Energy Gain

Maximum energy gain in the wakefield can be calculated in different ways. The simplest way is to calculate the accelerating field and multiply that by dephasing length. In the cold nonrelativistic regime, where the maximum electric field in a plasma wave is given by  $E_0 = cm_e\omega_p/e$  (Eq. 2.26) the energy gain is [46]

$$W[\text{GeV}] = E_0 L_d \simeq (m_e c \omega_p / e) (\lambda_p^3 / \lambda^2) \quad (2.36)$$

Using more sophisticated models for predicting the maximum electric field strength in the 1D nonlinear regime, the maximum energy gain can be written as [6, 47]:

$$W[\text{GeV}] = 0.4 I [\text{Wcm}^{-2}] / n_e [\text{cm}^{-3}] \quad (2.37)$$

These energy estimates are adequate in dealing with low intensity lasers ( $a \sim 1$ ). Other estimates of maximum energy, which are obtained using PIC simulations, are more apt for our experiments at 100 TW power regime. An estimate for the approximate energy gain is given based on the average peak of

accelerating electric field and the bubble radius [22]:

$$W[GeV] \simeq 1.7 \left( \frac{P[TW]}{100} \right)^{1/3} \left( \frac{10^{18}}{n_p[\text{cm}^{-3}]} \right)^{2/3} \left( \frac{0.8}{\lambda_0[\mu m]} \right)^{4/3} \quad (2.38)$$

An equation based on Eq. 2.38 can be written which gives the acceleration length ( $L_{acc}$ ) based on energy [21]:

$$W[MeV] \simeq 115 P[TW]^{1/4} L_{acc}[mm]^{1/2} \quad (2.39)$$

In comparison, the energy gain of a monoenergetic electron bunch in the ultrarelativistic regime ( $a_0 \gg 1$ ) is given by [12]

$$W \simeq 0.65 m_e c^2 \sqrt{\frac{P}{P_{rel}} \frac{c\tau}{\lambda}} \quad (2.40)$$

Where  $P_{rel} = m_e^2 c^5 / e^2 \simeq 8.5 TW$  is called the natural relativistic power unit.

In the analysis sections, Eq. 2.38 is used to plot maximum energy curves as they best describe the regime of interaction in our experiments.

## 2.6 Interferometry

Interferometry was mainly used to determine the density of the 2.4 mm gas target. It was also used in the 10 TW experiments to determine the density of the electrons. The principle method employed was to use the Mach-Zhender interferometer, consisting of two beam splitters and two mirrors (see Fig. 2.1). The beam splitters and mirrors caused the beam paths to form a parallelogram, resulting in equal beam path for the two beams created by the first beam splitter. The target, being either gas or plasma in our case, is placed in one of the arms of the interferometer. The resulting difference in the index of refraction caused by the presence of the target material in comparison with vacuum results in a

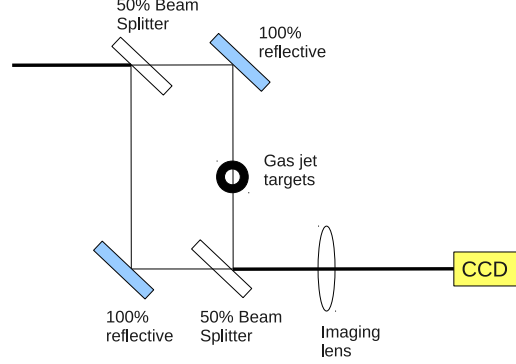


Figure 2.1: A schematic view of the Mach-Zehnder interferometer

phase change in the beam equal to

$$\delta\phi = \int_{-y_0}^{y_0} k (\eta_r(y) - 1) dy \quad (2.41)$$

where  $k = \frac{2\pi}{\lambda}$  and  $\eta_r$  is the index of refraction. The coordinate system used is the same as that used in [48], shown in Fig. 2.2, which shows the probe beam's path in 'y' direction through the target at the distance of 'x' from the center of the circularly symmetric object. For such circularly symmetric target like a horizontal slice of a gas jet or a cross section of a plasma created by laser ionization, we can rewrite equation 2.41 in polar coordinates as:

$$\delta\phi = 2 \int_0^{y_0} k (\eta_r(y) - 1) dy \quad (2.42)$$

$$= \frac{4\pi}{\lambda} \int_x^R \frac{(\eta_r(r) - 1) r dr}{(r^2 - x^2)^{1/2}} \quad (2.43)$$

The index of refraction can be extracted from the phase by using the Abel's

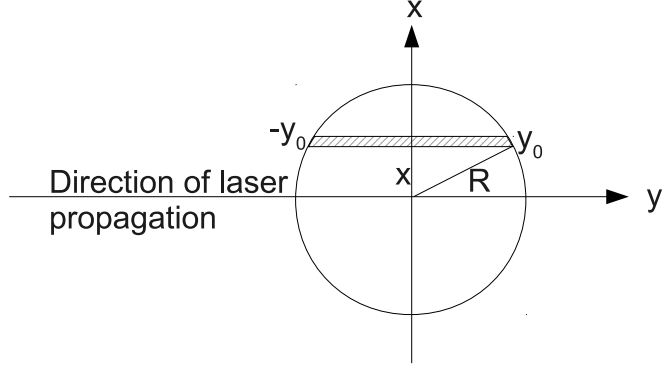


Figure 2.2: The laser probe traverses a circularly symmetric target such as a gas jet

transformation

$$\frac{4\pi}{\lambda} (\eta_r(r) - 1) = -\frac{1}{\pi} \int_r^R \frac{\delta\phi'(x) dx}{(x^2 - r^2)^{1/2}} \quad (2.44)$$

Where  $\delta\phi'(x)$  indicates differentiation of phase change with respect to 'x'. This integral formula can be replaced with a matrix sum using the the analysis described in [48]. In Einstein's summation format, the sum can be written as

$$\frac{4\pi}{\lambda} [\eta_r(r_j) - 1] = R^{-1} a_{jk} \delta\phi(x_k) \quad (2.45)$$

where  $r_j = \frac{jR}{n}$ ,  $x_k = \frac{kx_0}{n}$  ( $x_0 = R$  due to circular symmetry) and j and k iterate over values of 1,2,...,n-1. The matrix coefficients  $a_{jk}$  can be constructed using equations provided in [48].

The equations above provide a method for transforming phase shift ( $\delta\phi$ ) to index of refraction. In order to transform the interferograms into phase shifts, the quantity called fractional fringe shift can be used to make calculations simpler. This quantity is calculated by measuring the shift in the location of

fringe ( $\delta d(x_k)$ ) divided by the distance between fringes,  $d$ , at the same location as the phase shift is meant to be measured, i.e. at  $x_k$ . It can be shown that Eq. 2.45 can be rewritten with respect to fractional fringe shift as

$$\eta_r(r_j) - 1 = \frac{\lambda}{2R} a_{jk} \frac{\delta d(x_k)}{d} \quad (2.46)$$

Finally, the index of refraction has to be converted to density. If the target is a plasma, the electron density can be calculated using the dispersion relations of an electromagnetic wave with a small amplitude in plasma [49]

$$\eta_r^2 = 1 - \frac{\omega_p^2}{\omega^2} = 1 - \frac{n_e}{n_{cr}} \quad (2.47)$$

Where  $n_e$  is the electron density,  $n_{cr}$  is the critical density,  $\omega_p$  the plasma frequency, and  $c$  is the speed of light in vacuum.

To find the gas densities, first the nitrogen [50] and helium [51] dispersion equations were used to find the refractive index at the wavelength of 800 nm, which was the probe wavelength. Then, the simple relation of  $\rho_2 = \rho_1 \times \frac{\eta_{r2}-1}{\eta_{r1}-1}$  was used to find molecular density  $\rho_2$ .  $\eta_{r1}$  is the index of refraction calculated from dispersion curve and

$$\rho_1 = N_A \frac{ZP}{RT} \quad (2.48)$$

Where  $P$ ,  $R$ ,  $T$ , and  $N_A$  are pressure, universal gas constant, temperature, and the Avogadro's number. The effect of particular gases is taken into account using the unitless parameter  $Z$ , called the compressibility factor. This parameter (equal to 1 for ideal gas) is taken from [52] for nitrogen and [53] for helium,

represented by simple virial forms by

$$\begin{aligned} He : Z = 1 + (0.74062 \times 10^{-8}T^2 - 0.061793 \times 10^{-4}T \\ + 16.742 \times 10^{-4})P[51] \end{aligned} \quad (2.49)$$

$$N_2 : Z = 1 - P(317.60 - T) \times 10^{-5}[50] \quad (2.50)$$

Where P is pressure in atmospheres and T is temperature in Kelvin.

The linear relation between  $\rho$  and  $(\eta_r - 1)$  could be used because both gases obey the Lorentz-Lorenz law [54]:

$$\frac{\eta_r^2 - 1}{\eta_r^2 + 2}\rho^{-1} = \frac{N\alpha}{3\epsilon_0} \quad (2.51)$$

$$\frac{\eta_r - 1}{\rho} = \frac{(\eta_r^2 + 2)N\alpha}{(\eta_r + 1)3\epsilon_0} \quad (2.52)$$

In this equation,  $\alpha$  is the polarizability and  $\epsilon_0$  is the permittivity of the free space. N is the Avogadro's number if  $\rho$  is expressed in moles per unit volume. The right hand side of equation 2.52 is approximately constant since  $\eta_r \approx 1$ . Experimentally, the right hand side of 2.51 is shown to change on the order of only 0.3% over a range of 650 psi for nitrogen and on the order of 0.3% over 1000 psi for helium [55, 56].

## 2.7 Electron Energy Spectrometer

The relativistic equation of motion for a charged particle in a magnetic field is

$$\frac{d\vec{\mathbf{p}}}{dt} = q(\vec{\mathbf{v}} \times \vec{\mathbf{B}}) \quad (2.53)$$

where  $\vec{\mathbf{p}} = \gamma m \vec{\mathbf{v}}$  is the relativistic momentum of the particle and  $\gamma = (1 - (v/c)^2)^{-1/2}$  is the relativistic Lorentz factor. Using the relativistic en-

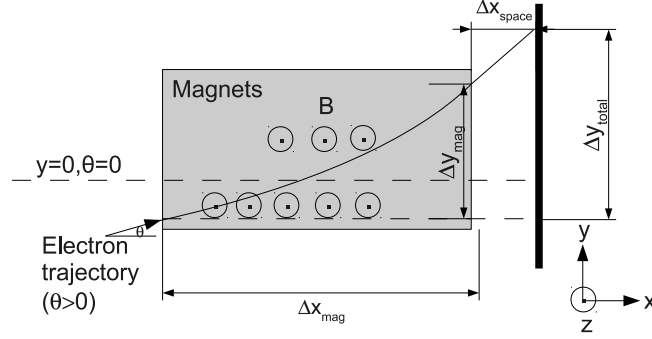


Figure 2.3: Electron deflection follows an arc in the magnetic field and a line after them.

From the energy equation  $E = \gamma mc^2$  we derive the relationship between energy and initial velocity:

$$\frac{v}{c} = \sqrt{1 - \left(\frac{mc^2}{E}\right)^2} \quad (2.54)$$

For electrons, the rest mass ( $mc^2$ ) is 0.511 MeV. Since the magnetic field does no work, the magnitude of velocity and hence  $\gamma$  are constants throughout the magnetic deflection, Eq. 2.53 can be simplified to

$$\gamma m \frac{d\vec{v}}{dt} = q(\vec{v} \times \vec{B}) \quad (2.55)$$

To determine the energy of electrons in these experiments, we used constant magnetic fields to deflect electrons according to their energies. A simplified view of the spectrometer with main elements are shown in Fig. 2.3. The line of  $\theta = 0$  is the path of laser. With the coordinate system displayed in this figure, the electron deflection is

$$\Delta x_{mag}(t) = \frac{v}{\omega_0} [\sin(\omega_0 t + \theta) - \sin(\theta)] \quad (2.56)$$

$$\Delta y_{mag}(t) = y_0 + \frac{v}{\omega_0} [\cos(\theta) - \cos(\omega_0 t + \theta)] \quad (2.57)$$

$$\Delta y_{space} = \frac{v_{yf}}{v_{xf}} \times \Delta x_{space} \quad (2.58)$$

Where  $\Delta y_{mag}$  and  $\Delta x_{mag}$  are the  $x$  and  $y$  deflections of electrons due to the magnetic field at time ' $t$ ' and  $\omega_0 = \frac{eB}{\gamma m}$  is the magnitude of the relativistic gyration frequency for electrons. The total deflection  $\Delta y_{total} = \Delta y_{mag} + \Delta y_{space}$  of the electrons is then calculated by considering the free space propagation of electrons after the magnets where  $\Delta x_{space}$  is the distance between the magnets and observation screen along the laser propagation direction.  $v_{xf}$  and  $v_{yf}$  in Eq. 2.58 are the components of the velocity of the electrons as they leave the magnets and can be calculated thus:

$$v_{fx} = v \cos(\omega_0 t + \theta) \quad (2.59)$$

$$v_{fy} = v \sin(\omega_0 t + \theta) \quad (2.60)$$

## Chapter 3

# Experimental Setup

The primary experiments were performed at the Advanced Laser Light Source (ALLS) facility at the Institut National de la Recherche Scientifique (INRS) in Montreal. We used two different laser systems for our experiments: the 10Hz/10 TW laser and later the 10Hz/100 TW laser. The laser systems as well as the targets and the diagnostic setups used during the experiments are described in this chapter.

### 3.1 10 TW System

#### 3.1.1 Laser

The initial phase of the experiment was carried out with the 10 TW laser system at ALLS. The system was designed to deliver 300 mJ per pulse compressed in 30 fs. For the experiments reported here, it typically provided 210 mJ pulses compressed in 33 fs, yielding peak power of 6.3 TW on target. This power was similar to previous rounds of experiments [57] with this system. The experimental setup is shown in Fig. 3.1.

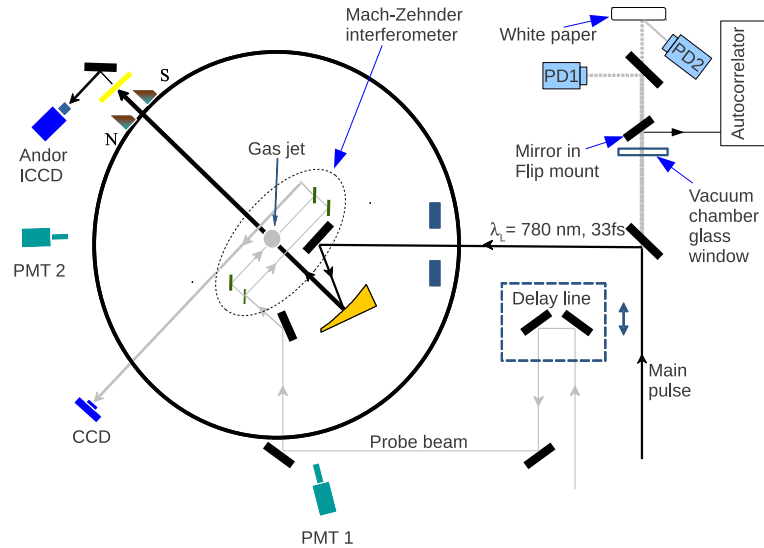


Figure 3.1: The schematic diagram of the typical experimental setup and vacuum chamber used in the 10TW experiments

Part of the beam (5%) was split from the main beam using partial transmission through one of the mirrors in the compressor and used as an optical probe diagnostic; to carry out shadowgraphy and interferometry of the interaction. This probe laser beam, shown as a grey beamline in Fig. 3.1, went through an adjustable delay line, which could be adjusted to bring the probe to the interaction region in a time frame spanning the entire interaction time from before the main pulse arrived at the gas jet to a few picoseconds after it had left it.

The target was positioned in one of the arms of a Mach-Zehnder interferometer setup. This interferometer consisted of two beam splitters and two mirrors as indicated in Fig. 3.1. The beam splitter creates two identical beams from the original probe beam line which travel identical paths and are combined at the end through the second beam splitter. The interference of the two beams generates a fringe pattern at the end. In the presence of a disturbance (i.e.

plasma), the fringes would bend and the density of the plasma could be calculated according to the process described in section 2.6. When the probe beam was completely blocked, the setup was used to monitor the self-emission of the plasma.

To focus the 6.3 TW laser pulse at our target, we used two 30 degree off axis parabolas. One had a focal length of 304.2 mm and focused the beam to a spot size of  $26 \times 27 \mu\text{m}$  FWHM, resulting in a peak intensity of  $6 \times 10^{17} \text{ Wcm}^{-2}$  and  $a_0 \sim 0.5$  assuming 70% of Energy in the main spot. The other had a focal length of 152.4 mm, producing a FWHM spot size of  $11 \times 13 \mu\text{m}$  and thus a maximum intensity of  $3 \times 10^{18} \text{ Wcm}^{-2}$  and  $a_0 \sim 1.2$  also assuming 70% of Energy in the main spot.

### Pulse Length and Prepulse Monitors

Important characteristics of the input laser pulse were diagnosed outside of the vacuum chamber as shown in Fig. 3.1, using a small portion of the laser pulse leaking through one of the turning mirrors. After going through the turning mirror and the glass window of the vacuum port, this beam was used for two purposes:

1. It was used to measure the amount of prepulse in the laser system. The femtosecond prepulse [58] (fspp), arriving about 8 ns prior to the main pulse, was measured by a fast photodiode with the light being reflected to it off of a wedge plate. The nanosecond prepulse [58, 32] was measured by another fast photodiode, looking at a piece of paper illuminated by the light that passed through the wedge (both shown in Fig. 3.1). Both of these photodiodes were calibrated against the main pulse and were the main method to measure the prepulses in the system. To adjust the level of prepulse we changed the Pockels cell timing of one of the amplifiers,

increasing or decreasing prepulse levels as needed.

2. Using a flip mirror in the path of the prepulse measurement setup, the leakage light from the turning mirror was redirected to a second order autocorrelator provided by the INRS to measure the duration of the laser pulse. By adjusting the separation between grating mirrors in the compressor, the duration of our laser pulse could be changed. Since the pulse measured by the autocorrelator went through the mirror and a vacuum glass window, it had a different chirp and pulse duration from the main pulse in vacuum. Thus the duration of the shortest pulse and the grating mirror position which produced it were different from the values for the pulse in vacuum. To find the difference we calibrated the measurements of the second order autocorrelator against the measurement of a frequency doubled signal which is an intensity dependent measurement [59]. According to the plots shown in Fig 3.2, the difference between shortest pulse in vacuum and the shortest pulse measured by the autocorrelator was 200 steps of the grating mirror. This value was used to set the operating point in vacuum relative to the minimum pulse length measured on the diagnostic autocorrelator.

### 3.1.2 Targets

The experiments used supersonic gas jets of helium and nitrogen. For 10 TW experiments, we used supersonic gas jet targets based on the design described in [60] with  $D_{crit}$  of 0.8 mm and  $D_{exit}$  of 2.4 mm (see figure 3.4 in section 3.2.2). Helium and nitrogen were used as target gases with backing pressures up to 1100 psi. The gas density of the gas jet was measured at the University of Alberta using a Mach-Zehnder interferometer. The targets were placed in one of the identical arms of the Mach-Zehnder interferometer setup, schematically shown

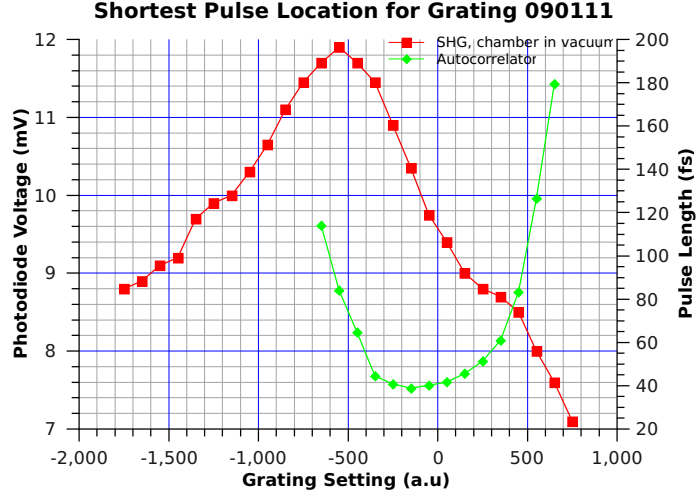
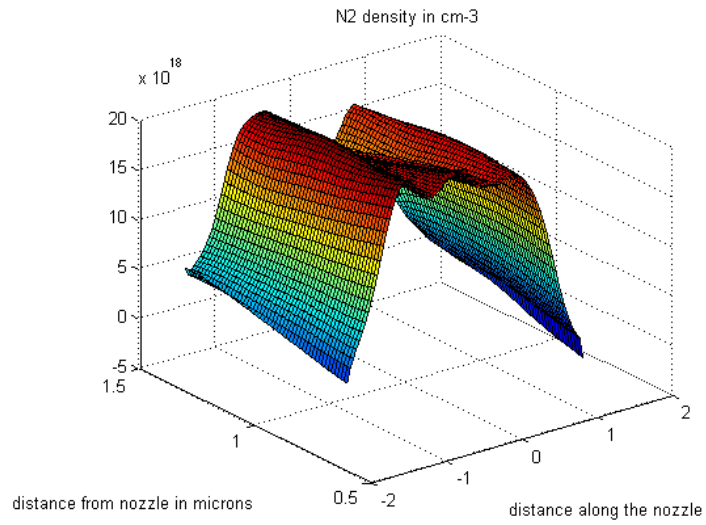


Figure 3.2: The curves from the frequency doubling experiment and autocorrelator measurement

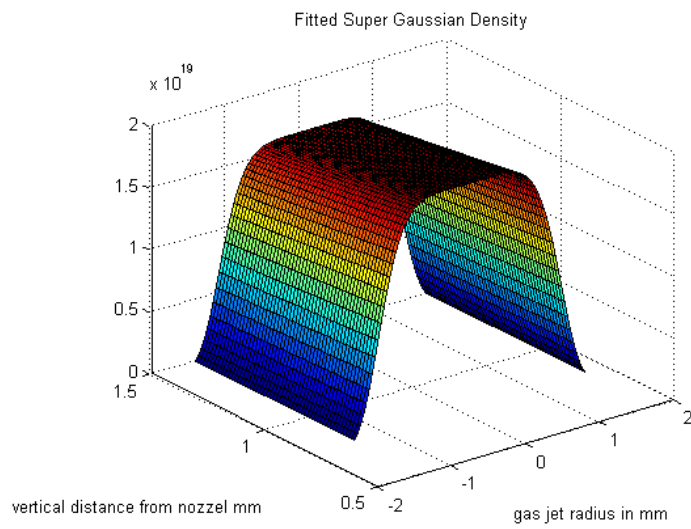
in Fig. 2.1. This was the same setup that was used in the main experiment as shown in Fig. 3.1. Without any gas, the interferometer produced parallel fringes. The gases caused fringe shifts according to the type and density of the gas. The density of the gas from these interferograms was deduced using the process described in section 2.6. The resulting surface plot for Nitrogen at 1000 psi is shown in the Fig. 3.3 on the top. On the bottom of the same figure, the super Gaussian curve fitted to the data is shown. The equation for this curve is

$$\rho[\text{cm}^{-3}] = 2.11 \times 10^{19} \exp\left(-\left(\frac{r[\text{mm}]}{1.28}\right)^6 - \frac{z[\text{mm}]}{6}\right) \quad (3.1)$$

where  $\rho$ ,  $r$ ,  $z$  are the molecular density of the gas, the radial distance from the centre of the gas jet and the elevation above the nozzle respectively. This equation will be used as the density of the gas in calculations in subsequent chapters.



(a)



(b)

Figure 3.3: (a) shows the density contour of the 2.4 mm nozzle as determined by interferometry and (b) the super Gaussian fit to the data

### 3.1.3 Electron Diagnostics

We used permanent magnets to determine the energy of the electrons. In the presence of the magnetic field, the electrons were deflected in accordance with their energy; the lower the electron energy the higher their deflection (see section 2.7). After going through the magnets, the electrons illuminated a Kodak Lanex fluorescent screen [61], imaged onto a cooled Andor ICCD using an F/1 Nikon lens. The Lanex screen was covered by a 16-25  $\mu\text{m}$  Al foil to shield the Lanex film from the laser light without significantly altering the electron trajectories.

A lead slit (not shown in Fig. 3.1) centred on the laser beam path after the target was used to define the starting trajectory of the electron bunches and enhance the resolution of energy measurements. Though the electron beams have significant pointing variability as also observed by others [21], a portion of the electrons did go through the slits and those were the ones whose energy we could observe and calculate.

Filtered scintillator PMT detectors were used to measure the emission of X-rays. These X-rays are primarily produced by high energy electrons impacting solid structures including the target nozzle. Their signals were used as a diagnostic and optimization tool.

## 3.2 200 TW System

### 3.2.1 Laser

A target chamber located on the 200 TW beamline at ALLS was used for the scaling studies at higher intensities. The 200 TW [62] laser system was completed in fall 2009. The system, including all of the focusing optics and some of the diagnostics were maintained and characterized by the INRS staff. At peak performance, the laser could supply 4 J of energy compressed in 25 fs. However,

Day	focal spot	Average Laser Power	I [ $\text{Wcm}^{-2}$ ]	$a_0$
100302	$40\mu\text{m} \times 32\mu\text{m}$	65 TW	$4.5 \times 10^{18}$	1.5
100311	$30\mu\text{m} \times 35\mu\text{m}$	82 TW	$6.9 \times 10^{18}$	1.8
100312	$41\mu\text{m} \times 41\mu\text{m}$	68 TW	$3.6 \times 10^{18}$	1.3
100315	$22\mu\text{m} \times 37\mu\text{m}$	60 TW	$6.5 \times 10^{18}$	1.8
100316	$28\mu\text{m} \times 45\mu\text{m}$	76 TW	$5.3 \times 10^{18}$	1.6

Table 3.1: The measured FWHM of the focal spot (Horizontal  $\times$  Vertical) on various experimental days. This variation lead to having different average values of intensities and  $a_0$  on different days

the highest laser energy achieved with this system during our experiments was on the order of 2.8 J and for most experiments was about 2 J. The pulse width was measured to be around 28 fs by INRS staff. Hence our laser had a maximum power of 100 TW, but most of the time, it was around 65-80 TW.

Prior to entering the chamber, the laser profile had a super Gaussian spatial profile of 75 mm FWHM. An off-axis-parabola with 150 cm focal length was then used to focus the beam in the centre of the chamber.

The focal spot, and hence  $a_0$ , varied day to day. The measured focal spots for several days of the experiment are given in table 3.1. Since laser power was significantly adjusted during 100311, the value for power on that day represents the power obtained when the laser was operating at full power. For other days, average power is used since the laser power tends to fluctuate from shot to shot (e.g. on 100316, the power fluctuated between 71 and 80 TW)

The focal spot was observed under vacuum during the experiments by an imaging system described later in this chapter (section 3.2.4). the size of each spot is calculated according to the following formula:  $\text{FWHM}[\mu\text{m}] = \text{FWHM}_{\text{pixel}}/M \times p[\mu\text{m}]$  where M is the magnification of the setup; being 5(6.2) with(without) the reflective mirror after the wedge (see figure in section 3.2.4) and p is the pixel size of the cameras which was  $4.65\mu\text{m} \times 4.65\mu\text{m}$  in the  $1280 \times 960$  pixel output mode and  $9.3\mu\text{m} \times 9.3\mu\text{m}$  in  $640 \times 480$  mode, where the

camera bins every four pixels together in each image.

### 3.2.2 Gas Jet Targets

For most of the experiment, the targets used were supersonic gas jet targets based on the design described in [60]. Simple conical Gas jet nozzles were made at the Electrical and Computer Engineering Department's machine shop with  $D_{crit}$  of 0.8 mm and  $D_{exit}$  of 2.4 mm, 5 mm, and 10 mm (see figure 3.4). The gas nozzle with 2.4 mm exit diameter is the same one as used in 10 TW experiments with molecular densities equal to those described in section 3.1.2.

The densities for the nozzles with 5 and 10 mm exit diameters were estimated based on the one dimensional flow characteristic equations [63, 64]:

$$\frac{S}{S_*} = \frac{1}{M} \left[ \frac{2 + (\gamma - 1)M^2}{\gamma + 1} \right]^{\frac{\gamma+1}{2(\gamma-1)}} \quad (3.2)$$

$$\frac{\rho}{\rho_0} = \left[ 1 + \frac{\gamma - 1}{2} M^2 \right]^{-\frac{1}{\gamma-1}} \quad (3.3)$$

$$\sin \alpha = \frac{1}{M} \quad (3.4)$$

Where  $M$ , the mach number is the ratio of the speed of gas to the speed of sound in that gas,  $\gamma$  is the ratio of specific heat (5/3 for helium and 7/5 for nitrogen),  $S$  is the area at the exit, and  $S_*$  is the critical area (at the throat of the nozzle).  $\rho$  is the density where the area equals  $S$  and  $\rho_0$  is the density in the reservoir, calculated using the ideal gas law and the known backing pressure. Finally  $\alpha$  indicates the angle of divergence of gas jet outside the nozzle, from which gas expansion at 1 mm away from the nozzle can be deduced. The locations of parameters used for this calculation are schematically shown in Fig. 3.4

The calculation chain is thus: The Mach number at  $D_{exit}$  is first calculated using the ratio of the areas according to equation 3.2. The area 1 mm away from the gas jet opening was then calculated using the angle  $\alpha$  from Eq. 3.4. Given

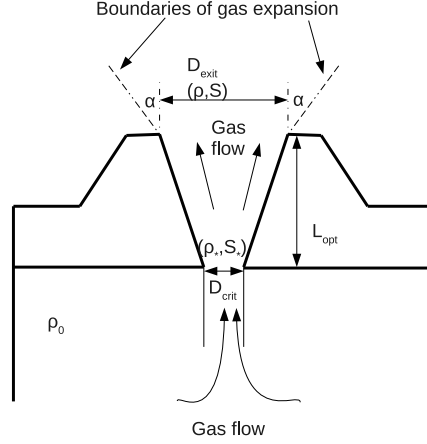


Figure 3.4: The schematic view of the conical gas jet nozzles used in the experiments. The 2.4 mm nozzle could produce electron density as high as  $10^{20} \text{cm}^{-3}$

this new area at 1 mm away from the nozzle, the Mach number is recalculated at that distance and finally, the density is calculated using equation 3.3.

The calculated molecular density for nitrogen and helium for pressures of 1000 psi are given in table 3.2. The experimental super Gaussian fit equation for 2.4 mm gas jet (Eq. 3.1) gives  $1.8 \times 10^{19} \text{cm}^{-3}$  as nitrogen's molecular density at 1000 psi, 1 mm away from the nozzle. Comparing the results of the 1D theory with the experimental result for 2.4 mm gas jet, it appears that there is a factor of 2.5 decline from theory to experiment. The losses are mainly due to 3D effects [60]. Additionally, 1D equations are developed for isentropic gas in a De Laval nozzle, having a slowly varying converging-diverging diameter. Our gas jet nozzles, however, do not have a slowly converging and diverging shape. Taking this difference into consideration, a geometric factor of 2.5 is introduced where all the electron densities resulting from ideal 1D equations are divided by this number to give the final electron densities listed in table 3.2. All the electron density numbers in table 3.2 except for nitrogen density at 1000 psi for

Dcrit (mm)	Dexit (mm)	L <sub>opt</sub> (mm)	Estimated atomic gas density 1 mm above the nozzle (cm <sup>-3</sup> ) at backing pressure of 1000 psi for He (N <sub>2</sub> molecular density numbers inside parenthesis)	Expected electron density on full ionization (N <sub>2</sub> in parenthesis)
0.8	2.4	–	$5.3 \times 10^{19}$ ( $4.4 \times 10^{19}$ )	$4.2 \times 10^{19}$ ( $1.8 \times 10^{20}$ )
0.8	5	10.5	$1.3 \times 10^{19}$ ( $1.1 \times 10^{19}$ )	$1.0 \times 10^{19}$ ( $4.4 \times 10^{19}$ )
0.8	10	15.3	$3.4 \times 10^{18}$ ( $2.8 \times 10^{18}$ )	$2.7 \times 10^{18}$ ( $1.1 \times 10^{19}$ )

Table 3.2: Gas jet nozzles dimensions and calculated densities for the nozzles used in the experiments. In electron density calculation, the ionization states of nitrogen and helium are assumed to be +5 and +2 respectively

2.4 mm nozzle are obtained in this manner. Ionization states for helium and nitrogen are assumed to be +2 and +5 respectively for electron density column of table 3.2. Further work is required to establish the accuracy of these density estimates.

The dimensions used for L<sub>opt</sub> in Fig. 3.4 are given in table 3.2 which were obtained by extending the designs of [60] so that the cross sectional area of the gas jets increases at the same rate, but D<sub>crit</sub> is 0.8 mm instead of 1 mm. No value for 2.4 mm nozzle is given since it was designed earlier for the 10 TW system.

A commercial Parker Valve solenoid (Model 009-181-900) was used to allow an inflow of gas through the nozzle for about 12 ms. The valve was controlled with a home made electronic system with a monitor pulse which indicated the valve’s operation.

Helium and nitrogen gases were used as the choice gases with backing pressures as high as 1000 psi, which in the case of nitrogen at full ionization could produce electron densities higher than 10<sup>20</sup>cm<sup>-3</sup>. We also used a mixtures of these gases, introducing various percentages of nitrogen in helium to investigate

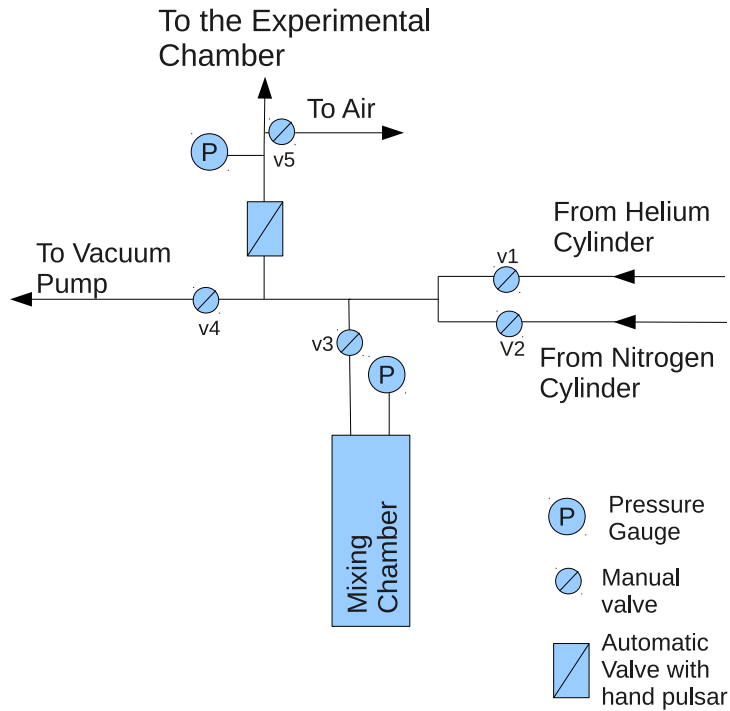


Figure 3.5: The gas network used for mixed gas experiments

the efficacy of the ionization injection (see section 2.3.2). To hold the mixed gases, we used a cylindrical chamber with direct lines from the two main gas cylinders (Fig. 3.5). The filling of the cylinder could be controlled with valves so that the chamber could be accurately filled with desired ratio of partial pressures of nitrogen and helium. The cylinder could be quickly emptied by a roughing vacuum pump. The automatic valve controlled with a hand trigger was a fail-safe measure to protect the turbo pump inside the experimental chamber from failing in case the solenoid valve failed to close after the shot. The gas inside the tube between the hand pulsar and the Parker solenoid valve could only be emptied into the air. Also during the experiments, the two pressure gauges shown in Fig. 3.5 would sometimes show significantly different pressures, which

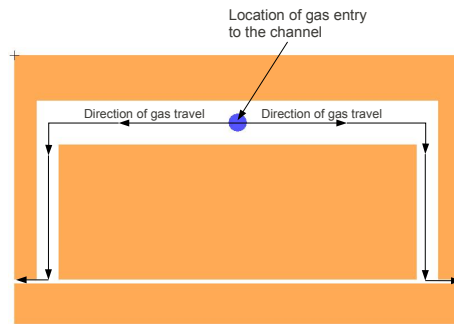
was different still from the pressure gauge on the main gas cylinders (not shown in the figure). In those cases we accepted the reading on the pressure gauge after the hand pulser (with 5% reading accuracy according to INRS staff) as the most accurate measure of gas pressure.

### 3.2.3 Passive Waveguide Targets

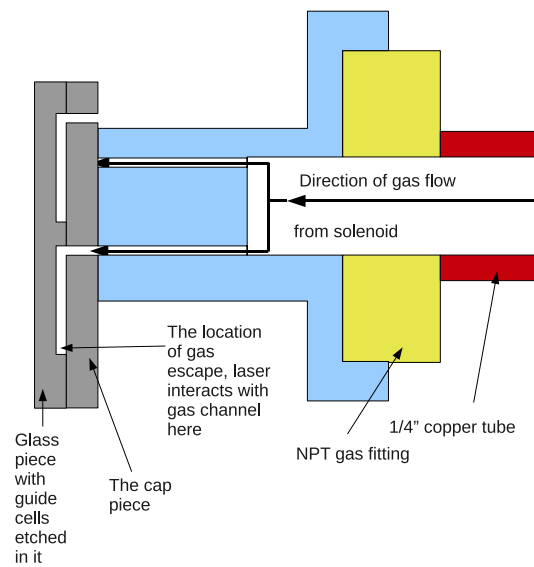
In these experiments we also used 10 mm passive capillaries (i.e. gas channels without electrical breakdown). These capillaries are made of two pieces of glass, bonded and annealed together. One of these pieces acted as a cap so that the gas would follow the path in the channel as indicated in Fig. 3.6a. The gas enters through the cap piece from the point of entry at the centre (filled circle). The wide channel allows the gas to flow freely to the ends of the capillary as shown. As gas escapes from the side, a stagnant gas channel with a nearly homogenous density in the centre is formed at steady state [65].

The cap piece was the glass substrate in contact with the gas feeder. A hole in this piece is matched to the gas feeder hole acting as an entry point for the gas. Other than this hole, which was drilled into the glass over plate using a water jet cutter in the machine shop, no other escape points existed on the cap piece to allow any leaks.

This gas cell is etched in columns in a 4" square glass piece using UV lithography and wet etch at the Nanofab facility of the Electrical and Engineering Department in University of Alberta (see Appendix A). The length of the gas guides in each column is kept constant so that the columns can be cut out at the end of the process with a diamond top saw. Guide widths within a column however are changed so that each column has several options of guide width ranging from  $400\mu\text{m}$  to  $800\mu\text{m}$ . The depth of each column (constant for the column) is determined by etch time and was either  $100\mu\text{m}$  or  $200\mu\text{m}$ . Several



(a)



(b)

Figure 3.6: Passive waveguide gas feeding structure. The common design cell is shown in (a) where gas flows in the capillary along the route indicated by arrows. The white space indicates the channel and the circle at the center indicates where gas is introduced to capillary. The cross section of the gas feeder apparatus is shown in (b). Gas enters the capillary through one hole while the other is sealed to the glass with a plastic o-ring



Figure 3.7: A series of waveguides on 4" long substrates were produced using nanofabrication methods

of these waveguide columns, cut from the same square substrate, are shown in 3.7. There are 13 waveguide rows on each 4" long column, with each feeding hole (shown as a blue circle in Fig. 3.6a) at constant distance of 6 mm from those on either side. Thus a worn target could be replaced with a new one by just translation of the column. This was necessary as it takes a long time to vent the chamber, put another target in, and pump down to vacuum again.

The gas feeder is shown in Fig. 3.6b. The gas flow is controlled by the same Parker valve as before, except that instead of a nozzle, an adaptor connects the solenoid to a length of copper tube attached to the gas feeder.

The gas feed was designed with two holes so that the two topmost guides and the two bottommost guides were accessible using the top and bottom holes respectively. The guides in the middle could be fed by either, but at all times one of the holes of the gas feeder would be flush against solid glass, where a plastic o-ring seal would prevent loss of gas as the other hole fed the gas into

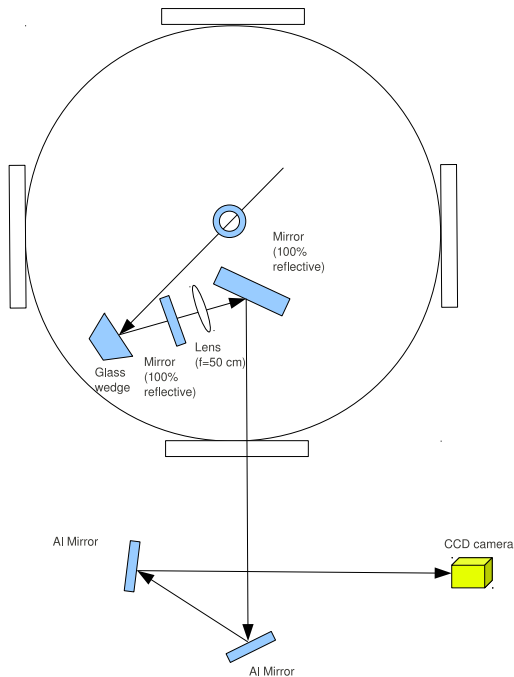


Figure 3.8: The output mode monitor setup

the guide. This was accomplished by having the distance between holes of the gas feeder mismatched with the holes in waveguide columns.

In these experiments, we used a 10 mm capillary channel  $600 \mu\text{m}$  wide and  $200 \mu\text{m}$  deep. The large cross section helps to minimize the interaction between laser and glass as this would modify the beam propagation considerably [66]. Even though we had capillaries which were 10, 20 and 30 mm long, we only had time to use the one described above.

### 3.2.4 Output Mode Monitor

One of our main optical diagnostics was the output mode monitor. This system was used to view the laser intensity distribution at the end of the interaction, referred to as the output plane of the gas targets. Its setup consists of a wedge

plate placed directly in the beam path after it interacts with the gas target, followed by an imaging setup as illustrated in Fig. 3.8. The 50 cm focal length lens of the imaging setup was followed by several mirrors guiding the beam outside of the vacuum chamber to a Point Gray Flea CCD camera.

The main challenge of working with this system was the high intensity of the laser beam which was enhanced when the beam was guided by relativistic self focusing inside the plasma. To reduce the intensity of the beam during high power shots, a 3/8 inch thick UV-grade fused silica (UVFS) mirror with high reflectivity at zero degrees was placed after the wedge to reduce the laser intensity by several orders of magnitude. The UVFS mirror affected the magnification of the imaging system. With it, the system had a magnification of  $M=5$  and when it was removed, the magnification increased to  $M=6.2$ .

The wedge plate and the mirror inside the vacuum chamber were controlled with motorized actuators, so when we wanted to measure the electron energies, we removed them from the beam path. As the wedge plate obstructed not only the laser, but the electron beam path as well, we were unable to simultaneously view the output laser mode and measure the energy of the generated electron beams. The output mode monitor however gave us a generalized view of how the laser pulse propagated in the plasma as will be shown in the results and discussion section.

In addition to observing the output mode of the laser after the interaction, this system was also used to view the shape of the focal spot in vacuum, by displacing the CCD camera by the appropriate amount.

### 3.2.5 New Electron Spectrometer

A new electron spectrometer (Fig. 3.9) was employed based on the same principles used for the spectrometer in 10 TW experiments; that is, permanent

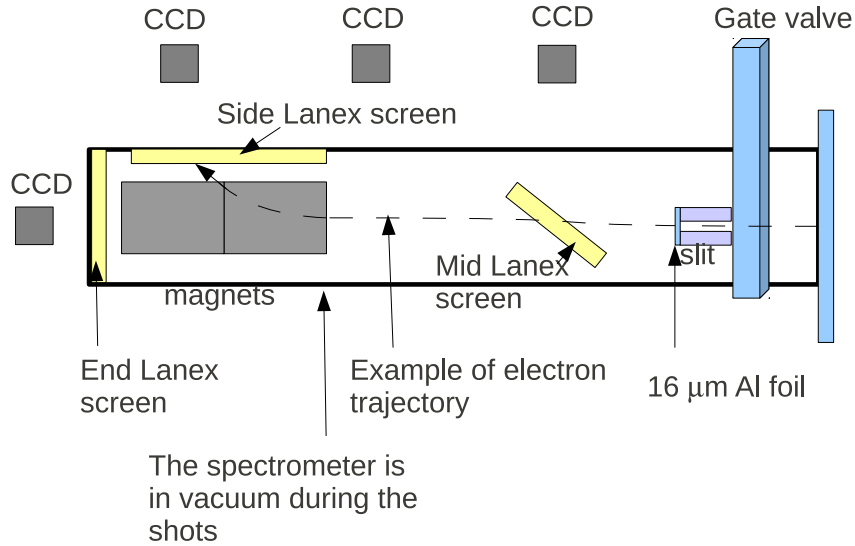


Figure 3.9: Schematics of the new electron spectrometer

magnets of 3 KG strength were used to disperse electrons according to their energy. The higher the electron's energy, the less it would be dispersed. Up to seven magnet units could be placed in series within the spectrometer housing, as opposed to just one in 10 TW experiments. Each magnet module was 12.5 cm long and had a 2 cm gap in their middle to let the electrons pass.

At this scale, Even electrons with energies of several GeVs would be deflected by centimetres after travelling over the nearly one meter of magnetic field. Fig. 3.10 shows calculated deflections of high energy electrons for different number of magnetic modules in the system.

Additionally, we used free standing Lanex screens in the path of the electron beams, which could indicate the direction and size of the electron beams. These mid screens were meant to be used for two purposes:

1. To give us some information about the pointing angle of the electron beams

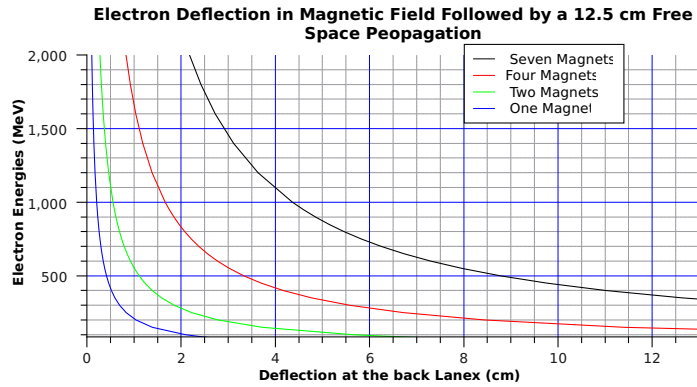


Figure 3.10: The electron deflection on the back Lanex calculated for different number of magnets.

2. To find out if it was possible to have a spectrometer setup without a lead slit. The lead slit is necessary to define initial angle and position of electrons as they enter the magnetic spectrometer. But as electron beams do not usually follow a consistent direction, several groups have chosen to remove the slit from their setups [21] [67].

Flexibility was an important factor in this set of experiments as it was our first experiments with a 100 TW class laser system. Although we expected electron energies as high as few GeVs, we also wanted to be prepared to measure lower energy electrons, should high energy ones prove difficult to obtain. Thus unlike the 10 TW system, the magnet yokes in this design had three open sides, so that the electrons that were not strong enough to make it to the end screen, could still be detected on a Lanex fluorescent screen on the side of the panel. An example of such trajectory is shown in Fig. 3.9 where an electron going through two magnets bends and hits the side Lanex. The three cameras watching the side of the spectrometer were Point Grey Chameleon cameras and the one watching the back Lanex was a cooled Andor Luca camera with higher sensitivity. We preferred to use the back Lanex because of the higher sensitivity

of the camera watching it. Thus we used four sets of magnets at most (usually only one or two) so that most of the electrons would hit the back Lanex screen.

Another important property of our spectrometer was ease of access to the configuration so that changes to the number of magnets or location of the Lanex film can be made quickly. The configuration was made accessible by one side which could be quickly removed. Additionally, it was provided with its own roughing vacuum pump, which allowed the spectrometer to be modified without venting the main experimental chamber which was separated from the spectrometer by a gate valve.

The laser light was blocked by an Al foil with the thickness of  $16\ \mu\text{m}$ . A layer of foil was placed between the spectrometer and gate valve connected to experimental chamber. The pressure between the two sides of the Al foil was equalized using a connection tube between them. Lanex screens were also covered by Al foils on their side facing the inside of the spectrometer to block the laser and room light from entering from that side.

### 3.2.6 Other Diagnostics

Other beam diagnostics included the use of optical probe beams which provided us with a transverse shadow of the interaction. The probe beam was taken from part of the main beam in the final compressor before the chamber and had a temporal FWHM of about 30 fs.

Our intention was to use the probe for interferometry as well, using a Wollaston polarizer outside the chamber, but there were two main problems which prevented us from doing so. First, the combination of inhomogeneous initial wavefront distortions and the number of filters used resulted in poor beam profile and lead to poor undisturbed fringes. The filters were necessary because of the strength of the probe beam which was required to be high to overcome

the intense plasma light generated during the interaction. Without filters, the scattered laser light and plasma emission would obscure our shadowgrams as we had previously observed on the 10 TW system. Second, in a Wollaston interferometer [68], the two beams with different polarizations diverge as they leave the prism leading to a few centimetres of separation between the centres of the beams at the plane of the CCD camera. Large diameter probe beams were required in order to give overlap and interference fringes between the two beams. The probe beams with the present setup turned out to be too narrow to give such overlap, even with the narrowest Wollaston angle (0.5 degrees) available.

Finally, like the 10 TW experiment, we used filtered scintillator PMT detectors to detect hard X-rays. These measurements could be used as a diagnostic of high energy electrons as further explained in section 5.2.

## Chapter 4

# Results and Discussion of 10 TW Experiments

In this chapter, the results of our experiments with the 10TW laser system at ALLS will be discussed<sup>1</sup>.

In earlier experiments we performed with the same system at ALLS [57], electron beams with energies between 10 to 50 MeV were observed in nitrogen and electron energies between 25 and 100 MeV were observed in helium. 2D PIC simulations also showed results that were consistent with the experiment. However occasionally, electron beams with very high electron energies (on the order of 200 MeV) were observed. It was postulated that the prepulse of the laser system creates a channel before the arrival of the main pulse. This channel would then create optimum conditions for laser guiding, increasing the interaction length and hence energy of the electrons.

Two methods were thus tried in these series of experiments to enhance the energy of the electron bunches. First, the level of prepulse was deliberately

---

<sup>1</sup>Large parts of this section have been previously published in [69]

increased by adjusting the timing of one of the Pockels cells in the laser system, generating a larger preplasma channel for the laser. Second, a longer focal length parabola was used in order to increase the acceleration length and hence the electron energies. The goal of this chapter of my thesis is to present a qualitative evaluation of the effect of these condition on electron acceleration.

## 4.1 The Prepulse Effect

Three types of prepulses exist in a high power laser system [58]. The first is the femtosecond prepulse (fspp) which arrives several nanosecond before the main pulse and is a low energy replica of the main pulse with the same time duration. Its intensity is about 5 orders of magnitude smaller than the main pulse. This prepulse leaks out of the regenerative amplifier one round trip (approximately 8 ns) earlier than the main pulse. The second is the nanosecond pedestal which is the leakage of amplified stimulated emission (ASE) signal. The ASE pedestals intensity is usually six to seven orders of magnitude weaker than the peak laser intensity but it is a long pulse (several nanoseconds in duration). Finally the third type of prepulse is the picosecond prepulse which is the slowly rising foot of the pulse arriving three to four picoseconds prior to the main pulse. The measurement from the third order autocorrelator for the 10 TW ALLS system is shown in Fig. 4.1. This figure indicates that the picosecond prepulse is five to six orders of magnitude smaller than main pulse.

Fig. 4.2 shows the photodiode signals of the nanosecond and fspp obtained during the experiments as described in section 3.1.1. Fig. 4.2a and 4.2b show nanosecond prepulses with a prepulse ratio of  $6 \times 10^{-2}$  and  $12 \times 10^{-2}$  respectively. Fig. 4.2c shows a fspp with a prepulse ratio of  $5 \times 10^{-5}$  relative to the main pulse signal.

Plasma channel generation could be started by the fspp, arriving 8.7 ns

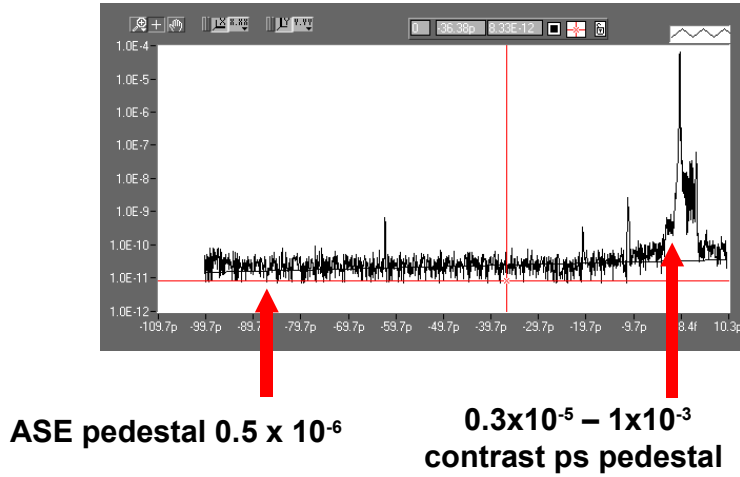
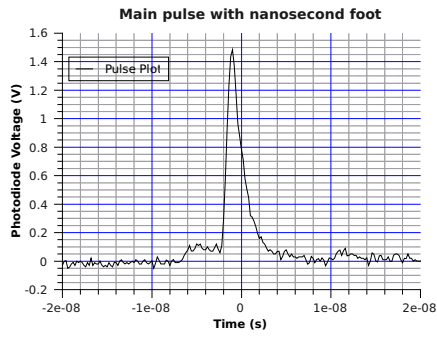


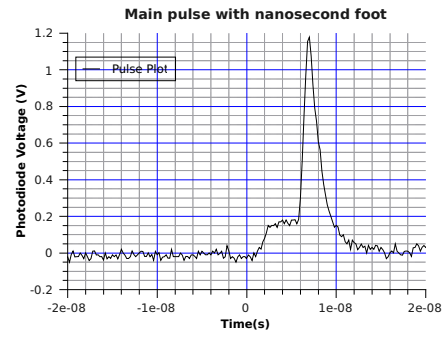
Figure 4.1: Third order autocorrelator measurement of ALLS laser system

before the main pulse. The calculated electron densities in the channel created by this pulse based on multiphoton ionization rates [70] are plotted in Fig. 4.3. These channel profiles are generated assuming that the prepulse followed the path of the main pulse. This is a reasonable assumption since the intensity of the prepulse beams are low enough that they are neither affected by ionization defocusing nor by relativistic self focusing. This plasma can then be heated by the nanosecond prepulse which is few nanoseconds in duration and relatively high in energy, creating a channel which can guide the main laser pulse. In such a “waveguide” the laser pulse can maintain its high intensity long enough for the self modulation of the pulse to lead to wave-breaking and injection of electrons into the wake.

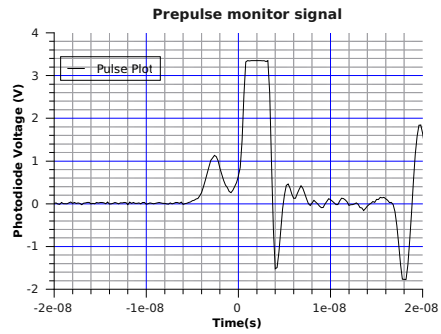
Increasing prepulse resulted in electron spectra such as Fig. 4.4. No significant increase in the mean energy occurred compared to previous experiments [57]. However, results obtained from different days of experiment indicated that the electrons bunches are generated easier when the prepulse levels are increased. For example on 090121, no electron bunch was observed at the lowest prepulse level with Pockels cell switching time of  $138 \mu\text{s}$  (main pulse energy of 370 mJ



(a) Lower nanosecond prepulse



(b) Higher nanosecond prepulse



(c) femtosecond prepulse

Figure 4.2: Examples of prepulse signals observed during the experiments. (a) and (b) show nanosecond foot and the main laser pulse for two different shots, where the level of prepulse was increased in (b). (c) shows an example of femtosecond prepulse

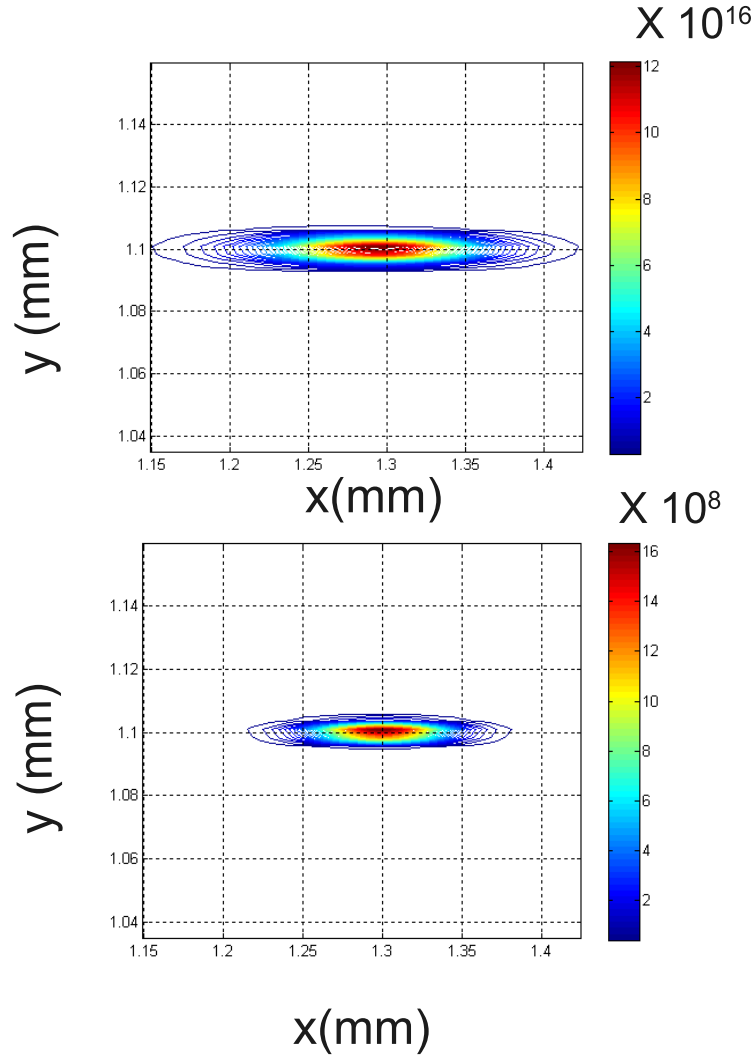


Figure 4.3: Contour plots of electron densities of preionized channels created by prepulses. A peak intensity of  $1 \times 10^{14} \text{Wcm}^{-2}$  is assumed for the prepulse. The plots are made using MPI rates for Helium (bottom) and Nitrogen (top) at backing gas pressure 1000 psi for both. The x-axis is distance along the axis of the laser with zero being at the center of the nozzle and y-axis is the transverse distance from nozzle surface. The laser is incidental from the right and is focused at 1.3 mm

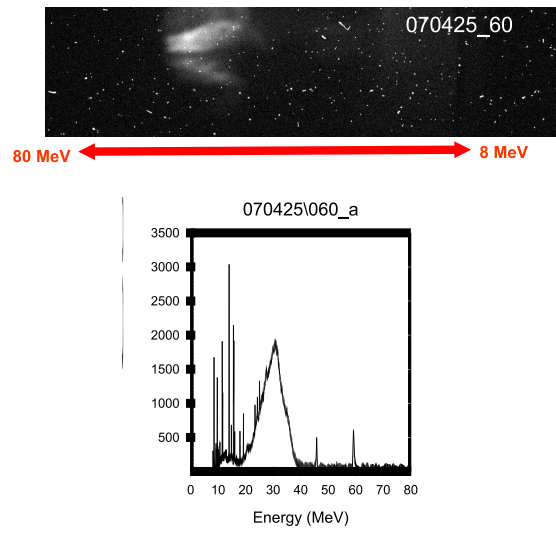


Figure 4.4: An electron spectra obtained with prepulse contrast of  $2 \times 10^{-5}$  with helium at 1100 psig ( $n_e \sim 4.6 \times 10^{19}$ )

before the compressor). Once the prepulse increased by decreasing the switching time to about  $134.25 \mu\text{s}$  (main pulse energy of 320 mJ before the compressor), the electron bunches appeared consistently. This corresponds to an increase in fspp contrast level from  $8 \times 10^{-6}$  to  $5 \times 10^{-5}$  and an increase in ASE prepulse power ratio of  $7 \times 10^{-3}$  to  $6 \times 10^{-2}$ . It is also important to notice how the main pulse intensity decreases with increasing prepulse as the Pockels cell timing is no longer optimized for highest intensity switch out. This effect can be seen in Fig. 4.2 where a nearly 100% increase in nanosecond pedestal led to 20% reduction in the main laser peak's intensity. In the same experimental day of 090121, the same decrease in switching time by  $3.75 \mu\text{s}$  caused 14% decrease in laser energy before the compressor. Such reduction in intensity resulted in lower wakefield amplitude and lower accelerating field. Thus even though higher prepulse leads to easier electron bunch generation, the reduction in laser intensities that ensues as a result of changing the Pockel cell somewhat cancels the effect and leads to lower energy electrons than possible with the optimum intensity.

Experimental evidence of the existence of channel before the arrival of the main pulse is seen in the time resolved interferograms in Fig. 4.5 where the small fringe shifts in the encircled area in Fig. 4.5 correspond to electron densities of  $\sim 10^{19} \text{cm}^{-3}$  in a small preformed channel. The length and the width of the channel roughly correspond to the calculated channel from multi-photon ionization rates (see Fig. 4.3). Furthermore, the fringe shift correlated with the progressively higher levels of prepulse (controlled by the Pockels cell timing). Similar effects of the prepulse have been observed by different groups, particularly by [58, 32].

## 4.2 Longer Focal Length Parabola

Since maximum energy gain is inversely related to density, most groups work at electron densities of few times  $10^{18} \text{cm}^{-3}$ . The electron density in our experi-

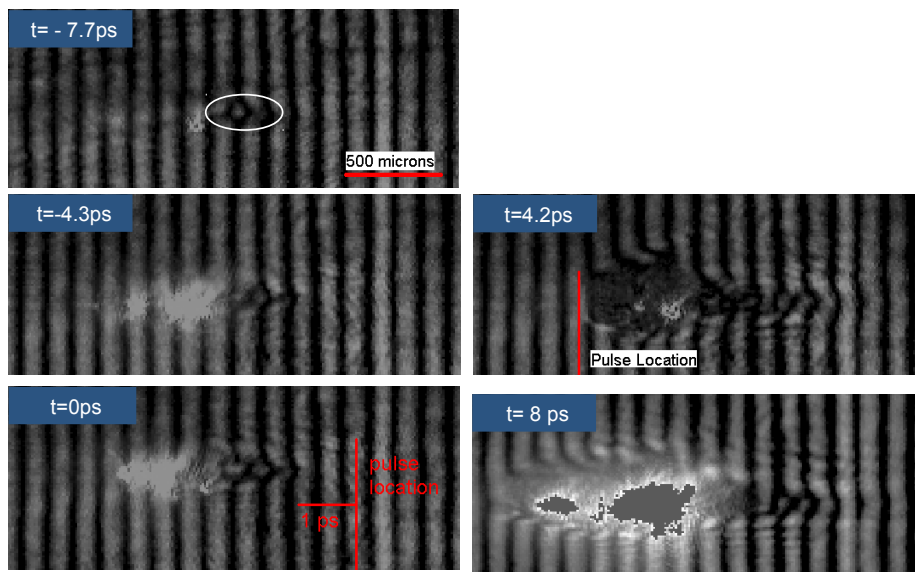


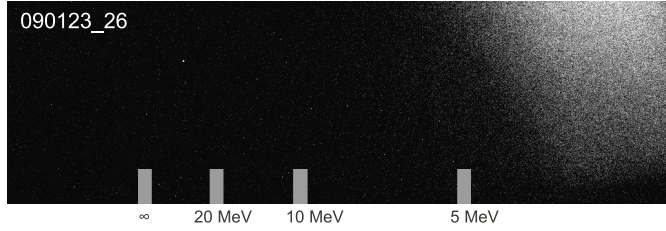
Figure 4.5: Time resolved interferograms of 6 TW pulse using a 15 cm focal length parabola and Helium gas at 1000 psi, with fspp intensity contrast of  $\simeq 5 \times 10^{-6}$ . The interferograms are recorded from 7.7 ps before the pulse arrives to 8 ps after. The preplasma generated is indicated with a circle in the frame for  $t=-7.7$  ps

ments was in the mid to high  $10^{19} \text{ cm}^{-3}$ . This density, which is about an order of magnitude higher than what most other groups use, was required probably to initiate wave-breaking which occurs easier at higher density since the nonlinear wavebreaking electric field amplitude (Eq. 2.27) is inversely proportional to density. i.e. wavebreaking threshold is lower at higher density.

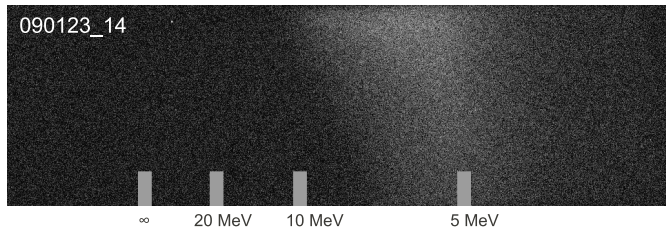
This problem was more significant with the long focal length parabola as longer focal lengths result in larger spot sizes and less initial intensity. Our goal was to increase the maximum electron energies using longer acceleration lengths, which scales with the Rayleigh range for low intensity beams [10]. However, using the 30 cm focal length f/12 parabola, results were only observed with  $N_2$  at 1000 psi ( $n_e \simeq 10^{20} \text{ cm}^{-3}$ ), and high levels of prepulse (fspp ratio of  $5 \times 10^{-5}$ ). In contrast, although high prepulse provided us with a parameter space for more frequent monoenergetic shots with the 152.4 mm focal length parabola, it was not essential for observing electron signals, as we could observe them at low prepulse level (fspp ratio  $\leq 10^{-5}$ ) as well. Furthermore, with the 152.4 mm focal length parabola, MeV electrons could be observed for electron density as low as a third of what was required for 30 cm focal length parabola. Evidently, with smaller focal spot, the laser beam could overcome the  $a_0 \geq 3$  threshold for injection (see section 2.3.1) easier and thus a smaller amount of prepulse is required to initiate injection at lower densities.

For the short focal length parabola we commonly obtained monoenergetic electron signals in the range of few tens of MeV, with a divergence of less than 10 mrad accompanied by occasional monoenergetic shots above 200 MeV as described previously [57]. For long focal length, however, we typically obtained a thermal spectrum as shown in Fig. 4.6a with an electron tail extending to around 8 MeV. We also observed occasional quasi-monoenergetic beams with energies of around 5 MeV as shown in Fig 4.6b.

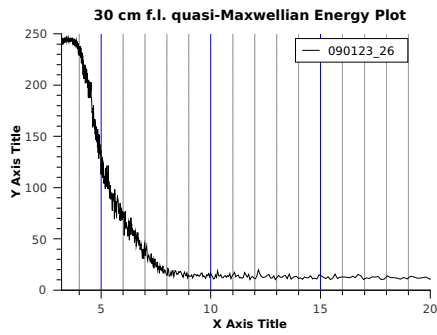
It appears that the increase in interaction distance is not sufficient to compensate for the decrease in accelerating field and difficulty in injection at low intensities. This makes it difficult to obtain quasi-monoenergetic electron bunches with 6 TW pulses and a 30 cm focal length parabola. This is in contrast to the 15 cm focal length parabola where the intensity is high enough to obtain good interaction conditions. In both cases optimization of the prepulse level was required in order to obtain good injection and guiding conditions.



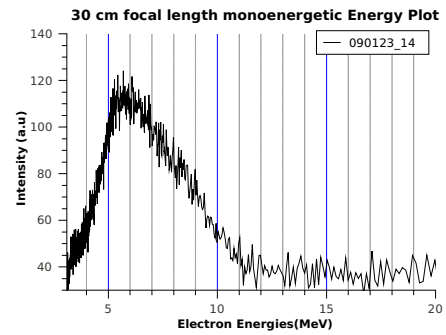
(a) Maxwellian type energy distribution



(b) Monoenergetic energy distribution



(c) quasi-Maxwellian profile



(d) Monoenergetic profile

Figure 4.6: Examples of monoenergetic and Maxwellian electron shots with nitrogen at 1000 psi  $n_e \sim 1.8 \times 10^{20}$  and high prepulse

## Chapter 5

# Results and Discussion of 100 TW Experiments

### 5.1 Electron Energy Calculation

The setup for the electron energy spectrometer, as detailed in section 3.2.5, allowed for electron energy to be calculated in two different ways. What these methods have in common is that the electron energy in both cases is determined by the amount of deflection in the magnetic field as detailed in section 2.7.

The first way involves using a slit to limit the spectrometer's angular acceptance. The slit is centered on the laser path and for sufficiently small opening, all electrons can be assumed to enter the magnets inline with the laser. Thus in terms of parameters used in section 2.7,  $\theta = 0$  and  $y = 0$  for these electrons. In our experiments we used a 5 mm slit exclusively, with horizontal acceptance angle of 5 mrad. There are clear computational advantages to this technique, as only one fluorescent screen at the end needs to be monitored and the input direction and angle of the electron bunches are unambiguous within error. The

Day	Number of Magnets	$\Delta x_{space}$ [cm]	Relevant section	Max Error at 200 MeV	Max error at 100 MeV
100302	1	12.5	<a href="#">5.2</a>	113%	34%
100309	2	12.5	<a href="#">5.3.1,5.3.2</a>	25%	10%
100310	4	12.5	<a href="#">5.3.1,5.3.2</a>	5%	3%
100316	1	52	<a href="#">5.3.1,5.3.2</a>	16%	7%

Table 5.1: Magnetic configuration used in different days including maximum error due to presence of slit.  $\Delta x_{space}$  is the distance of the last magnet from the back Lanex screen. See sections [2.7](#) and [3.2.5](#)

exact magnetic configuration for the different days where a slit was used is given in table [5.1](#). The limitation of this technique is that electrons have a large and unpredictable pointing angle, which means that few of the electrons comprising the bunch would actually go through the slit and some shots may completely miss the slit opening. This is one of the factors that may contribute to the error of data as far as average energy and percentage of shots yielding monoenergetic results is concerned. For example, if under a certain circumstance the opening of the slit is missed repeatedly (for example the said condition contributes to higher divergence of electron beams from the path of laser) the data may be misinterpreted since no electron signals are observed in the circumstance under question. This error is not considered in the statistical analysis of the present work and it is assumed that if a monoenergetic shot is produced, it makes it through the slit. This error however is something that needs to be considered in future experiments.

The second method of analyzing electron energies is to use two Lanex screens with the magnets placed between them. This method is similar to the method used in [\[21\]](#), except that in our case, the first fluorescent screen, mid Lanex screen in Fig. [3.9](#), is placed before the magnets in order to give a better overall view of the electron signals. The Lanex fluorescent screen before the magnets is

used to determine the initial position and angle of the electron beams as they enter the magnets. These variables are determined with respect to the laser beam path. One disadvantage of this method is that the initial position and angle of electrons has to be determined for each shot. This could be problematic as the position of the high energy electron beam on the mid Lanex may be ambiguous. There may be several electron spots on the mid Lanex screen or the high energy shot maybe a faint spot overshadowed by the equally bright low energy background electrons. The advantage of this technique however is that distribution of electron numbers and the presence of electron beams with large divergence can be viewed. This technique was used to collect data for sections [5.3.3](#), [5.4](#), and [5.5](#).

## 5.2 2.4 mm Gas Jet Results

We started out the experiments with the 2.4 mm exit diameter nozzle and helium gas. The energies of the electron bunches are shown in Fig. [5.1](#). Each data point represents the average of the peak of a quasi-monoenergetic beam. Shots with no electron signals and Maxwellian spectrum are removed from the data, except in the cases where all shots resulted in no electron signals, where zero MeV is assigned to them as their energy.

The energies of electron bunches is plotted as black circles with energies displayed on the left axis. The green curve is the theoretical maximum energy gain (Eq. [2.38](#)) for a fixed laser power of 6.0 TW. This graph is plotted for this energy in order to match the average data at  $n_e = 2.1 \times 10^{19}$ .

Even though an average power of 77 TW of power was used in these experiments, the electron bunches appear as though only one tenth of the power was used to accelerate them. The rest of the power was likely used in driving the wakes to the wave breaking threshold, or broke up into filaments and was

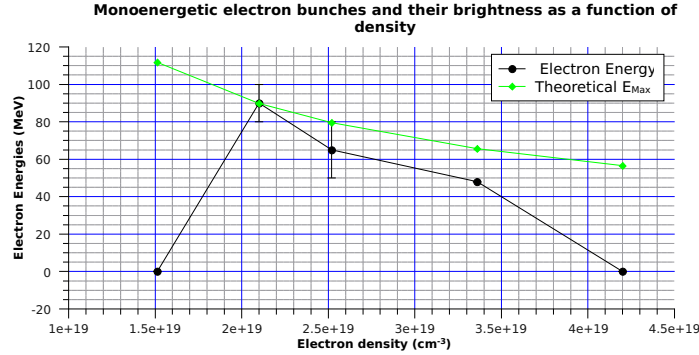


Figure 5.1: The data from the 2.4 mm gas jet and peak laser power of 77 TW

scattered.

A phenomenon that is observed from Fig. 5.1 is that the slope of the theoretical curve is shallower than the experimental curve and the distance between the points increases with increasing electron density. This effect starts from  $2.5 \times 10^{19}$  where the max energy predicted by theory matches the upper end of the experimental results and is particularly noticeable at densities above  $3 \times 10^{19} \text{cm}^{-3}$ . Since wave breaking electric field is proportional to  $n_e^{-1/4}$  (Eq. 2.27) and hence easier at higher densities, higher electron energy may be expected as electrons accelerate over their short dephasing length of few hundred microns. Dephasing length, depletion length, and plasma wavelength are plotted in Fig. 5.2.

This effect can be explained by the fact that as the electron density rises, the matched bubble radius decreases (in 1D linear theory, matched bubble radius is on the order of the plasma wavelength. See section 2.2). This in turn means that the laser pulse should undergo significant modifications in order for the laser spot size to shrink to such a small bubble spot size. Thus with increasing density, it may take longer for the laser to reach the condition of a stable self propagation channel. Additionally, dephasing and depletion lengths (see section 2.4) are smaller at higher densities. Although the depletion length is longer than

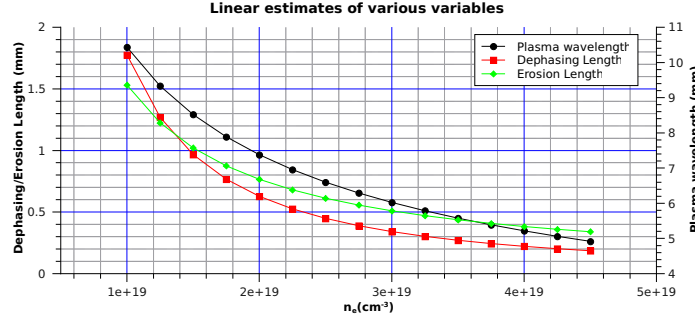
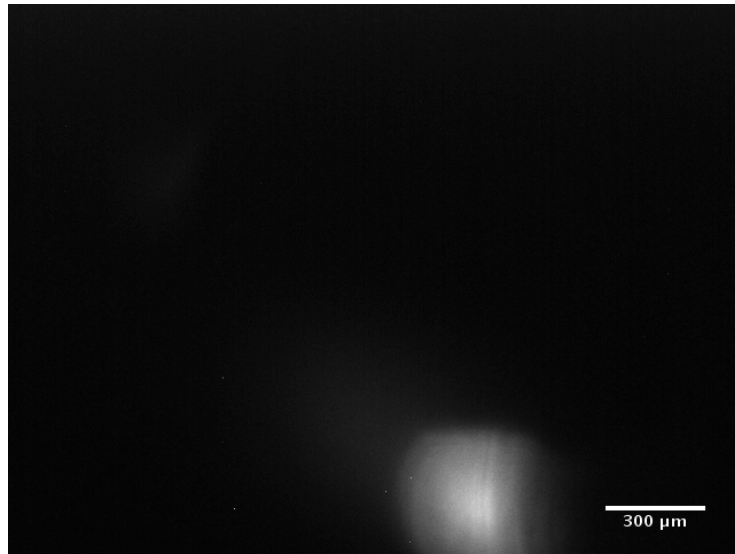


Figure 5.2: Parameters of laser wakefield acceleration according to theory

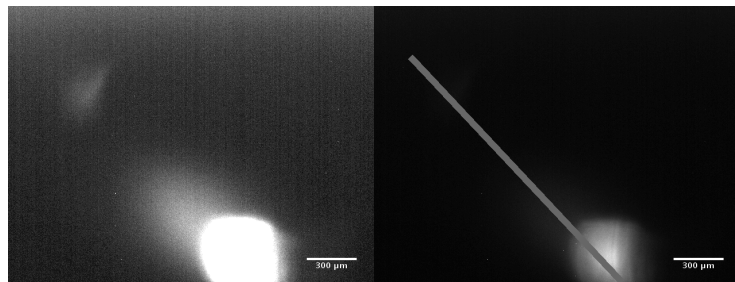
the dephasing length, dephasing is measured from the point of electron injection whereas the depletion length is measured from the initial wake setup. Thus, long distance of laser pulse modification for establishing of a self-propagating channel and shorter depletion lengths (proportional to  $n_e^{-1}$  from equation 2.31) could lead to acceleration being terminated before the dephasing length is reached. In addition, the longer length before electron injection could lead to reduced peak laser power and weaker wake electric field accelerating the electrons.

Another explanation for faster than expected decrease in electron energies with increasing electron density is that because of the smaller matched spot size for the self sustained propagation channel, a smaller amount of laser energy is guided into that channel and the rest is scattered, leading to weaker accelerating fields. Evidence for this latter explanation comes from observations of the top emission images.

An example of such image is shown in Fig. 5.3. The data set for all images shown is gathered in Appendix C. The images show a bright circle of emitted light of few hundred microns diameter (visible in Fig. 5.3a) followed by a large area of low intensity scattered light. At the end, there is another bright spot in the shape of a crescent (visible in Fig. 5.3b). Fig. 5.3c indicates where lineouts of different images are taken for comparison.



(a) Normal brightness



(b) Enhanced brightness

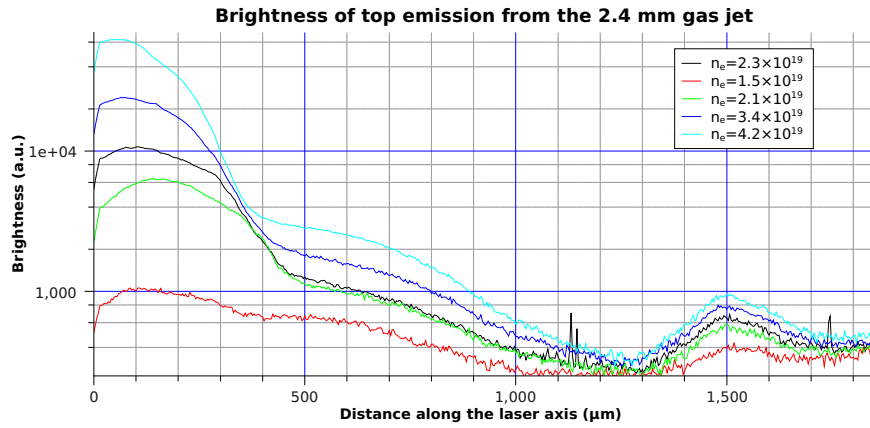
(c) Lineout trace

Figure 5.3: Example of top emission for 2.4 mm gas jet at  $n_e = 2.1 \times 10^{19} \text{cm}^{-3}$  (shot 100302\_74). The laser enters from the lower right and propagates forward towards the top left. All three images belong to the same shot

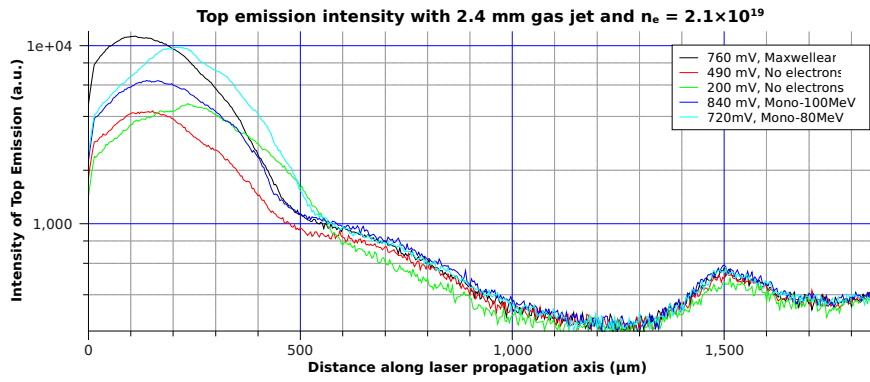
Lineouts for different shots are plotted in Fig. 5.4. From Fig. 5.4a, it is clear that as the density rises, the scattered light's peak intensity also rises dramatically. For example an increase by a factor of two in density (green to light blue curve) can cause an increase in maximum scattered intensity of an order of magnitude. This nonlinear rise in light scattering intensity with respect to density can be an explanation for the higher than expected decrease in electron energies with density rise.

It should be also pointed out that there is some variation in the top emission intensity observed at a given density. For example from Fig. 5.4b we can see that there is about a factor of 2.5 difference between the lowest and highest Thomson scattered intensity. Even so, the tendency of the emission intensity is to increase with density. Another feature to notice in Fig. 5.4b is that after a certain distance, the graphs are essentially identical. The consistency of the location of the crescent shaped feature (smaller peak) with respect to the location of the gas jet is very good (compared to the location of peak intensity for example). This probably means that the feature is linked to the gas jet and does not change unless the gas jet is moved. Judging by its location, it is probably the location of gas density down-ramp, which has been shown to be able to induce injection of electrons [34] and further side scattering of light. The PMT signal observed and the observed electron signals are shown in the legend of Fig. 5.4b. A qualitative relationship between electron production and maximum intensity of Thomson scattering may be seen as shots producing no electron results (henceforth referred to as null shots) produce much lower Thomson scattering. However, not enough data is available to establish a quantitative correlation between these two factors.

The PMT signal observed is plotted in Fig. 5.5 to show the relationship between high energy monoenergetic electron signals, electron density and gen-



(a)



(b)

Figure 5.4: Top emission images for 2.4 mm gas jet (a) for different densities and (b) for several shots for the same density. Axis of propagation is shown in Fig. 5.3c

erated PMT signals. The data points in this figure are for individual shots. The line of -100 MeV energy is reserved for the shots that resulted in a quasi-Maxwellian spectrum as opposed to a monoenergetic spectrum. For the shots that produced electron signals, the percentage of shots that resulted in Maxwellian spectrum, monoenergetic spectrum or no electron signals at all are shown in table 5.2.

Where no electron signals were observed (energy equals to zero line) we see two distinct regions. At lower density regions (up to  $2.1 \times 10^{19}$ ) we see the lowest PMT (less than 400 mV). At these points, no electron signals are seen probably because the density is too low for self-focusing to initiate electron injection over the length of our gas jet. When injection does occur at lower densities however, highest electron energies are observed.

The second region of no electron signals occurs at high density and is characterized by some of the highest PMT signals. With the evidence presented so far about the high amount of scattered light, I believe that these signals are generated by direct laser acceleration [71, 72] or stochastic acceleration [73] and not by the wakefield as high densities are known to do [72].

The total sum percentage of zero and quasi-Maxwellian spectrum stay relatively constant over the range of densities. However, no null electron shots are observed at density of  $2.3 \times 10^{19} \text{cm}^{-3}$ , where equal numbers of monoenergetic beams and Maxwellian spectrum are generated. This indicates that at this density self injection and acceleration consistently occur over the length of the plasma, but the shot to shot variation in experimental parameters is high enough to result in different electron energy spectrum. When high energy electron bunches are generated, the PMT is variable, but does not seem to present any clear patterns.

An example of a monoenergetic and Maxwellian signals at the electron den-

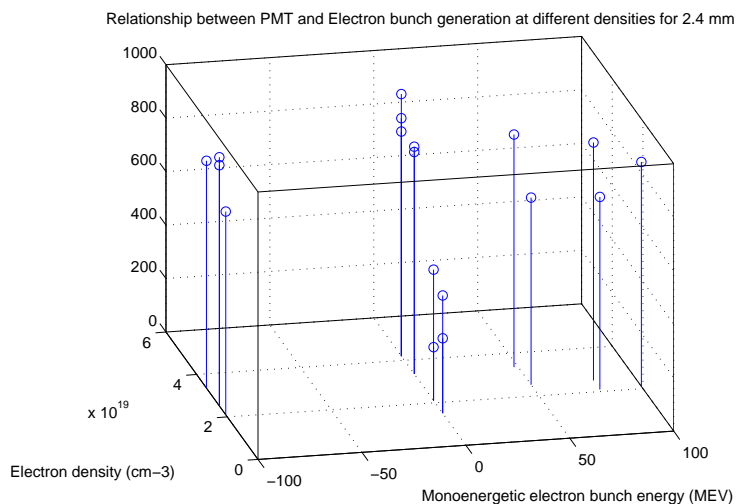


Figure 5.5: The PMT value recorded in electron density and electron bunch energy space are plotted. Electron bunch energy of -100 MeV denotes Maxwellian spectrum for electrons

$n_e$	quasi-monoenergetic beams (% shots)	Maxwellian spectrum (% shots)	no electrons (% shots)
$2.1 \times 10^{19}$	40	20	40
$2.3 \times 10^{19}$	50	50	0
$3.4 \times 10^{19}$	25	25	50

Table 5.2: The distribution of different behaviours of electron bunches according to their energies

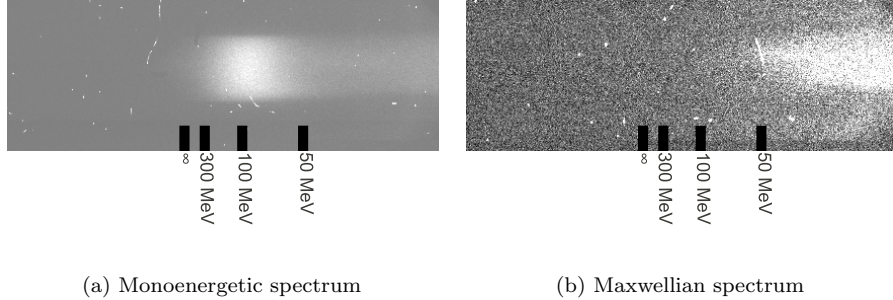


Figure 5.6: Example spectrum of electron signals using a nozzle with exit diameter of 2.4 mm. (a) is shot 100302\_74 and (b) is shot 100302\_77.  $n_e = 2.1 \times 10^{19} \text{cm}^{-3}$  for both shots and peak laser power is 77 TW

sity of  $2.1 \times 10^{19} \text{cm}^{-3}$  are presented in Fig. 5.6a and 5.6b respectively.

### 5.3 5 mm Gas Jet Results

We spent a large part of the experimental time with the 5mm gas jet targets. The study of the results with this nozzle will be separated into the following sections: In the first section I will present the features of the obtained electron bunches with helium gas targets. A discussion follows about the different trends in the electron signals and how they vary with different experimental parameters, mainly the plasma density and the depth of focus. Then I will present the results of experiments with nitrogen, either added as a high Z impurity in helium or used as the main gas for acceleration. Following that section, laser guiding over the length of the plasma will be examined. The laser mode was observed using a wedge and imaging system as described in section 3.2.4. Finally, I will present some observed characteristics of the acceleration process which need more investigation.

### 5.3.1 Electron Features Using Helium Gas Jet

Monoenergetic electron bunches with energies between 100 and 300 MeV were routinely observed from a pure helium gas jet with estimated densities of  $5 \times 10^{18} \text{cm}^{-3}$  to  $1 \times 10^{19} \text{cm}^{-3}$  in these experiments.

Some commonly observed features in electron beams are shown in Fig. 5.7 with horizontal profiles of the same images shown in Fig. 5.8. Lineout plots including vertical ones presented later in the chapter are made using binning of several pixels in ImageJ software, which takes the average of pixels in vertical (horizontal) direction for horizontal (vertical) profiles. For example images in Fig. 5.8 are horizontal lineout plots with 5 pixel binning in the vertical direction. The values on vertical axis are pixel count values with background subtracted for each image. Value of background noise for each figure is obtained by taking the average of pixels in an area on the left side of the images, where no electrons will be found. The standard deviation in these background noise levels is 27 counts for the images shown in Fig. 5.7.

Most electron beams observed had a monoenergetic spectra. Two examples are shown in Fig. 5.7a (lineout in Fig. 5.8a) and 5.7b (lineout in Fig. 5.8b) with 200 and 140 MeV peak electron energies respectively. A large number of the electron beams observed show multi-electron spots where one or more of the them have monoenergetic characteristics. An example of such is shown in Fig. 5.7c (lineout in Fig. 5.8c). Other times we would get a quasi-Maxwellian spectra with prominent features such as the signal shown in Fig. 5.7d (lineout in Fig. 5.8d). This last figure shows a peak in the quasi-Maxwellian background. In the analysis that follows, these signals are assumed to be composed of two feature, a quasi-Maxwellian super imposed with monoenergetic electron spots.

Occasionally, we got what appeared to be a very high energy electron signature with weak brightness, always accompanied by very strong secondary

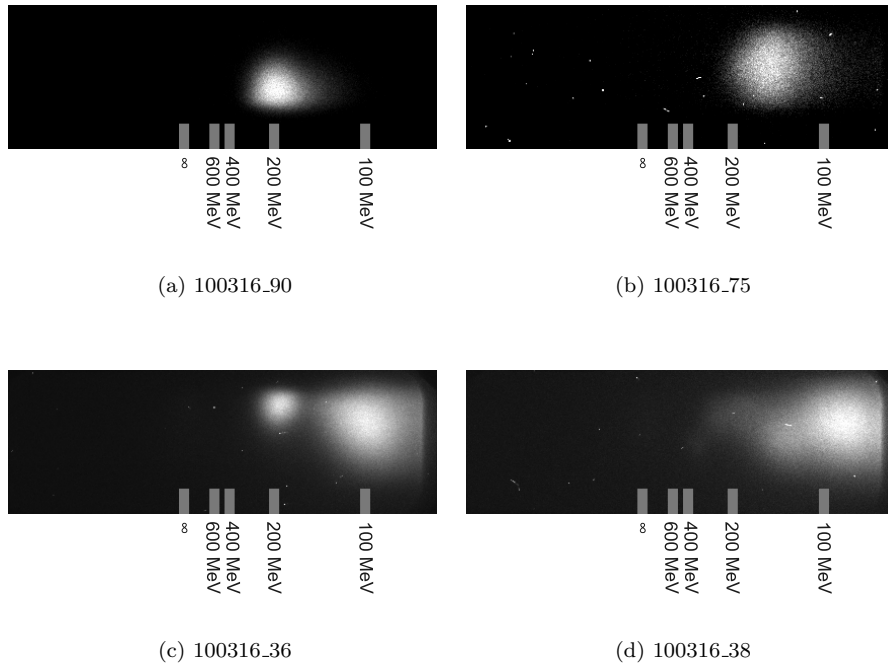
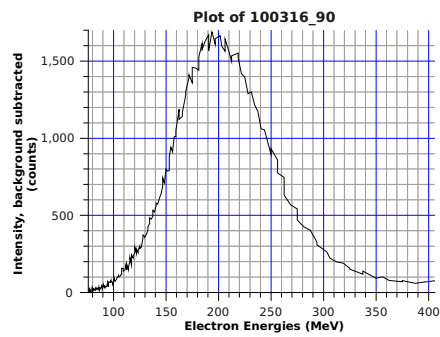
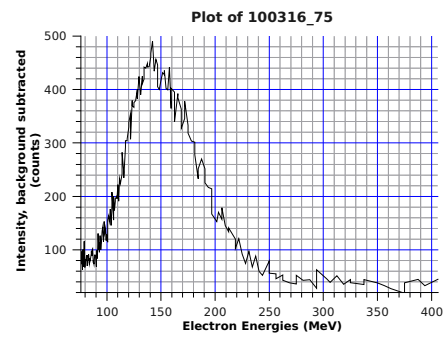


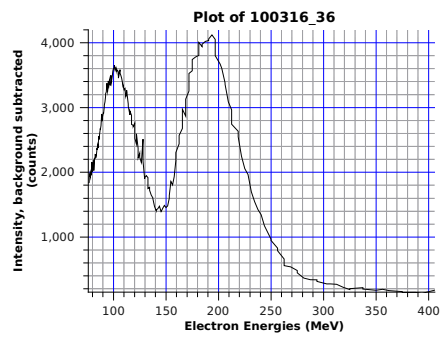
Figure 5.7: Commonly observed types of electron signals. (a) and (b) show monoenergetic signals. (c) shows a signal with two peaks and (d) shows monoenergetic spots superimposed on quasi-Maxwellian. Peak laser power is 77 TW and estimated electron density was about  $5 \times 10^{18} \text{cm}^{-3}$ . The electrons go through the mid Lanex screen before being dispersed by magnets



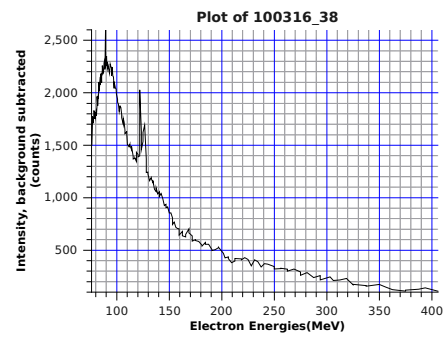
(a)



(b)



(c)

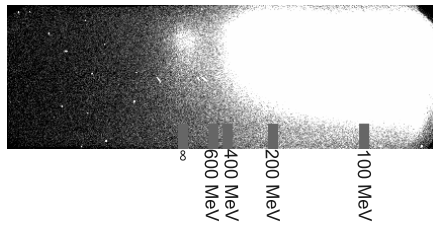


(d)

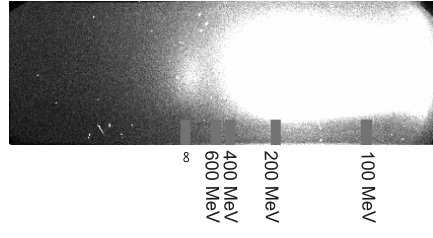
Figure 5.8: Horizontal plots for the commonly occurring electron features. (a), (b), (c), and (d) are horizontal outlines of 5.7a, 5.7b, 5.7c, and 5.7d respectively

electron signals. In what follows these will be referred to as the high energy features, even though they may not be electron signals as will be discussed. These shots appeared only a handful times during the duration of the entire experiment. Two examples of such signals with clear high energy feature are shown in in figure 5.9. The high energy features can be seen clearly in the high brightness images (Figs. 5.9a and 5.9b) while the low energy features at about 200 MeV (210 MeV for 100316\_33) can be observed in the low brightness figures (Figs. 5.9c and 5.9d). The brightness and contrast of the 5.9a and 5.9b have been individually adjusted to most clearly show the high energy features. The low brightness figures on the other hand are made at the same brightness. It can be seen then that the image on 100316\_51 (16,383 counts) is brighter than 100316\_33 (12,000 peak count) and has a saturated peak. The vertical profiles (Figs. 5.9e and 5.9f) are drawn for both high and low energy electrons with binning of 8 horizontal pixels. The intensities are normalized to one for each figure in order to compare vertical profiles of high and low energy electron signals. These figures show how high energy features are confined to a small divergence angle like the prominent feature.

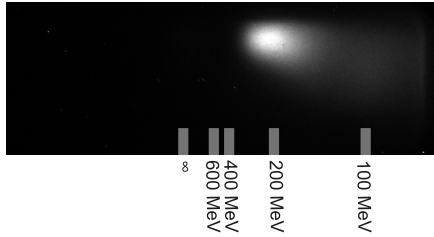
One possible explanation for these high energy features is X-ray emission. There were generally two kinds of X-rays observed. The first kind, betatron radiation [74], is the X-ray emission that results from the electrons wiggling inside the bubble. Due to the rounded nature of the bubble, electrons that are not trapped on the bubble axis feel a transverse force as well as the longitudinal one. Thus they oscillate inside the bubble back and forth across the bubble axis, generating the X-ray emission. We observed this radiation, shown in Fig. 5.10a, only when the middle Lanex screen (see Fig. 3.9) had been removed since the relatively low energy betatron X-rays are absorbed by the Lanex screen. The width of the betatron square signal is 1.1 cm which matches the expected shadow



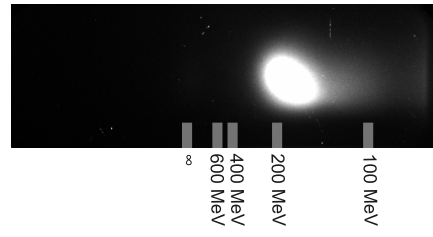
(a) 100316.33 with helium,  $n_e \sim 5 \times 10^{18} \text{cm}^{-3}$ , Enhanced image. Peak P = 78 TW



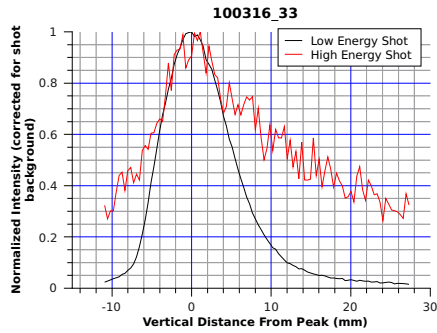
(b) 100316.51 with helium,  $n_e \sim 5 \times 10^{18} \text{cm}^{-3}$ , Enhanced image. Peak P = 76 TW



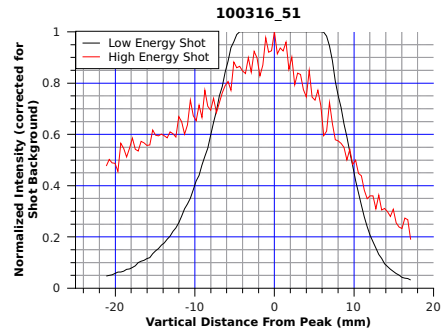
(c) 100316.33 Low brightness image



(d) 100316.51 Low brightness image

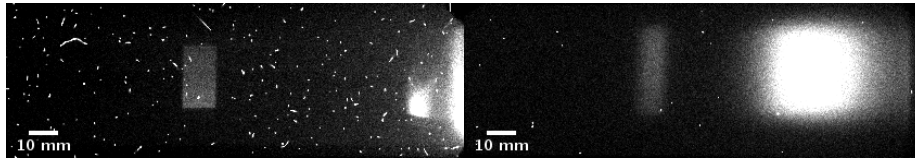


(e) Vertical profiles of 100316.33



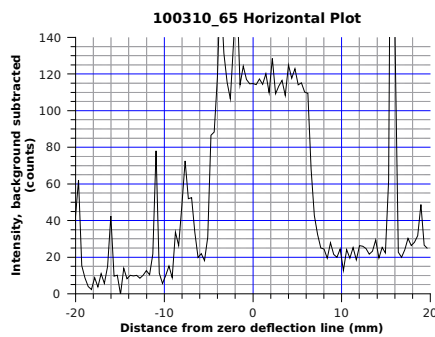
(f) Vertical profiles of 100316.51

Figure 5.9: Two rare shots with faint signal at high energy and prominent lower energy spot. (a) and (b) are high brightness images. (c) and (d) are low brightness images of (a) and (b) respectively. (c) and (d) have the same settings. (e) and (f) show vertical profiles of high energy and low energy features normalized to one and superimposed

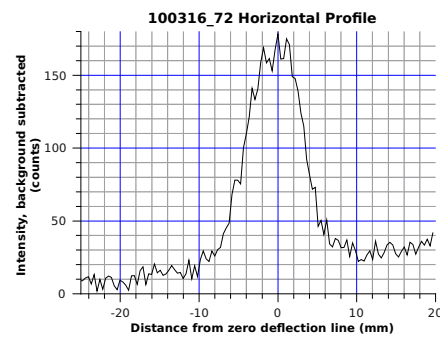


(a) 100310\_65. Magnets present without mid Lanex screen shows the betatron image

(b) 100316\_72. An image with magnets, mid Lanex screen, and glass wedge in electron path. Shows Bremsstrahlung radiation



(c) Lineout of the betatron image



(d) Lineout of the image with magnets, mid Lanex screen, and glass wedge in the way

Figure 5.10: X-ray shadows. (a) shows betatron radiation. (b) shows Bremsstrahlung radiation from Lanex screen and glass wedge in electrons path. (c) and (d) are horizontal lineouts of (a) and (b) respectively

of the 5 mm slit cast by a point source at the position of the target onto the back Lanex screen.

The second type of X-rays observed was generated from Bremsstrahlung radiation, where electrons interacting with matter generate radiation as a result of the deflection they experience when colliding with the positive ions in the matter. This radiation can be seen in Fig. 5.10b, where electrons hitting the glass wedge (put in to view laser profile) generates strong X-ray radiation which can be seen through the middle Lanex screen. In these cases, the X-ray spectrum extends into the MeV range which can penetrate through the glass plate and

Lanex film.

For the shots shown in Fig. 5.9 there was no glass in the electrons' path; but the mid Lanex screen was in the spectrometer. As Lanex screen absorbs betatron radiation, it is unlikely for the faint high energy feature to be of betatron radiation. It is possible however that they are Bremsstrahlung radiation resulting from the interaction of high energy electron beam with the mid Lanex screen or the 16  $\mu\text{m}$  Al foil used as light block. According to [75], the cone angle for Bremsstrahlung generation is dominated by multiple electron scattering given by [76]

$$\theta_{1/e}[\text{rad}] = 17.5(\beta cp[\text{MeV}])^{-1}\sqrt{\delta}[1 + 0.1^{10} \log(10\delta)] \quad (5.1)$$

Where

$$\delta = \frac{L}{L_R}$$

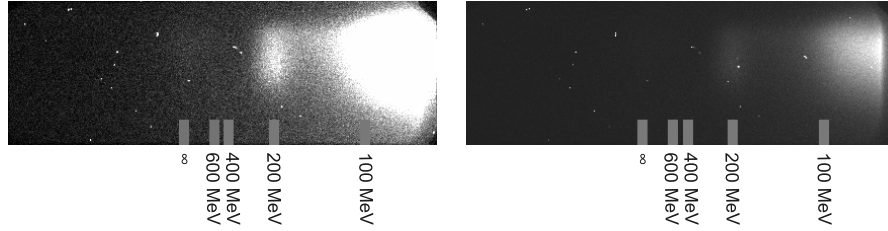
$L_R$  being the radiation length and  $L$  being the length of substance electrons travel through. Since  $p = \gamma mv$ ,  $E = \gamma mc^2$ , and  $\beta = v/c \sim 1$  then

$$\theta_{sc}[\text{rad}] \simeq \frac{17.5}{E[\text{MeV}]} \sqrt{\delta}[1 + 0.1^{10} \log(10\delta)] \quad (5.2)$$

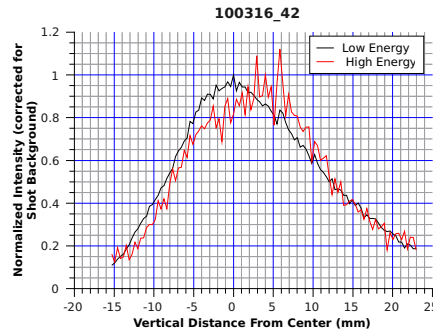
The Bremsstrahlung radiation cone angle is expected to be nearly equal to electron scattering angle. Moreover, If they are the radiation caused by the high energy bunches, the peaks should coincide in the vertical profile as magnets are only dispersive in horizontal direction. Looking at Fig. 5.9e, we see that the peaks of low and high energy shots coincide almost exactly above normalized intensity of 0.75. The plots do diverge for normalized intensity below 0.7 because of degraded signal to noise ratio. This degradation is due to two effects. First, the background levels and signal counts are very close to each other. The raw peak of high energy feature in 100316.33 (Fig. 5.9a) is 811 counts as opposed

to the background 591 counts. Therefore signal to noise ratio drops below one with normalized intensity at about 0.7. Second, the tail of the very bright lower energy electron signal adds to the noise in a non-symmetric way because the electron signals are not circular, but rather they have an oval shape. Even so, it is clear that the high energy feature resembles the low energy shot very closely in features. For example, in both, rising to the peak is shallow on the right side, while it is sharp on the left. Fig. 5.9f is added for the sake of completeness. As the low energy peak is saturated it is not possible to say whether the maxima coincide, though there certainly is a correlation between the peaks. Again the shallow rise lays on the same side. Further, the location of the high energy feature is less than 2 mm away from the projected center of the slit and overlaps it within the error imposed by the width of the slit. The projected center of the slit is obtained using the average of the central line of X-ray and undeflected electron images from different days. In summary, the very close resemblance of high energy features to the lower energy electron spots and vertical and horizontal position of the peaks, it is reasonable for these shots to be taken as X-ray signals.

On the other hand other images also present close vertical peaks between high and low energy electron bunches such as those observed in shot 100316\_42 shown in Fig. 5.11. Here, the difference is about 5 mm. This image is shown with two different levels of brightness and contrast in Figs. 5.11a and 5.11b to clearly show both features. The lower energy feature is not a clear spot as was the case in the other two images shown previously but it serves the present purpose as it is confined vertically. This image is particularly instructive since the high energy feature is undoubtedly electron signal, due to unambiguous and large deflection. The lineouts in this series were performed using 8-pixel horizontal binning and they are also normalized to one with respect to their



(a) 100316.42 with helium,  $n_e \sim 6 \times 10^{18} \text{ cm}^{-3}$ , Enhanced image      (b) 100316.42 Low brightness image



(c) Vertical profiles of 100316.42

Figure 5.11: 100316.42. (a) shows a high brightness image and (b) the same image with decreased brightness. The vertical profiles for high and low features are plotted in (c)

peak. Aside from the minor differences, the two profiles resemble each other very closely. This figure thus demonstrates that similar shapes of electron signals, though suggestive, does not necessarily mean that one is the X-ray image of the other. This being said, in the large majority of shots with multiple spots, the vertical position of spots are significantly different. For example the two peaks shown in Fig. 5.7c are nearly 6 mm apart vertically.

Taking the high energy feature as an electron signal, it is clear that its energy is well over 0.5 GeV from Fig. 5.9a. From the scaling equations (Eq. 2.39), we can estimate the acceleration length to be over 3 mm for a 600 MeV electron

signal with all 75 TW of power used for acceleration in a single channel whereas the depletion length is 2.5 mm (See Fig. 5.13 Where depletion length is plotted as a function of density). Furthermore, The theoretical maximum energy at the density of  $6 \times 10^{18}$  for 75 TW of laser power in a single beamlet is 470 MeV. However, such an electron signal as observed could perhaps be produced in a more complex process, involving first the acceleration of a large number of electrons to about 200 MeV and then a small group accelerated further. Such processes is not described by the simple scaling laws given earlier.

Multi-spot electron beams at high energies have also been observed by others [6, 11, 77] and have been attributed to effects such as beam loading, dephasing or hosing instability [46]. In simulations, multiple electron bunches can develop in two ways: a second bunch of electrons can be injected in the back of a bubble as an initial electron bunch is accelerated away from the back [11] or electrons may be injected in a second bubble travelling behind the first at the same velocity [6]. Similar feature can be seen in 3D PIC simulations presented in Chapter 6. High energy features with low charge were observed by [77] while [6, 11] observed higher energy features with higher charge, though no quantitative relationship can be established from the color contours. This may indicate that different mechanisms are responsible for creation of the weak high energy and strong lower energy bunch of electrons.

### 5.3.2 Electron Trends for Electron Produced by Helium Targets

This section pertains to investigating the dependence of electron energies on two major parameters: estimated electron densities and the location of laser focus in vacuum. For this analysis, only shots with monoenergetic electrons were considered. The peak of the monoenergetic spot (the energy with highest

brightness) is used as the energy of each shot. For shots with more than one monoenergetic electron bunch, the one with the highest energy is considered.

We had experimental data from pure helium on three days: 100309, 100310, and 100316. Data for each day is shown on separate graphs since laser and spectrometer parameters changed from day to day, but were constant during an experimental day.

### Variation with electron densities

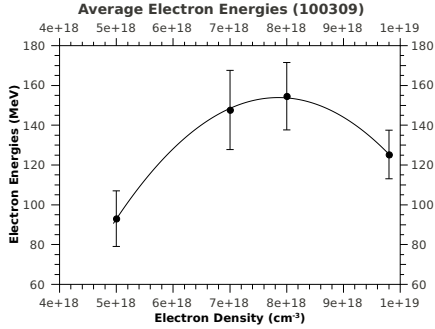
The variation of electron energies with electron densities is shown in the left column of Fig. 5.12. The data points are average energies and the error bars are the standard deviation of the mean ( $\sigma_x/\sqrt{(N-1)}$  where  $\sigma_x$  is the standard deviation and N number of points). For all the figures, a line or a parabola is fitted to the data. On 100309 and 100310, density was scanned over the range of  $5 \times 10^{18}$  and  $1 \times 10^{19}$  (Figs. 5.12a and 5.12c) while a finer density scan was carried out on 100316 (Fig. 5.12e) for densities between  $5 \times 10^{18}$  and  $6 \times 10^{18}$ . The data at each density point is a compilation of data at all focus depths combined. Focus depths are defined as the location of the vacuum focus spot with respect to the leading edge of the gas jet. Thus for example the focus depth of 2.5 mm refers to the laser being focused at the center of the gas jet in vacuum and 5.0 refers to it being focused at the edge of the gas jet farthest from the parabola. The reason for grouping focus depths together was that the average energies for individual focus depth over the range of electron densities overlapped with each other and also the number of monoenergetic shot at each particular density and focus depth was low ( $\leq 4$  shots). Therefore to establish a better statistical trends for electron energy over particular variables, these groups are combined. The same is done for the variation with focus depths, shown in the right column of Fig. 5.12 to be discussed in the next section. For graphs showing variation of parameters with focus depths, electron densities

are grouped at each particular focus depth. Figures for individual focus depths (and electron densities) as well as the number of shots for each day are added in Appendix B

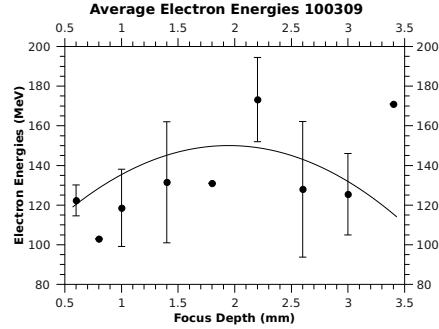
The theoretical variation of maximum electron energy with electron density is plotted in Fig. 5.13b using Eq. 2.38 and 76 TW as input laser power. Additionally plasma wavelength, estimated pump depletion length and dephasing length (From Eqs. 2.31 and 2.33) are plotted in Fig. 5.13a.

Comparing the data between 5.13b and the left column of Fig. 5.12, it is immediately clear that that the characteristics of the theoretical curve, increasing energy with decreasing density, are not shared with the experimental curves. In other words, whereas the electron energy increases by 60% as density is decreased from  $1.0 \times 10^{19}$  to  $5.0 \times 10^{18}$  in the theoretical curve, the experimental electron energies often undergo either decrease or stay relatively constant over the same range of densities. In fact none of the curves show consistently increasing energy with decreasing density. This inconsistency between theoretical and experimental characteristics of the peak energy of the quasi-monoenergetic beams may be due to a combination of several factors. At high densities, the lower wave breaking electric field (proportional to  $n_e^{-1/4}$  according to equation 2.27) allows the electrons to be trapped earlier in the acceleration process compared to lower densities. As the densities are decreased, the dephasing length increases significantly faster than the depletion length, such that at  $5 \times 10^{18} \text{cm}^{-3}$  the dephasing length is 5 mm, 1.6 times larger than the depletion length. The maximum energy curve in the figure 5.13b is plotted assuming that the electrons travel over their dephasing length. However with increasing injection threshold as density drops, the electrons inject later and do not travel over their full dephasing length and so do not produce the maximum energy predicted by theory.

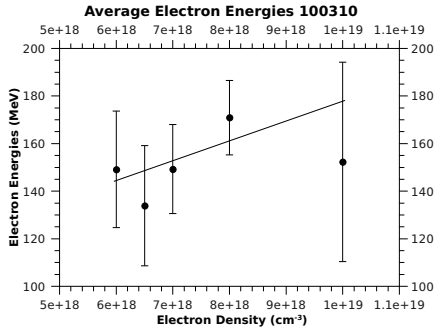
Also note the difference between the electron energies generated using the 5



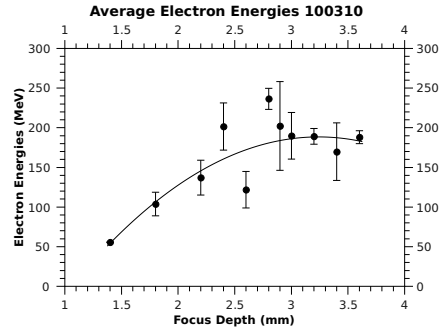
(a) Equation of curve:  $-7.5 \times 10^{-36}x^2 + 1.18 \times 10^{-16} - 309$



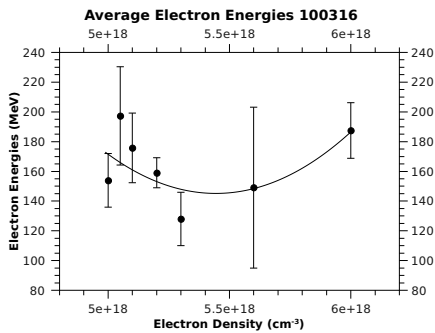
(b) Equation of curve:  $-16.3x^2 + 63.6x + 88$



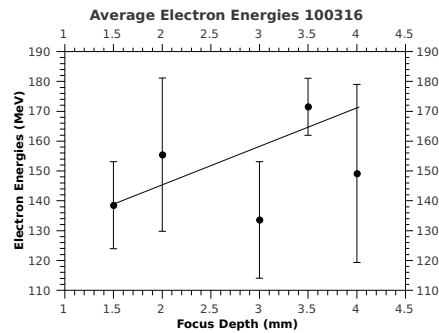
(c) Equation of curve:  $8.34 \times 10^{-18}x + 94.3$



(d) Equation of curve:  $-39.6x^2 + 256x - 272$

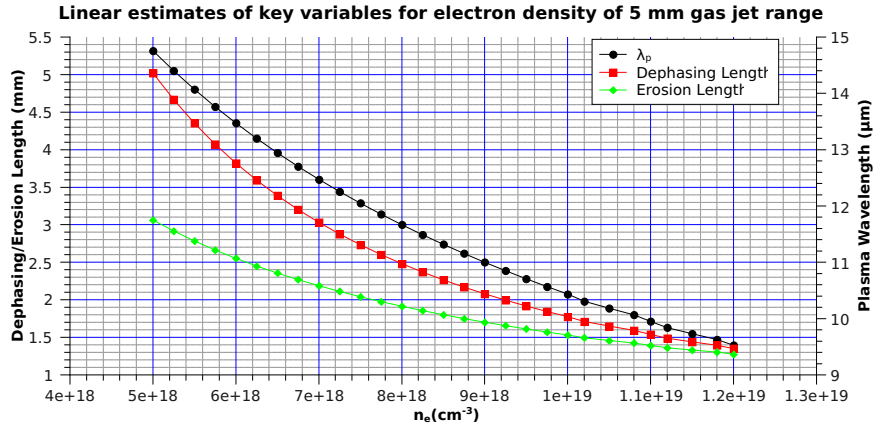


(e) Equation of curve:  $1.33 \times 10^{-34}x^2 - 1.45 \times 10^{-15}x + 4.1 \times 10^3$

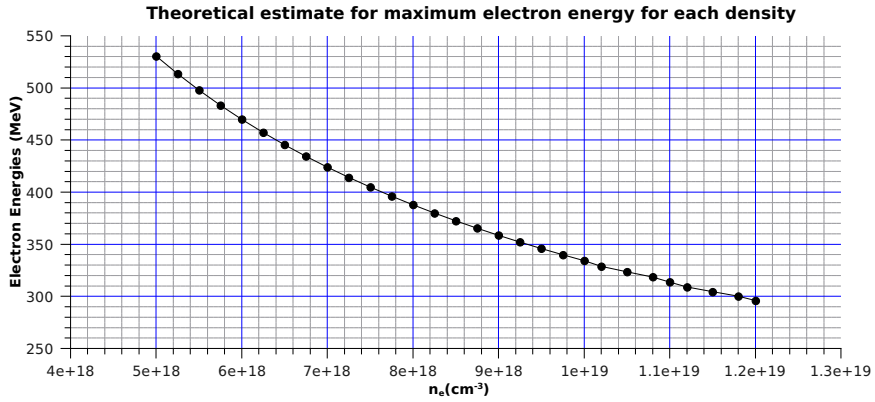


(f) Equation of curve:  $12.9x + 12.0$

Figure 5.12: Average of electron energies with changing density (left column) and focus depth (right column). Rows one, two, and three belonging to 100309, 100310, 100316 respectively. The equation for each curve fit to the data is in each image's caption.



(a)



(b)

Figure 5.13: Theoretical estimates of variables as functions of electron density. (a) shows plasma wavelength in black circles, dephasing length in red squares and depletion length in green symbols. plasma wavelength is read from the right vertical axis while depletion and dephasing length values are read from the left axis. (b) shows the maximum electron energy from theoretical estimates at different densities

mm gas jet and 2.4 mm gas jet in section 5.2. There is no lower bound on density below which electron signals were not observed. This is important because it means that lower densities and hence higher electron energies are achievable with plasma target of higher length under the same setup.

The large standard deviation of the mean in the data should be noted which in some cases is greater than 100 MeV (e.g. Fig. 5.12e). This large variation for shots under the same conditions is an indication of the variations in propagation of the laser pulse in the plasma. Evidence of this can be seen in Fig. 5.14 where the output laser profile is displayed for consecutive shots on 100316 in addition to the vacuum propagation mode of the laser shown in 5.14a. These images are recorded using the output mode monitor described in section 3.2.4. The output intensity distribution of the laser pulse shows a multitude of the “hot spots”, suggesting that there are a multitude of different and perhaps interfering electron beams generated, each having its own pointing angle. This means that at each shot the laser power is divided between filaments and the energy observed on the spectrometer may be any one electron bunch from the several that are generated during the laser plasma interaction. The light in these individual hot spots account for a few percent (six percent for figure 5.14d) of the entire laser profile’s brightness, which means that about 5 TW is channelled in that particular hot spot assuming 76 TW input laser power. The number of channels and the amount of energy concentrated in each is a variable that may contribute to lower than expected energies as well as shot to shot variability. In five out of the seven images, there is a distinct spot at the edge of the beam profile. The hot spots are not merely an intensification of features in the vacuum profile (Fig. 5.14a), suggesting that the regions of high intensity evolve during propagation and could be dependent on the intensity gradients as well as intensity. Finally, it is unclear how many of these spots correspond to electron beams, though some

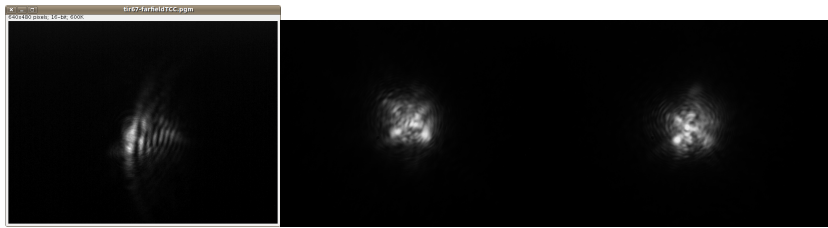
images from the Lanex screen set before the magnets shows multiple electron spots (see Fig. 5.15).

The percentage of shots yielding monoenergetic spots and quasi-Maxwellian spectra at different densities are shown in the left column of Fig. 5.16. The monoenergetic percentages are shown in black circles and quasi-Maxwellian percentages are shown in red squares. It can be seen from this figure that the percentage of electron shots yielding monoenergetic spectra increases almost linearly (most clearly seen in Figs. 5.16c and 5.16e) with decreasing density. This corroborates previous studies [23] that reported more consistent electron generation at lower densities.

### Variation with focus depth

The same data can be plotted as a function of focus depth (fd) as shown in the right column of Fig 5.12. This time, the data for different densities are grouped together.

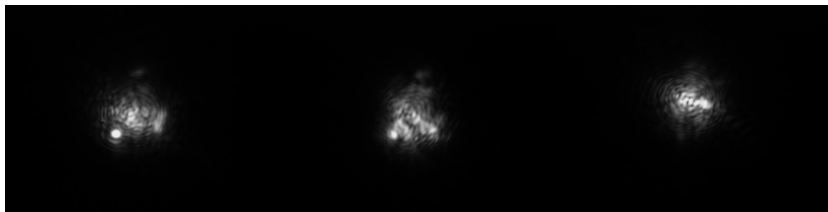
There appears to be a common trend in Fig. 5.12. That is, the mean average energy of electrons peaks around the center of gas jet ( $fd \sim 2.5$ ). This can be seen clearly in Figs. 5.12b and 5.12d and somewhat less clearly in Fig. 5.12f. for  $fd < 2.5$ , the average energy exhibits an increasing trend and above  $fd = 2.5$ , the average energy slightly decreases. Since this parameter has not been studied by any theoretical group that this author is aware of, I can only present qualitative explanations, while quantitative theoretical description will have to be provided in subsequent studies. The increase of the mean electron energies as the focus spot is moved deeper in the target can be explained in terms of different forces acting on the spot size, similar to what was done in [78]. When the focus spot is set deep into the gas jet, the natural convergence of the incoming beam helps the process of self-focusing and thus the the matched spot size of the bubble can be expected to be reached earlier in the acceleration process. Conversely when the



(a) Vacuum laser mode at the gas jet's exit plane

(b) 100316.63

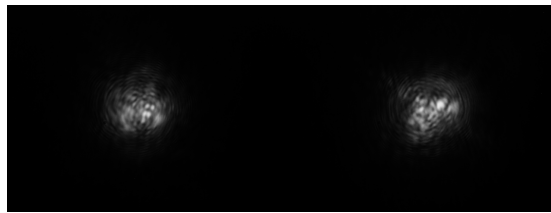
(c) 100316.65



(d) 100316.66

(e) 100316.69

(f) 100316.70



(g) 100316.71

(h) 100316.72

Figure 5.14: Exit plane images with 5 mm gas jet nozzle for consecutive shots on 100316. These images show some prominent features on the edge of the beam in addition to their central feature

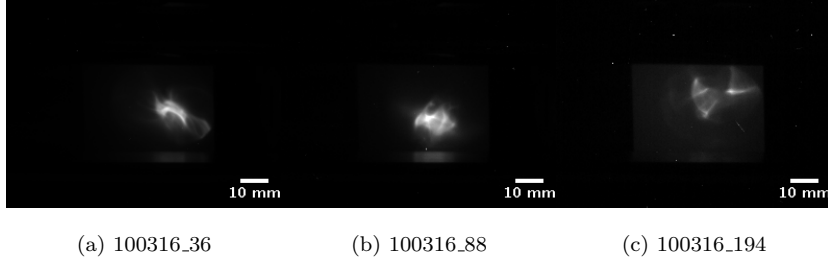


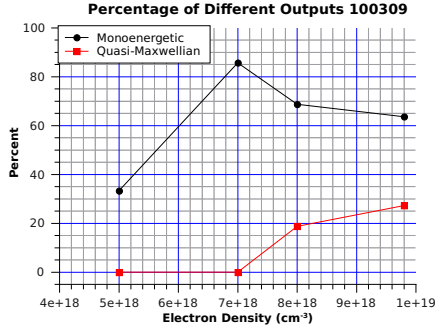
Figure 5.15: Example of several shots of mid Lanex which had multiple electron signatures, taken on the same day as 5.14

focus spot is near the leading edge ( $fd \simeq 0$ ), the self focusing has to fight against the divergence of the beam in addition to other sources of beam defocusing (see [78] and the references therein). It is unclear why the mean energy starts to fall slightly after this point. More detailed investigation is required to better understand the nature of the energy dependence of focus depth.

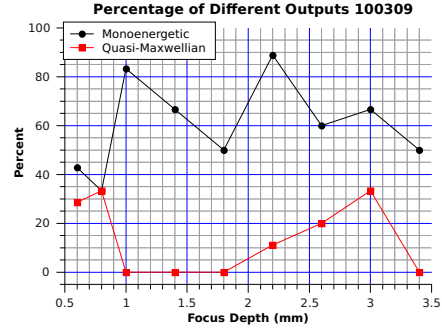
The percentage of shots producing monoenergetic spots (right column of Fig. 5.16) seems to follow a more or less similar trend as the average energy of electrons; that is, the percentage of monoenergetic shots peaks around the middle of the gas jet and starts dropping after that. Evidently vacuum focal spot position being in the middle of the gas jet contributes to the stability of self-focusing channel, increasing both the percentage and energy of the monoenergetic spot observed. The exception to this trend, seen in Fig. 5.16d and 5.16f, is the data from 100309 (Fig. 5.16b) where the percentage variation is relatively low over the range of focus depth.

### 5.3.3 Mixed Gas and Nitrogen Results

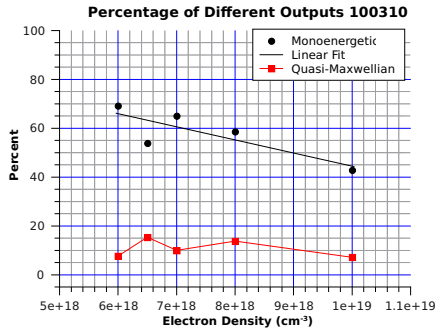
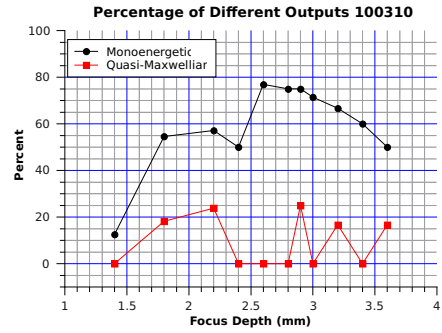
In addition to using pure helium as a gas target, we also added impurities in helium in the form of nitrogen in order to test ionization injection (see section 2.3.2). To do so we used the mixing chamber described in section 3.2.2. The elec-



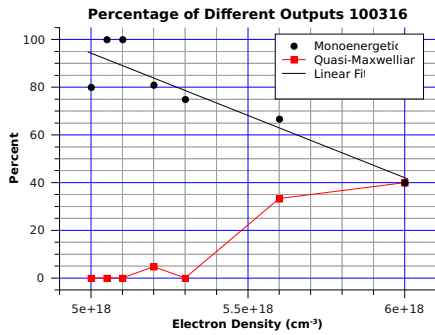
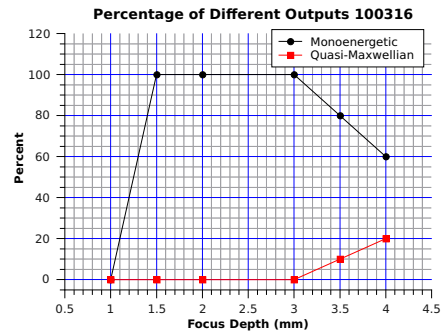
(a)



(b)

(c) Equation of Curve:  $-5.38 \times 10^{-18}x + 98.2$ 

(d)

(e) Equation of Curve:  $-5.22 \times 10^{-17}x + 356$ 

(f)

Figure 5.16: Percentage of monoenergetic and quasi-Maxwellian shots on 100309, 100310, and 100316 shown in rows 1, 2, and 3 respectively. Left column shows the percentage as a function of estimated electron density and right column as a function of focus depth

tron density is calculated using the initial partial pressures between the gases, assuming +2 and +5 ionization states for helium and nitrogen respectively. To reach lower percentage of nitrogen in the gas mixture in the experiments, an initial partial pressure state was established (5% or 10% nitrogen in the mix) and then helium pressure was increased in order to dilute the mixture. Due to slow leakage in our gas network, we didn't have precise control over the pressure values and determining exact percentage of nitrogen is not possible. Thus the electron densities presented are only estimates.

Similar to other experiments [24, 31], a large portion (14 shots out of 28) of the shots resulted in quasi-Maxwellian spectrum. This is to be expected since at full power,  $a_0 \simeq 1.8$  is greater than the value required for ionization and trapping of 6th nitrogen electron. So nitrogen electrons are injected early in the interaction and keep injecting into the bubble, leading to a thermal spectrum [31]

On the other hand, we also observed a large number (13 shots out of 28) of high energy monoenergetic electrons produced. The electron energies for these shots for different density is shown in Fig. 5.17 where the focused depths are written near each point. The focus depth for the series of shots with N<sub>2</sub>:He pressure near 10% was 2.5 mm. compared to Fig. 5.12, we see that in some instances the electron energy appears much higher than those produced by helium alone. One explanation is the effect of different method of electron energy measurement. Unlike pure helium results presented earlier, the electron energies here were determined without a slit. Thus we were able to determine the energies of electrons with much higher divergence angle (up to 14 mrad) with respect to the laser beam. Results in Fig. 5.17 indicates that the nitrogen electrons are trapped early in the wake formation and are accelerated over longer length, to much higher energies than helium of similar densities, where a sig-

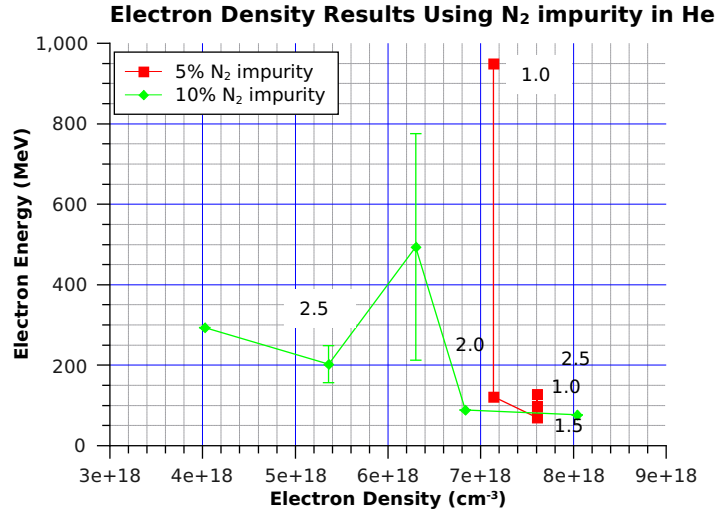


Figure 5.17: Electron energies with mixed gases and 5 mm nozzle. The focus depth of each shot is written next to its data point. the 10% nitrogen curve (the green curve) is exclusively taken at  $fd = 2.5mm$

nificant portion of energy may be depleted by the time wavebreaking injection occurs.

We also used nitrogen alone as a target with the 5 mm nozzle. The density range was between  $1.3 \times 10^{19} \text{cm}^{-3}$  and  $2.6 \times 10^{19} \text{cm}^{-3}$ . Out of the 26 shots taken on that day, 19 of them resulted in quasi-Maxwellian spectra with very low energies (under 30 MeV) and only three shots showed quasimonoenergetic features. The energy of these shots is shown in table 5.3. In comparison with helium at similar densities (table 5.2), a much higher percentage (73%) of the shots resulted in quasi-Maxwellian spectrum. This could be because of the low dephasing and depletion lengths which are all under 1 mm for density higher than  $1.3 \times 10^{19} \text{cm}^{-3}$  (Fig. 5.2) or it could be due to continuous ionization injection of the inner shell electrons of nitrogen. The exception to the rule, being the three monoenergetic shots, may happen under exceptional circumstances where a proper bubble forms and the electrons probably inject via the method

$n_e[\text{cm}^{-3}]$	Energy (MeV)
$1.3 \times 10^{19}$	55
$2.0 \times 10^{19}$	42
$2.6 \times 10^{19}$	34

Table 5.3: Energy of monoenergetic signals using nitrogen as the only target gas

of wavebreaking. Also the monoenergetic shots with nitrogen have lower energy compared with their similar densities in helium (Fig. 5.1).

These shots demonstrate how electrons can be generated with high Z gas such as nitrogen, which is demonstrated with 100 TW class laser power for the first time. Perhaps at the correct low density, the nitrogen gas could be singly used for both ionization injection and acceleration without the need of additional gases.

### 5.3.4 Laser Guiding

It has been shown recently [21] that the self injection of electrons through wavebreaking (section 2.3.1) occurs when the laser power exceeds a threshold of  $3P_c$  and is saturated at  $5P_c$ , where  $P_c$  is the critical power for self-focusing, calculated from Eq. 2.24:

$$P_c[\text{GW}] = 17 \left( \frac{\omega^2}{\omega_p^2} \right) = 17 \frac{n_{cr}}{n_e}$$

It was also asserted that laser guiding is limited by nonlinear pump depletion [13] which for the range of  $a_0 > 1$  is independent of laser power [22]. However a very limited range of  $P/P_c < 2.4$  was considered in experiments to arrive at that conclusion [13]. To investigate whether there is a similar limit on range of  $P/P_c$  for optimum laser self guiding over the range of the plasma target, we ran an experiment keeping the plasma density constant at  $3.4 \times 10^{18} \text{ cm}^{-3}$  (with

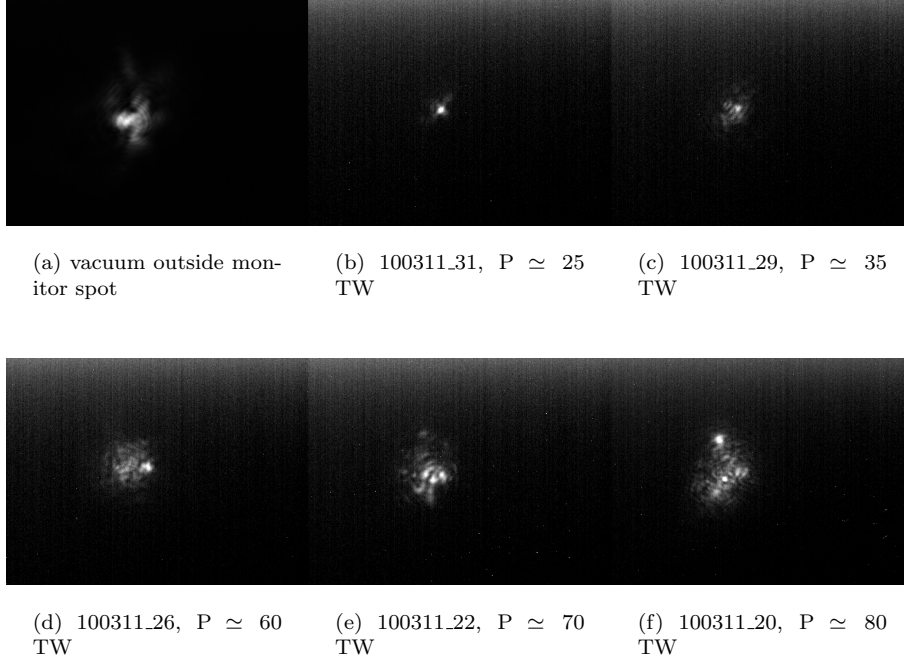


Figure 5.18: Output monitor images for varying laser energy with  $n_e = 3 \times 10^{18} \text{cm}^{-3}$

$\lambda_p \simeq 18 \mu\text{m}$  and  $P_c \simeq 8 \text{ TW}$ ) while we changed the laser energy. The results are shown in Fig. 5.18. It is clearly seen that as the laser energy increases from 25 TW ( $P/P_c \simeq 3$ ) to 80 TW ( $P/P_c \simeq 10$ ) the mode of the laser seen by the output monitor progressively degrades from a well collimated single channel in Fig. 5.18b to multiple filaments and beam breakup in Fig. 5.18f. This is in contrast with the recent conclusion that pump depletion, independent of laser power, is the limiting factor in laser guiding.

The reason for this discrepancy lies in the condition for stable self guiding of the laser given in section 2.2. For the linear and 1D nonlinear regimes ( $a \sim 1$ ), these conditions merely mean that the spot size ( $r_s$ ) should be on the order of the plasma wavelength. In 3D nonlinear case ( $a_0 > 2$ ), the condition for

P[TW]	$P/P_c$	I [ $W\text{cm}^{-2}$ ]	$a_0$	3D Nonlinear [ $\mu\text{m}$ ] from equation 5.3	$r_s$
25	3	$2.1 \times 10^{18}$	1.0	10	
35	4	$2.9 \times 10^{18}$	1.2	10	
60	8	$5 \times 10^{18}$	1.5	11	
70	9	$5.9 \times 10^{18}$	1.7	12	
80	10	$6.7 \times 10^{18}$	1.8	12	

Table 5.4: Values of matched spot size for powers used during the experiment with a vacuum focal spot of  $30 \times 35\mu\text{m}$  horizontal and vertical FWHM and  $\lambda_p = 18\mu\text{m}$

matched spot size is  $k_p r_s = 2\sqrt{a_0}$ , which in the matched spot size case can be written as [21]

$$r_s[\mu\text{m}] = 8.5 \times 10^6 (P[\text{TW}])^{1/6} \times (n_e[\text{cm}^{-3}])^{-1/3} \quad (5.3)$$

$$= 5.6(P[\text{TW}])^{1/6} \quad (5.4)$$

where  $n_e = 3.4 \times 10^{18} \text{ cm}^{-3}$  is used to get to Eq. 5.4. The values for the matched spot size according to equation 5.4 are given in table 5.4 for the laser powers used in the experiment.

For the guided mode 5.18b the spot size measures  $20 \mu\text{m}$ , which given the imaging system's  $F_{\#} = 20$  ( $f=50 \text{ cm}$ ,  $D=2.5 \text{ cm}$ ), is very close to the system's limit of resolution and this number may be closer to  $\lambda_p = 18\mu\text{m}$  as the nonlinear theory predicts for matching spot size. At this power, the relativistic and ponderomotive self focusing reduce the spot size to  $\sim 18\mu\text{m}$  and the pulse remains at this spot size until the end of the interaction. As the power is increased from 25 TW to 80 TW,  $a_0$  approaches the case better described by 3D nonlinear equation. Thus the matched spot size  $r_s$  starts to decrease from  $18 \mu\text{m}$  to values indicated in table 5.4, which are significantly less than  $\lambda_p$ . In other words, in the transition from the weakly relativistic to strongly relativistic case, the

matched spot size becomes too small and the conditions for stable self guiding over 5 mm can no longer be satisfied. This leads to the break up of the main laser into filaments of lower energy which individually have higher matched spot size requirements. Thus several stable channels may be generated as seen in Fig. 5.18e and 5.18f.

Furthermore it is observed from equation 5.3 that at higher powers, larger matched spot size is required to keep electron density constant or reduce it. A reduction in density is normally used at higher power in order to increase maximum energy gain which is inversely related to electron density (see section 2.5). Because of the relativistic self focusing effect, the final spot size can be significantly smaller than that of the input laser pulse. Nevertheless it is desirable for the sake of higher stability [23] to reduce the pulse evolution as much as possible which means larger spot sizes are better suited for bubble regime at higher powers, assuming  $a_0$  stays above 2.

In summary, laser guiding over 5 mm of plasma was observed for  $P/P_c < 10$ . It is shown that laser power plays an important role in that there is a range for  $P/P_c$  for which optimum guiding occurs and it is similar to the parameter space for optimum production of high charge electron bunches [21]. Best guiding was observed for  $P/P_c \leq 4$  and high  $P/P_c$  is observed to lead to beam breakup as the optimum matched spot size is too small to be reached by self-focused laser.

### 5.3.5 Other Features to be Further Investigated

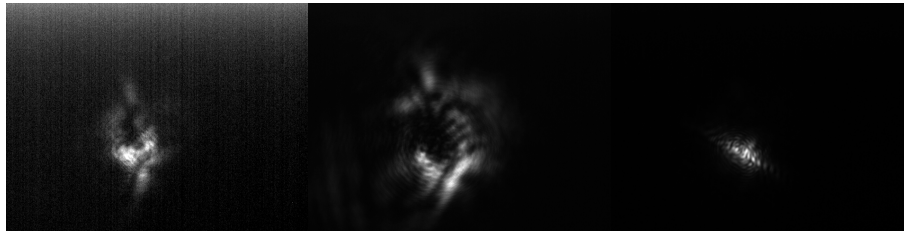
During one of the days that the mode was observed, a number of modes appeared to have a ring structure. These modes are displayed in Fig. 5.19. It appears that the structure does not depend on density alone; since for example Fig. 5.19d and 5.19e are taken with exactly the same conditions, but one gives a fairly well guided mode, while the other has a pronounced ring structure to

it. Nor are the ring features merely intensified versions of the vacuum shots since for example Fig. 5.19i shows strong features at the top while the strong features of the vacuum focus spot (Fig. 5.19a) are all at the bottom half of the ring. A strong dependence on plasma density is not observed since a comparison between Figs. 5.19h to 5.19d shows that the output modes are similar (i.e. same size and similar dominant features) at densities varying by a factor of five.

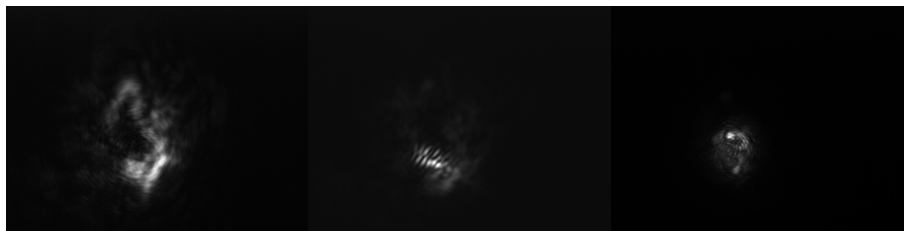
It is important to note that Fig. 5.19a clearly shows a different vacuum spot compared with Figure 5.19b, which was taken later in the shot. Hence this effect may be a mere result of variations in the laser pulse profile. It is possible for example that due to a malfunction of phase correcting mirror, a large portion of the laser light was concentrated on the edges as evidenced by the vacuum mode in Fig. 5.19b, leading to self focusing away from the center and near the edge of the beam.

Another possible explanation may be given based on observations from PIC simulations (see chapter 6). In these simulations, a large spot size undergoes strong self focusing where its spot size is reduced to the matched spot size for the simulation density. A similar ring structure is seen in the simulation as the laser undergoes spot size modification. Therefore this may be a common feature in the accelerating structure and we simply chanced to see it. An example of the mid Lanex screen signal is shown in Fig. 5.19k. Presence of electron spots forming a ring around a central spot can be seen in this image. Follow up experiments are needed to obtain a better understanding of the causes for appearance of these rings.

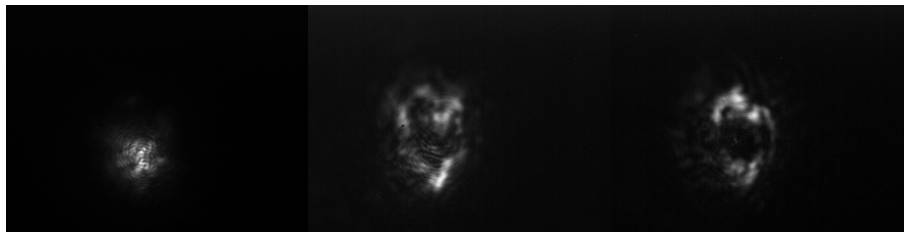
On a side note, Figs 5.19c, 5.19f, and 5.19g show once again that as the density (and thus  $P/P_c$ ) rises the guided mode degrades, which is in agreement with the results of section 5.3.4.



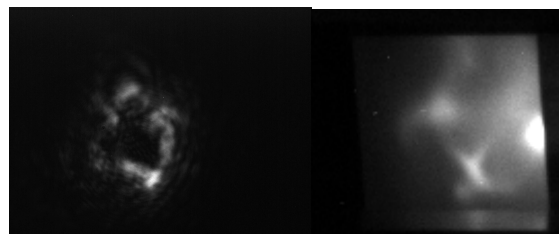
(a) vacuum shot 100312.3 (b) vacuum shot 100312.85 (c) 100312.7, He 200 psi



(d) 100312.83, He 200 psi (e) 100312.84, He 200 psi (f) 100312.29, He 400 psi



(g) 100312.9, He 600 psi (h) 100312.67, He 600 psi (i) 100312.73, He 800 psi



(j) 100312.78, He 1000 psi (k) 100312.26, The image on Mid Lanex, He 400 psi

Figure 5.19: This figure shows that the ring effect is dependent on the nature of the initial beam.

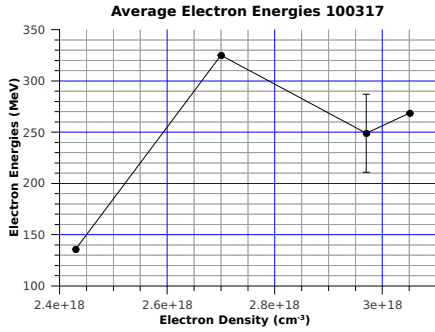
## 5.4 10 mm Gasjet Results

On March 17, 2010, we installed the gas nozzle with 10 mm exit diameter. The average energies as a function of electron density and focus depth as well as the percentage of shots yielding monoenergetic results are shown in Fig. 5.20. With the 10 mm nozzle, we entered a parameter space of experiments where the percentage of shots yielding any electron signals dropped to zero. This density threshold which is about  $2 \times 10^{18} \text{ cm}^{-3}$  probably constitutes the lower limit of density for wave breaking injection. Below this point, the wake amplitude stays below the level of wave breaking injection. Where there are electron bunches generated, we observe the drop of energy with decreasing electron density which has the same causes previously discussed in section 5.3.2.

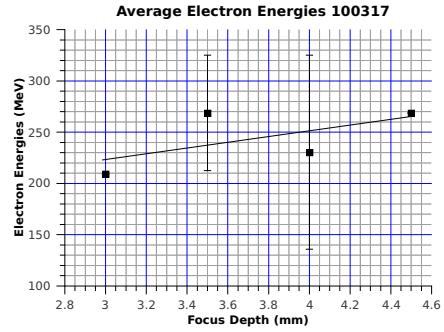
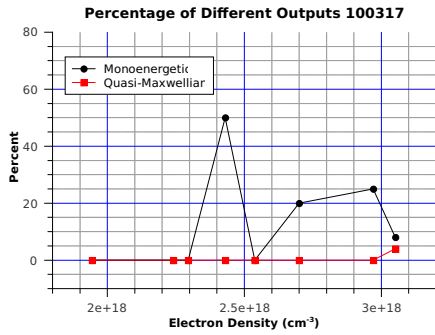
The data from Fig. 5.20d shows a similar trend for the percentage of monoenergetic shots obtained with the 10 mm nozzle as the percentage obtained with the 5 mm gas jet target. The electron signals are not generated for  $fd > 6.5$  and  $fd < 2.5$ . The trend in the range where electrons are generated favours a peak near 4 mm focus depth. Similar to 5 mm gas jet targets, focusing the laser near the center of gas jet seems to have a stabilizing effect on electron generation. Where electrons are generated, electron energies change very little over the range of focus depths, though there is a tendency towards higher energy with deeper focus depth as was observed also in section 5.3.2.

## 5.5 10 mm Passive Capillary

Although we had multiple lengths of the passive gas capillary tubes, we only used a 10 mm long cell with the width of  $200\mu\text{m} \times 600\mu\text{m}$ . The main advantage of the capillaries is at lengths higher than 10 mm, where it becomes impractical to use gas jets as the densities become too low for high pressures. This round



(a)

(b) Curve Equation:  $28.0x + 139$ 

(c)

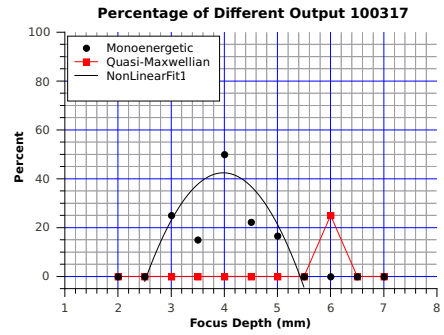
(d) Curve Equation:  $-4.37x^2 + 36.8x - 5.45$ 

Figure 5.20: 100317 10 mm gas jet data. (a) and (b) show the average electron energy as functions of electron density (left) and focus depth (right). (c) and (d) show the percentage of shots yielding monoenergetic (black circles) or quasi-Maxwellian spectrum (red squares) as functions of electron density (left) and focus depth (right)

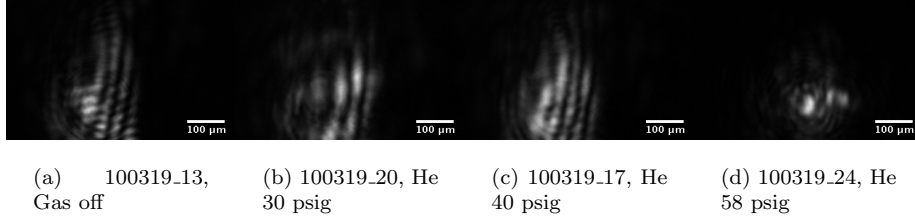


Figure 5.21: Laser modes at the output of the interaction from the waveguides at different backing pressures of He gas for a pulse power of 77 TW

of the experiments however was carried out primarily as a proof of principle experiment to get some experience in working with capillaries.

The images from the output mode monitor (Fig. 5.21) indicate that there is a guided mode once the gas density crosses a threshold. This mode does not appear when there are no gases in the guide or when the pressure is too low. Instead some lines appear that are most likely the result of the diffraction of laser light from the edges of the waveguide. This is a clear indication that guiding is the result of the plasma generated by photoionization of the gas and not glass elements. Furthermore, assuming that the results of section 5.3.4 for the guided mode apply to our capillary,  $1 < P/P_c < 4$  can be used to estimate the density of electrons. This gives an estimate for electron density of  $3.7 \times 10^{17} < n_e[\text{cm}^{-3}] < 1.5 \times 10^{18}$  for the laser power at 77 TW. The guided spot in 5.21d is 28  $\mu\text{m}$  FWHM which using the equation for matched spot size in nonlinear wakefield regime (Eq. 5.3) gives  $n_e = 4 \times 10^{17} \text{cm}^{-3}$  which is in agreement with the conditions for laser guiding.

Three monoenergetic shots were observed with the capillary cells out of the twenty shots taken. The low number of monoenergetic electron bunches appearing also indicates that we are at the threshold of injection which is consistent with the low density estimated. Two monoenergetic shots (100 and 150 MeV) appeared at 200 psig, and one (200 MeV) appeared at 350 psig. Assuming linear

variation in electron density with respect to pressure, and assuming (from the discussion in the previous paragraph) electron density of  $n_e = 4 \times 10^{17} \text{cm}^{-3}$  for backup gas pressure equal to 58 psig, the electron density was approximately  $1.4 \times 10^{18} \text{cm}^{-3}$  and  $2.1 \times 10^{18} \text{cm}^{-3}$  for 200 and 350 psig respectively. Eq. 2.38 predicts a maximum theoretical energy of 980 MeV for  $2.1 \times 10^{18} \text{cm}^{-3}$  with 77 TW laser power and pulse depletion and dephasing lengths of 7.7 mm and 20 mm are predicted by Eqs. 2.31 and 2.33 respectively.

The waveguides were made in a column so after one waveguide stopped producing results we could translate the guide vertically to a fresh waveguide. The first round of experiments however completely destroyed the waveguide. There were brown markings visible on glass near the site where the guide was. The laser may have heated and melted the glass if the beam was misaligned into the glass channel. Given this destructive power of the laser, care should be taken in the future for more exact alignment of the laser.

We also had to work at unexpectedly high pressure to produce the estimated electron density. Based on experiments with similarly designed capillaries, such as [79] where a maximum of 150 mbar (2 psi) was used to get electron densities on the order of  $10^{18} \text{cm}^{-3}$  for hydrogen, we expected to need no more than 10 psi to achieve similar electron densities. However we needed to have pressures as high as few hundred psi to get electron signals. Most likely the feeding seal which was an o-ring plastic seal was not pressed hard enough to completely seal and so it is possible that not all of the gas was channelled inside the waveguide. A better design and monitor setup for the gas transport system need to be designed in the future.

## Chapter 6

# PIC Simulations

Particle In Cell (PIC) simulation is an important technique for investigating underlying physical processes in the laser wakefield acceleration. In these simulations the fully relativistic equations of motions coupled to Maxwell's equations are solved for macro particles. Each of these macro (pseudo) particles represent many particles. The number and size of these particles can be set in the simulation parameters.

In most of the PIC simulations, the ions are considered completely stationary to save simulation time. Therefore electron particles moves in a background of positive charge. This is the case with the simulations presented here.

Two sets of simulations were run by the plasma theory group<sup>1</sup> from the Physics Department of the University of Alberta. These fully 3D simulations were carried out using the moving window technique, where instead of simulating the entire length of interaction, a small simulation window ( $\sim 64 \mu\text{m}$  in this case) moves with the laser pulse, in effect discarding areas far away from the laser pulse. The parameters for the simulations are listed in the table 6.1. The 'experiment' column has sample parameters representing typical experimental

---

<sup>1</sup>P.E. Masson-Laborde, N. Naseri, K. Popov, W. Rozmus

	Experiment	Simulation 1	Simulation 2
P(TW)	80	100	100
I(Wcm <sup>-2</sup> )	$6.7 \times 10^{18}$	$7 \times 10^{19}$	$1.7 \times 10^{19}$
$a_0$	1.8	5.8	2.8
$n_e(\text{cm}^{-3})$	$6 \times 10^{18}$	$3 \times 10^{18}$	$1 \times 10^{19}$
nonlinear matched spot size ( $\mu\text{m}$ FWHM)	11	15	10
$S = \frac{n_e}{n_c a_0}$	0.002	0.0003	0.002

Table 6.1: Parameter for simulations

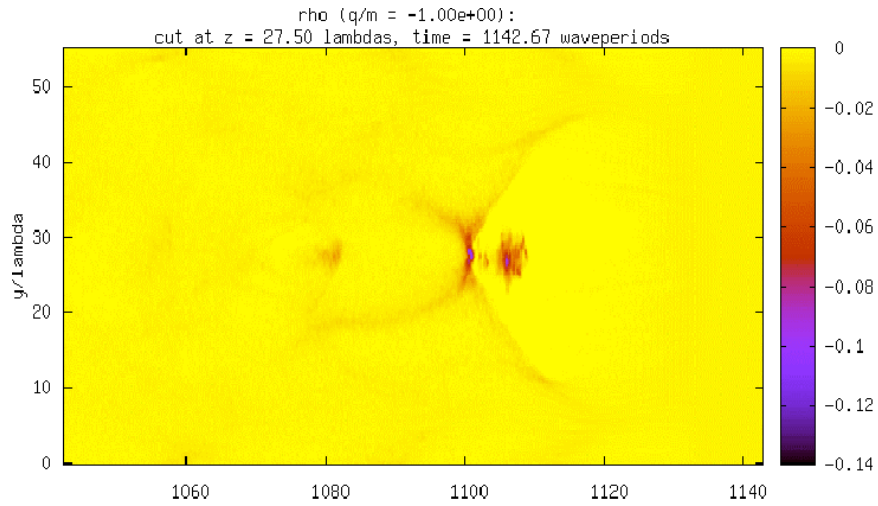
parameters. Parameter S is the similarity parameter defined as [12]

$$S = \frac{n_e}{a_0 n_c} \quad (6.1)$$

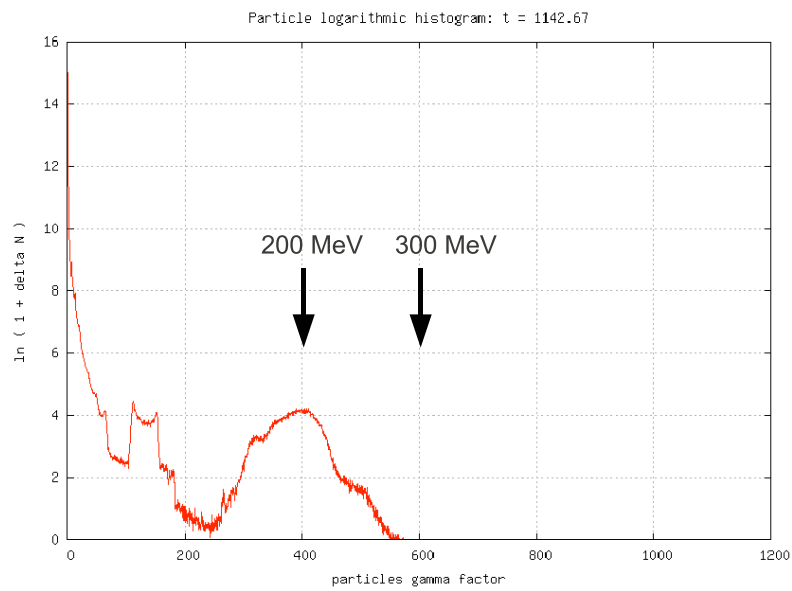
This parameter was developed using ultrarelativistic simulations. According to [12], experiments with the same ‘S’ parameter are similar. The  $a_0$  parameter to be used in this expression is the value during the main interaction after self focusing. Thus significant self focusing of the input beam would lead to simulation parameters 1 while little self focusing would lead to simulation parameters in simulation 2.

Simulation results for the first simulation are shown in Figs. 6.1. It is seen that after 910 microns, there are two trapped bunches clearly defined with 80 MeV and 200 MeV peak energies from two consecutive bubbles. Borders of the bubble can be seen in this image as well. After about 1.7 millimetres, the energies of the two bunches reaches about 300 and 150 MeV. After this point, there is very little acceleration for the high energy bunch while the energy of the second bunch starts to catch up with the first bunch. The result featuring monoenergetic bunches is similar to some of the electron features that we have seen with energies between 100 and 300 MeV (e.g. Fig. 5.7).

The results of the second simulation are shown in Fig. 6.2 and 6.3. The

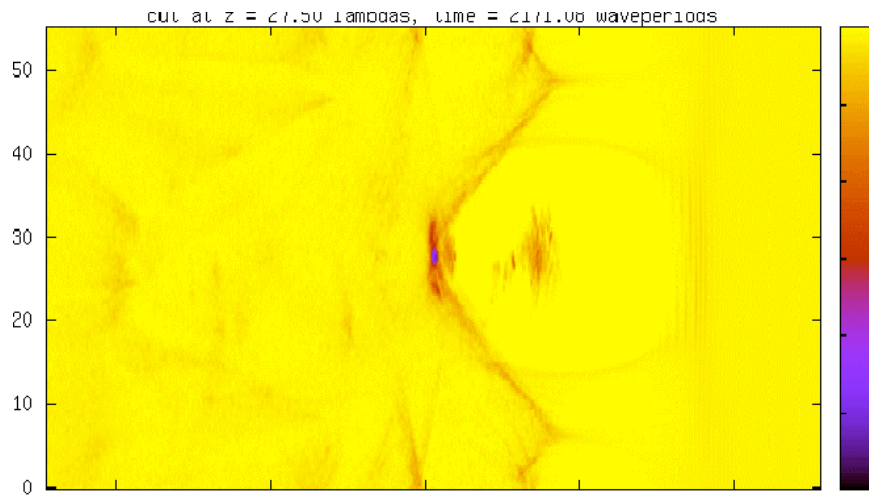


(a) z= 910 microns

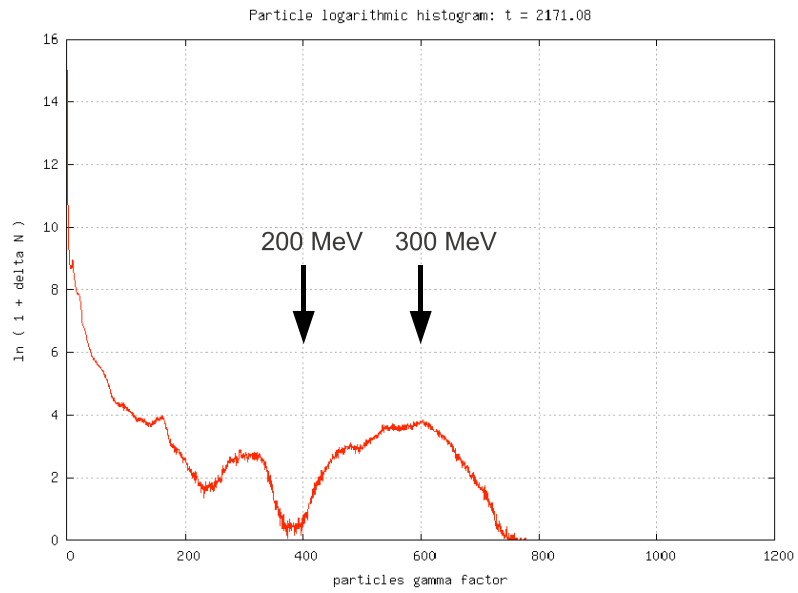


(b) z= 910 microns

Figure 6.1: Results of Simulation 1. The top and bottom figures show snapshots of electron density contour and the electron energy spectra after laser has travelled 910 microns

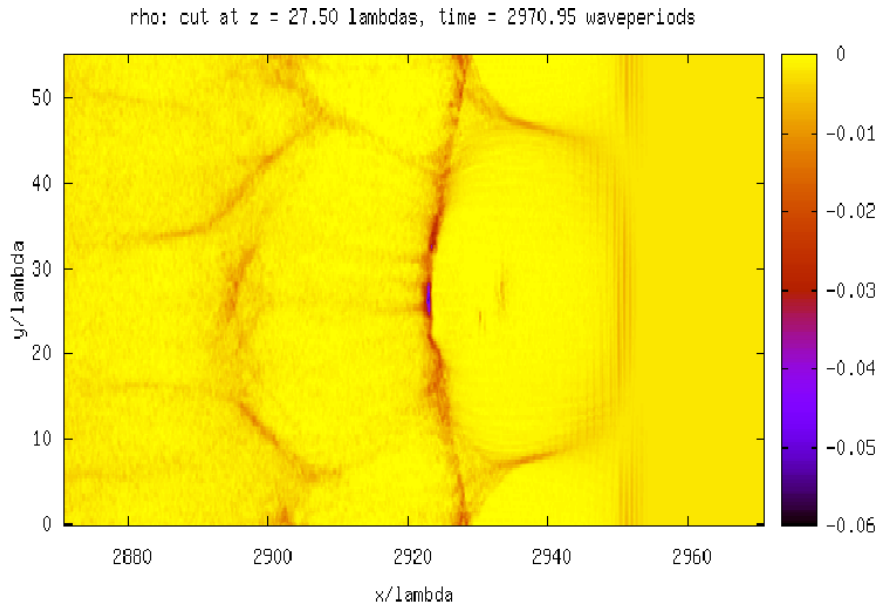


(c) z= 1730 microns

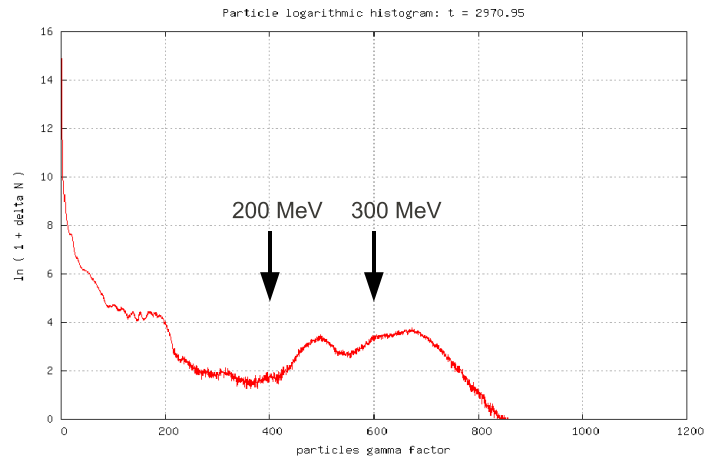


(d) z= 1730 microns

Figure 6.1: Results of Simulation 1 continued. The top and bottom figures show snapshots of electron density contour and the electron energy spectra after laser has travelled 1730 microns



(e) z= 2400 microns



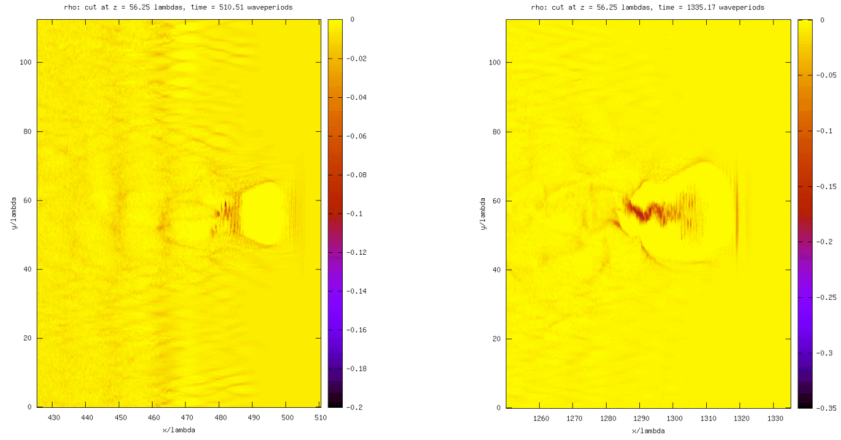
(f) z= 2400 microns

Figure 6.1: Results of Simulation 1 continued. The top and bottom figures show snapshots of electron density contour and the electron energy spectra after laser has travelled 2400 microns

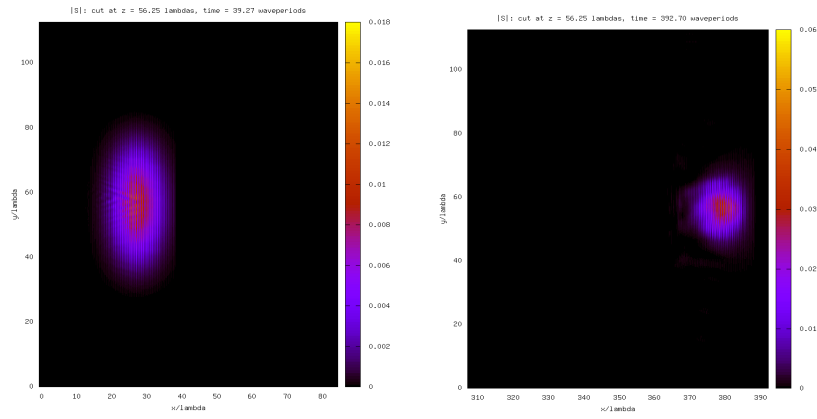
results indicate that the laser pulse undergoes self focusing for the first 300  $\mu\text{m}$  to reach a diameter of 10  $\mu\text{m}$  (equal to nonlinear matched spot size). At this point the wake bubble behind the laser pulse is formed and electron injection begins almost immediately. As shown in Fig. 6.3, the laser pulse's spot size is observed to oscillate and refocus as it propagates in the plasma. This oscillation includes occasions when the laser profile exhibits a ring shape. Meanwhile the bubble radius increases behind the laser pulse. This may be a result of the stronger ponderomotive force caused by the increased intensity of the laser as it undergoes further self focusing. Since the dephasing length is on the order of the plasma bubble [22], electrons that are injected later have a longer acceleration length and can reach higher energies, albeit the bubble's electric field is reduced by all the electrons already in it. The electrons never stop injecting into the bubble until the end of the simulation run. The result is a thermal spectrum with maximum energy of near 500 MeV. Additionally the electrons do not travel on axis. rather, they wiggle inside the bubble as they propagate, generating betatron radiation that was seen during the experiment (see section 5.3.1).

Many aspects of the acceleration observed in the second simulation results have also been observed in the experiments. For example, electron spectra such as Fig. 6.4 indicates continuous injection in the bubble. Different angles observed for different energies also point to the wiggling motion of the electrons as they are accelerated. The ring feature has also been seen in experiments as observed in section 5.3.4. The simulations indicate that the rings appear as a result of self-focusing effects in the bubble as the pulse struggles to keep the matched spot size.

There are also differences between the results of the second simulation and experiments. A significant portion of the electron shots have results that are more consistent with the first simulation. That is the electron spectra has one



(a) Bubble enlargement as the simulation goes on



(b) Pulse evolution from the diameter of 20 microns to a diameter of 10 microns after pulse propagation distance of about 300 microns

Figure 6.2: Results of Simulation 2. Fig. (a) shows the significant growth of the bubble as it propagates about 700 microns from  $x=400$  to  $x=1100$  microns (b) shows the spot size reduction by nearly a factor of two in 300 microns of propagation

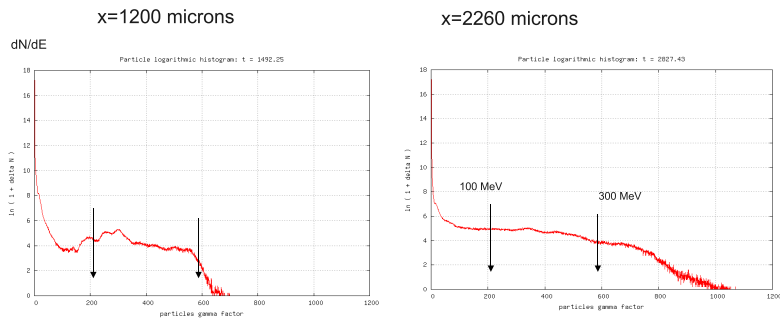
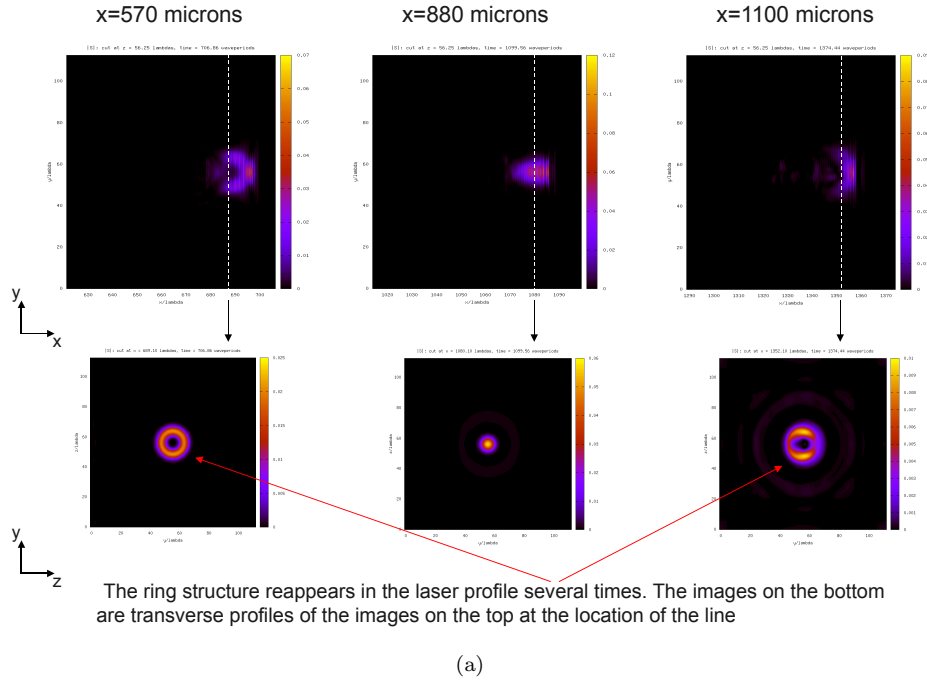


Figure 6.3: Results of Simulation 2: Fig. 6.3a shows reappearance of the ring structure as the pulse keeps evolving and 6.3b shows two samples of electron spectra at two different times.

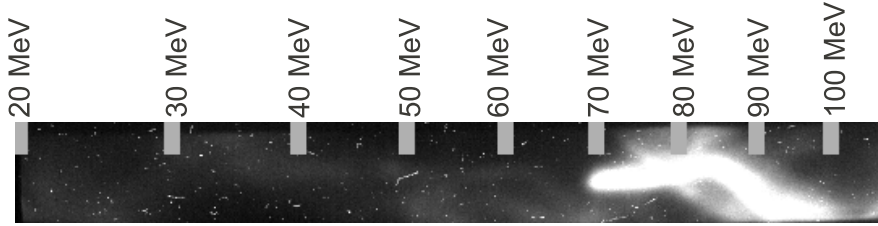


Figure 6.4: An example of electron density spectra which shows evidence of continuous injection. Shot 100310\_110 (side Lanex screen), with estimated electron density  $7 \times 10^{18} \text{cm}^{-3}$

or several electron spots, confined in momentum space (see Fig. 5.7). It is expected that this may be due to self focusing effects for the input beam. In these shots, the electron injection must have followed a pattern similar to the simulation one. In other words, injection stopped and a monoenergetic bunch was accelerated by the bubble to hundreds of MeVs of energy.

Overall, the simulations demonstrate many common features with the experimental results. However, variation of laser and density profile from shot to shot and also non-uniformity of these same parameters, may account for the differences in features observed from shot to shot.

## Chapter 7

# Conclusions

In conclusion, we have investigated the effect of different parameters on laser wakefield acceleration, trying to increase the energy of monoenergetic beams observed as well as understand the underlying processes.

In the weakly relativistic regime, we have performed experiments using the 10 TW ALLS system to obtain monoenergetic electron beams using a short, 15 cm and a long, 30 cm focal length parabola. Typically, we were able to obtain quasi-monoenergetic electron bunches of 10-50 MeV energy from nitrogen at electron density of  $10^{20}\text{cm}^{-3}$ , and 10-30 MeV from He at electron density of  $5 \times 10^{19}\text{cm}^{-3}$  with the 15 cm focal length parabola as previously reported [57]. We also obtained occasional shots of over 100 MeV from nitrogen and helium with the 15 cm parabola. These occasional shots probably represent the ideal set of guiding and injection plasma conditions obtained with just the right level of prepulse. Experiments done with varying levels of prepulse confirm the existence of small plasma channels that may be used by the laser pulse for guiding. With the 30 cm focal length parabola, we typically obtained quasi-Maxwellian electron energy distributions from nitrogen at electron density of

$10^{20}\text{cm}^{-3}$ . We occasionally also saw weak quasi-monoenergetic electron bunches with energies of the order of 5 MeV from the 30 cm parabola. The dependence of our results on high amount of prepulse suggests that the preplasma seeded by the fs prepulse and heated by the nanosecond ASE pedestal plays a significant role in the interaction. Also as wave breaking is easier at higher densities this indicates that the lack of results at lower density may be a result of having difficulty with injection. Finally, the experiments show that the nonlinear self-focusing of the laser does not compensate for the lowered intensity of the input beam when using the long focal length parabola under our conditions.

In the 3D nonlinear regime, experiments were carried out at the 100 TW ALLS beamline. At high densities ( $\sim 5 \times 10^{19}\text{cm}^{-2}$ ) obtained using the 2.4 mm gas jet target, electron energies of about 80 MeV were observed which is significantly less than the theoretical maximum energy possible. A number of factors including high amounts of scattered laser light and short acceleration limiting lengths at these densities could be the explanation for the low energies. With electron density between  $5 \times 10^{18}$  and  $1 \times 10^{19}\text{cm}^{-3}$  quasi-monoenergetic spots with energies between 100 to 300 MeV were routinely observed using a 5 mm helium gas jet as the target. Occasionally, bunches appeared at very high energies, and further research is required to determine their nature or manner of generation. It was determined from the results that the mean energy observed with decreasing electron density did not increase as predicted by theory. Thus the effect of decreasing electron density leading to an increase in acceleration length, i.e. the dephasing and depletion length, is cancelled either by the lowered accelerating electric field or the longer length of pulse evolution required for wave-breaking injection. On the other hand the increase in matched bubble spot size accompanying the decrease in density did seem to have a positive effect on the percentage of shots yielding monoenergetic results. Furthermore

it was determined that the energy of electrons is dependent on the position of vacuum laser focus. There appears to be an ideal range of vacuum focus located a few millimetres inside the boundary of the gas jet target which resulted both in the highest mean energy of monoenergetic spots as well the highest percentage of electron signals yielding monoenergetic spots. Focusing in this region seems to have a stabilizing effect on the relativistic self-focusing leading to the highest percentage of monoenergetic shots with high energies.

Nitrogen was also used as a target both as a small percentage impurity in helium and as a stand alone target. Small amounts of nitrogen in helium were used to investigate ionization injection where trapped electrons are generated by the 6th nitrogen ionization state. High energy electron signals were observed for the first time in published literature with nitrogen as target; both as an impurity addition to helium and as an stand alone gas. Additionally, it was found that the energies obtained from pure nitrogen were lower than those observed from  $N_2$ :He mix and additionally a large percentage of the shots yielded quasi-Maxwellian spectrum.

Laser guiding experiments showed how at full operation of our laser, a large degree of filamentation occurs due to a large amount of disparity between the matched spot size and the input laser spot size. It was demonstrated that contrary to other publications, when the power rises too high compared to the critical power for self focusing, a matched spot size is no longer maintained, and multiple filaments are observed instead. Rectifying this issue in future experiments could lead to higher energy electron beams with the same setup as the entire laser energy can be focused into a single accelerating bubble by choosing the appropriate vacuum spot size.

Also for the first time, ring structures were observed in the laser profile at the end of the interaction, with corresponding electron spots being observed on

the Lanex screen before the magnets. This phenomenon may be related to the process of self-focusing of laser in the plasma and requires further investigation.

Trends observed in 5 mm gas jet were also observed in the 10 mm exit diameter gas jet, most notably, it was shown for the first time that the depth of focus is an important factor in percentage of shots that yield quasi-monoenergetic spectrum. Also a lower electron density boundary of  $2 \times 10^{18} \text{cm}^{-3}$  was found for our configuration below which no electrons were observed.

10 mm passive capillary waveguides were tried and a few shots yielding quasi-monoenergetic electrons the range of 100-200 MeV were observed. The glass waveguide was found to be have been damaged after the experiment, which could indicate incorrect alignment on some shots. A better system for alignment of guides and gas delivery will make if possible to do a systematic study of the waveguides in the future.

Finally PIC simulations done by the plasma group on pulse propagation and electron acceleration demonstrate many common features of electron spots observed during the experiments, including multiple monoenergetic spots, monoenergetic vs. quasi-Maxwellian spectrum development, and the ring structure observed in the laser profile.

# Bibliography

- [1] T. Tajima and J. Dawson, “Laser Electron Accelerator,” *Physical Review Letters*, vol. 43, pp. 267–270, July 1979.
- [2] D. STRICKLAND and G. MOUROU, “Compression of amplified chirped optical pulses,” *Optics Communications*, vol. 56, pp. 219–221, Dec. 1985.
- [3] S. P. D. Mangles, C. D. Murphy, Z. Najmudin, A. G. R. Thomas, J. L. Collier, A. E. Dangor, E. J. Divall, P. S. Foster, J. G. Gallacher, C. J. Hooker, D. A. Jaroszynski, A. J. Langley, W. B. Mori, P. A. Norreys, F. S. Tsung, R. Viskup, B. R. Walton, and K. Krushelnick, “Monoenergetic beams of relativistic electrons from intense laser-plasma interactions,” *Nature*, vol. 431, pp. 535–538, 2004.
- [4] J. Faure, Y. Glineac, A. M. Pukhov, S. Kiselev, S. Gordieno, E. Lefebvre, J. P. Rousseau, F. Burgy, and V. Malka, “A laser-plasma accelerator producing monoenergetic electron beams,” *Nature*, vol. 431, pp. 541–544, 2004.
- [5] C. G. R. Geddes, C. Toth, J. V. Tilborg, E. Esarey, C. B. Schroeder, D. Bruhwiler, C. Nieter, J. Cary, and W. P. Leemans, “High-quality electron beams from a laser wakefield accelerator using plasma-channel guiding,” *Nature*, vol. 431, p. 538, 2004.

- [6] W. P. Leemans, B. Nagler, A. J. Gonsalves, C. Toth, K. Nakamura, C. G. R. Geddes, E. Esarey, C. B. Schroeder, and S. M. Hooker, “GeV electron beams from a centimetre-scale accelerator,” *Nature Physics*, vol. 2, pp. 696–699, 2006.
- [7] E. Esarey, P. Sprangle, J. Krall, and A. Ting, “Overview of plasma-based accelerator concepts,” *IEEE Transactions on Plasma Science*, vol. 24, no. 2, pp. 252–288, 1996.
- [8] N. Hafz, M. Uesaka, J. Koga, and K. Nakajima, “Numerical analysis of 10 fs femtosecond relativistic electron beam generation using single 12 TW50 fs laser pulse,” *Nuclear Instruments and Methods in Physics Research A*, vol. 455, pp. 148–154, 2000.
- [9] H. P. Schlenvoigt, K. Haupt, A. Debus, F. Budde, O. Jackel, S. Pfotenhauer, H. Schwoerer, E. Rohwer, J. G. Gallacher, E. Brunetti, R. P. Shanks, S. M. Wiggins, and D. A. Jaroszynski, “A compact synchrotron radiation source driven by a laser-plasma wakefield accelerator,” *Nature Physics*, vol. 4, no. February, pp. 130–133, 2008.
- [10] E. Esarey, C. B. Schroeder, and W. P. Leemans, “Physics of laser-driven plasma-based electron accelerators,” *Reviews of Modern Physics*, vol. 81, no. September, p. 1229, 2009.
- [11] S. Kneip, S. R. Nagel, S. F. Martins, S. P. D. Mangles, C. Bellei, O. Chekhlov, R. J. Clarke, N. Delerue, E. J. Divall, G. Doucas, K. Ertel, F. Fiuza, R. Fonseca, P. Foster, S. J. Hawkes, C. J. Hooker, K. Krushelnick, W. B. Mori, C. A. J. Palmer, K. T. Phuoc, P. P. Rajeev, J. Schreiber, M. J. V. Streeter, D. Urner, J. Vieira, L. O. Silva, and Z. Najmudin, “Near-GeV Acceleration of Electrons by a Nonlinear Plasma Wave Driven by a

- Self-Guided Laser Pulse,” *Physical Review Letters*, vol. 103, p. 035002, 2009.
- [12] S. Gordienko and A. Pukhov, “Scalings for ultrarelativistic laser plasmas and quasimonoenergetic electrons,” *Physics of Plasmas*, vol. 12, no. 4, p. 043109, 2005.
- [13] J. E. Ralph, K. A. Marsh, A. E. Pak, W. Lu, C. E. Clayton, F. Fang, W. B. Mori, and C. Joshi, “Self-Guiding of Ultrashort , Relativistically Intense Laser Pulses through Underdense Plasmas in the Blowout Regime,” *Physical Review Letters*, vol. 102, no. May, p. 175003, 2009.
- [14] P. Sprangle, E. Esarey, J. Krall, and G. Joyce, “Propagation and guiding of intense laser pulses in plasmas,” *Physical Review Letters*, vol. 69, no. 15, p. 2200, 1992.
- [15] P. Sprangle, E. Esarey, and A. Ting, “Nonlinear theory of intense laser-plasma interactions,” *Physical Review Letters*, vol. 64, pp. 2011–2014, Apr. 1990.
- [16] P. Sprangle, C. M. Tang, and E. Esarey, “Relativistic self-focusing of short-pulse radiation beams in plasmas,” *IEEE Transactions on Plasma Science*, vol. ps-15, no. 2, pp. 145–153, 1987.
- [17] P. Sprangle, E. Esarey, and A. Ting, “Nonlinear interaction of intense laser pulses in plasmas,” *Physical Review A*, vol. 41, pp. 4463–4469, Apr. 1990.
- [18] G. Z. Sun, E. Ott, Y. C. Lee, and P. Guzdar, “Self-focusing of short intense pulses in plasmas,” *Physics of Fluids*, vol. 30, no. 2, p. 526, 1987.
- [19] P. Sprangle, A. Zigler, and E. Esarey, “Elimination of laser prepulse by relativistic guiding in a plasma,” *Applied Physics Letters*, vol. 58, no. 4, p. 346, 1991.

- [20] A. G. R. Thomas, Z. Najmudin, S. P. D. Mangles, C. D. Murphy, A. E. Dangor, C. Kamperidis, K. L. Lancaster, W. B. Mori, P. A. Norreys, W. Rozmus, and K. Krushelnick, “Effect of laser-focusing conditions on propagation and monoenergetic electron production in laser-wakefield accelerators,” *Physical Review Letters*, vol. 98, p. 095004, 2007.
- [21] D. H. Froula, C. E. Clayton, T. Doppner, K. A. Marsh, C. P. J. Barty, L. Divol, R. A. Fonseca, S. H. Glenzer, C. Joshi, W. Lu, S. F. Martins, P. Michel, W. B. Mori, J. P. Palastro, B. B. Pollock, A. Pak, J. E. Ralph, J. S. Ross, C. W. Siders, L. O. Silva, and T. Wang, “Measurements of the Critical Power for Self-Injection of Electrons in a Laser Wakefield Accelerator,” *Physical Review Letters*, vol. 103, p. 215006, 2009.
- [22] W. Lu, M. Tzoufras, C. Joshi, F. S. Tsung, W. B. Mori, J. M. Vieira, R. A. Fonseca, and L. O. Silva, “Generating multi-GeV electron bunches using single stage laser wakefield acceleration in a 3D nonlinear regime,” *Physical Review Special Topics- Accelerators and Beams*, vol. 10, p. 061301, 2007.
- [23] S. P. D. Mangles, A. G. R. Thomas, O. Lundh, F. Lindau, M. C. Kaluza, A. Persson, C. Wahlström, K. Krushelnick, and Z. Najmudin, “On the stability of laser wakefield electron accelerators in the monoenergetic regime,” *Physics of Plasmas*, vol. 14, no. 056702, p. 056702, 2007.
- [24] C. McGuffey, A. G. R. Thomas, W. Schumaker, T. Matsuoka, V. Chvykov, F. J. Dollar, G. Kalintchenko, V. Yanovsky, A. Maksimchuk, K. Krushelnick, V. Y. Bychenkov, I. V. Glazyrin, and A. V. Karapeev, “Ionization Induced Trapping in a Laser Wakefield Accelerator,” *Physical Review Letters*, vol. 104, p. 025004, 2010.
- [25] S. P. D. Mangles, A. G. R. Thomas, C. Bellei, A. E. Dangor, C. Kamperidis, S. Kneip, S. R. Nagel, L. Willingale, and Z. Najmudin, “Self-Guided

- Wakefield Experiments Driven by Petawatt-Class Ultrashort Laser Pulses,” *IEEE Transactions on Plasma Science*, vol. 36, no. 4, pp. 1715–1721, 2008.
- [26] F. Tsung, R. Narang, W. Mori, C. Joshi, R. Fonseca, and L. Silva, “Near-GeV-Energy Laser-Wakefield Acceleration of Self-Injected Electrons in a Centimeter-Scale Plasma Channel,” *Physical Review Letters*, vol. 93, Oct. 2004.
- [27] I. Kostyukov, E. Nerush, A. Pukhov, and V. Seredov, “Electron Self-Injection in Multidimensional Relativistic-Plasma Wake Fields,” *Physical Review Letters*, vol. 103, no. October, p. 175003, 2009.
- [28] E. Oz, S. Deng, T. Katsouleas, P. Muggli, C. D. Barnes, I. Blumenfeld, F. J. Decker, P. Emma, M. J. Hogan, R. Ischebeck, R. H. Iverson, N. Kirby, P. Krejcik, C. O. Connell, R. H. Siemann, D. Walz, D. Auerbach, C. E. Clayton, C. Huang, D. K. Johnson, C. Joshi, W. Lu, K. A. Marsh, W. B. Mori, and M. Zhou, “Ionization-Induced Electron Trapping in Ultrarelativistic Plasma Wakes,” *Physical Review Letters*, vol. 98, no. February, p. 084801, 2007.
- [29] N. Kirby, I. Blumenfeld, C. E. Clayton, F. J. Decker, M. J. Hogan, C. Huang, R. Ischebeck, R. H. Iverson, C. Joshi, T. Katsouleas, W. Lu, K. A. Marsh, S. F. Martins, W. B. Mori, P. Muggli, E. Oz, R. H. Siemann, D. Walz, and M. Zhou, “Transverse emittance and current of multi-GeV trapped electrons in a plasma wakefield accelerator,” *Physical Review Special Topics- Accelerators and Beams*, vol. 12, p. 051302, 2009.
- [30] T. P. Rowlands-rees, C. Kamperidis, S. Kneip, A. J. Gonsalves, S. P. D. Mangles, J. G. Gallacher, E. Brunetti, T. Ibbotson, C. D. Murphy, P. S. Foster, M. J. V. Streeter, F. Budde, P. A. Norreys, D. A. Jaroszynski,

- K. Krushelnick, Z. Najmudin, and S. M. Hooker, “Laser-Driven Acceleration of Electrons in a Partially Ionized Plasma Channel,” *Physical Review Letters*, vol. 100, no. March, p. 105005, 2008.
- [31] A. Pak, K. A. Marsh, S. F. Martins, W. Lu, W. B. Mori, and C. Joshi, “Injection and Trapping of Tunnel-Ionized Electrons into Laser-Produced Wakes,” *Physical Review Letters*, vol. 104, no. JANUARY, p. 025003, 2010.
- [32] T. Hosokai, K. Kinoshita, A. Zhidkov, K. Nakamura, T. Watanabe, T. Ueda, H. Kotaki, M. Kando, K. Nakajima, and M. Uesaka, “Effect of a laser prepulse on a narrow-cone ejection of MeV electrons from a gas jet irradiated by an ultrashort laser pulse,” *Physical Review E*, vol. 67, p. 036407, Mar. 2003.
- [33] T. Ohkubo, A. Zhidkov, T. Hosokai, K. Kinoshita, and M. Uesaka, “Effects of density gradient on short-bunch injection by wave breaking in the laser wake field acceleration,” *Physics of Plasmas*, vol. 13, p. 033110, 2006.
- [34] C. G. R. Geddes, K. Nakamura, G. R. Plateau, C. Toth, E. Cormier-michel, E. Esarey, C. B. Schroeder, J. R. Cary, and W. P. Leemans, “Plasma-Density-Gradient Injection of Low Absolute-Momentum-Spread Electron Bunches,” *Physical Review Letters*, vol. 100, no. May, p. 215004, 2008.
- [35] A. Yamazaki, H. Kotaki, I. Daito, M. Kando, S. V. Bulanov, T. Z. Esirkepov, S. Kondo, S. Kanazawa, T. Homma, K. Nakajima, Y. Oishi, T. Nayuki, T. Fuji, and K. Nemoto, “Quasi-monoenergetic electron beam generation during laser pulse interaction with very low density plasmas,” *Physics of Plasmas*, vol. 12, p. 093101, 2005.
- [36] J. Faure, C. Rechatin, A. Norlin, A. Lifschitz, Y. Glinec, and V. Malka, “Controlled injection and acceleration of electrons in plasma wakefields by colliding laser pulses,” *Nature*, vol. 444, pp. 737–739, 2006.

- [37] G. Fubiani, E. Esarey, C. B. Schroeder, and W. P. Leemans, “Beat wave injection of electrons into plasma waves using two interfering laser pulses,” *Physical Review E*, vol. 70, p. 016402, 2004.
- [38] H. Kotaki, S. Masuda, M. Kando, J. K. Koga, and K. Nakajima, “Head-on injection of a high quality electron beam by the interaction of two laser pulses,” *Physics of Plasmas*, vol. 11, no. 6, pp. 3296–3302, 2004.
- [39] C. Rechatin, J. Faure, A. Lifschitz, X. Davoine, E. Lefebvre, and V. Malka, “Quasi-monoenergetic electron beams produced by colliding cross-polarized laser pulses in underdense plasmas,” *New Journal of Physics*, vol. 11, no. 013011, p. 13011, 2009.
- [40] X. Davoine, E. Lefebvre, C. Rechatin, J. Faure, and V. Malka, “Cold Optical Injection Producing Monoenergetic, Multi-GeV Electron Bunches,” *Physical Review Letters*, vol. 102, no. 6, p. 65001, 2009.
- [41] H. Kotaki, I. Daito, M. Kando, Y. Hayashi, K. Kawase, T. Kameshima, Y. Fukuda, T. Homma, J. Ma, L. M. Chen, T. Z. Esirkepov, A. S. Pirozhkov, J. K. Koga, A. Faenov, T. Pikuz, H. Kiriya, H. Okada, T. Shimomura, Y. Nakai, M. Tanoue, H. Sasao, D. Wakai, H. Matsuura, S. Kondo, S. Kanazawa, A. Sugiyama, H. Daido, and S. V. Bulanov, “Electron Optical Injection with Head-On and Countercrossing Colliding Laser Pulses,” *Physical Review Letters*, vol. 103, no. November, p. 194803, 2009.
- [42] H. Kotaki, I. Daito, Y. Hayashi, J. Ma, L. M. Chen, M. Kando, T. Z. Esirkepov, Y. Fukuda, T. Homma, A. Pirozhkov, J. K. Koga, K. Nakajima, H. Daido, and S. V. Bulanov, “Counter-crossing injection for stable high-quality electron beam generation via laser-plasma interaction,” in *Journal of Physics: Conference Series*, vol. 112, p. 42031, Institute of Physics Publishing, Institute of Physics Publishing, 2008.

- [43] H. Kotaki, I. Daito, M. Kando, Y. Hayashi, J. Ma, L.-m. Chen, T. Z. Esirkepov, Y. Fukuda, T. Homma, A. Pirozhkov, J. K. Koga, K. Nakajima, H. Daido, and S. V. Bulanov, “Improvement of the Quality and Stability of Electron Bunch Using Countercrossing Laser Beam,” *IEEE Transactions on Plasma Science*, vol. 36, no. 4, pp. 1760–1764, 2008.
- [44] B. A. Shadwick, C. B. Schroeder, and E. Esarey, “Nonlinear laser energy depletion in laser-plasma accelerators,” *Physics of Plasmas*, vol. 16, no. 5, p. 056704, 2009.
- [45] E. Miura, K. Koyama, S. Kato, and N. Saito, “Demonstration of quasi-monoenergetic electron-beam generation in laser-driven plasma acceleration,” *Applied Physics Letters*, vol. 86, p. 251501, 2005.
- [46] K. Nakamura, B. Nagler, C. Toth, C. G. R. Geddes, C. B. Schroeder, E. Esarey, W. P. Leemans, A. J. Gonsalves, and S. M. Hooker, “GeV electron beams from a centimeter-scale channel guided laser wakefield accelerator,” *Physics of Plasmas*, vol. 14, p. 056708, 2007.
- [47] W. P. Leemans, C. W. Siders, E. Esarey, N. E. Andreev, G. Shvets, and W. B. Mori, “Plasma Guiding and Wakefield Generation for Second-Generation Experiments,” *IEEE Transactions on Plasma Science*, vol. 24, no. 2, pp. 331–342, 1996.
- [48] K. Bockasten, “Transformation of Observed Radiances into Radial Distribution of the Emission of a Plasma,” *Journal of the Optical Society of America*, vol. 51, p. 943, Sept. 1961.
- [49] F. F. Chen, *Introduction to Plasma Physics and Controlled Fusion*. Springer, 1984.

- [50] E. R. Peck and B. N. Khanna, “Dispersion of Nitrogen,” *Journal of the Optical Society of America*, vol. 56, no. August, p. 1059, 1966.
- [51] C. R. Mansfield and E. R. Peck, “Dispersion of Helium,” *Journal of the Optical Society of America*, vol. 59, p. 199, Feb. 1969.
- [52] J. Hilsenrath, C. W. Beckett, W. S. Benedict, L. Fano, H. I. Hoge, J. F. Masi, R. L. Nuttall, Y. Touloukian, and H. W. Woolley, *Tables of thermal properties of gases*. U.S. National Bureau of Standards Circular No. 564, 1955.
- [53] D. White, T. Rubin, P. Camky, and H. L. Johnston, “THE VIRIAL COEFFICIENTS OF HELIUM FROM 20 TO 300K.,” *Journal of Physical Chemistry*, vol. 64, pp. 1607–1612, Nov. 1960.
- [54] A. D. Buckingham and C. Graham, “The Density Dependence of the Refractivity of Gases,” *Proceedings of the Royal Society of London. Series A, Mathematical and Physical Sciences*, vol. 337, no. 1609, pp. 275 – 291, 1974.
- [55] H. DEWIJN and F. HEINEKEN, “The lorentz-lorenz functions of argon, nitrogen and carbon dioxide up to 50 atmospheres at a wavelength of 12 mm,” *Physica*, vol. 25, no. 1-6, pp. 615–625, 1959.
- [56] M. E. Thomas and T. J. Tayag, “Refractive index of He, SF<sub>6</sub>, and CO<sub>2</sub> at 0.63299 um as a function of temprature and pressure,” *Applied Optics*, vol. 27, no. 16, pp. 3317–3318, 1988.
- [57] Z. Chen, C. Unick, N. Vafaei-Najafabadi, Y. Tsui, R. Fedosejevs, N. Naseri, P.-E. Masson-Laborde, and W. Rozmus, “Quasi-monoenergetic electron beams generated from 7 TW laser pulses in N<sub>2</sub> and He gas targets,” *Laser and Particle Beams*, vol. 26, pp. 147–155, June 2008.

- [58] T. Hosokai, K. Kinoshita, T. Ohkubo, A. Maekawa, M. Uesaka, A. Zhidkov, A. Yamazaki, H. Kotaki, M. Kando, K. Nakajima, S. V. Bulanov, P. Tomassini, A. Giulietti, and D. Giulietti, “Observation of strong correlation between quasimonoenergetic electron beam generation by laser wakefield and laser guiding inside a preplasma cavity,” *Physical Review E*, vol. 73, p. 036407, 2006.
- [59] B. A. Lengyel, *introduction to laser optics*. John Wiley and Sons, 1966.
- [60] S. Semushin and V. Malka, “High density gas jet nozzle design for laser target production,” *Review of Scientific Instruments*, vol. 72, no. 7, p. 2961, 2001.
- [61] Y. Glinec, J. Faure, A. Guemnie-Tafo, V. Malka, H. Monard, J. P. Larbre, V. De Waele, J. L. Marignier, and M. Mostafavi, “Absolute calibration for a broad range single shot electron spectrometer,” *Review of Scientific Instruments*, vol. 77, p. 103301, 2006.
- [62] S. Fourmaux, S. Payeur, A. Alexandrov, C. Serbanescu, F. Martin, T. Ozaki, A. Kudryashov, and J. C. Kieffer, “Laser beam wavefront correction for ultra high intensities with the 200 TW laser system at the advanced laser light source,” *Optics Express*, vol. 16, p. 11987, July 2008.
- [63] L. D. Landau and E. M. Lifshitz, *Fluid Mechanics*. Pergamon Press, 1959.
- [64] S. Schreier, *Compressible flow*. John Wiley and Sons, 1982.
- [65] D. J. Spence and S. M. Hooker, “Investigation of a hydrogen plasma waveguide,” *Physical Review E*, vol. 63, p. 015401, 2000.
- [66] T. Kameshima, H. Kotaki, M. Kando, I. Daito, K. Kawase, Y. Fukuda, L. M. Chen, T. Homma, S. Kondo, T. Z. Esirkepov, N. A. Bobrova, P. V. Satorov, and S. V. Bulanov, “Laser pulse guiding and electron acceleration

- in the ablative capillary discharge plasma,” *Physics of Plasmas*, vol. 16, no. 9, p. 093101, 2009.
- [67] K. Nakamura, W. Wan, N. Ybarrolaza, D. Syversrud, J. Wallig, and W. P. Leemans, “Broadband single-shot electron spectrometer for GeV-class laser-plasma-based accelerators,” *Review of Scientific Instruments*, vol. 79, p. 053301, 2008.
- [68] R. Benattar, C. Popovics, and R. Sigel, “Polarized light interferometer for laser fusion studies,” *The Review of scientific instruments*, vol. 50, p. 1583, Dec. 1979.
- [69] N. Vafaei-Najafabadi, A. Ali, J. A. Chakera, R. Fedosejevs, and Y. Y. Tsui, “Parametric investigation of laser wakefield acceleration versus F-number of focusing optics,” in *Photonics North 2009* (R. Vallee, ed.), vol. 7386, (Quebec, Canada), pp. 738638–8, SPIE, June 2009.
- [70] G. Bekefi, *principles of laser plasmas*. John Wiley and Sons, 1977.
- [71] A. Pukhov, Z.-M. Sheng, and J. Meyer-ter Vehn, “Particle acceleration in relativistic laser channels,” *Physics of Plasmas*, vol. 6, no. 7, p. 2847, 1999.
- [72] C. Gahn, G. D. Tsakiris, A. Pukhov, J. Meyer-ter Vehn, G. Pretzler, P. Thirolf, D. Habs, and K. J. Witte, “Multi-MeV Electron Beam Generation by Direct Laser Acceleration in High-Density Plasma Channels,” *Physical Review Letters*, vol. 83, no. 23, p. 4772, 1999.
- [73] M. Tanimoto, S. Kato, E. Miura, N. Saito, K. Koyama, and J. K. Koga, “Direct electron acceleration by stochastic laser fields in the presence of self-generated magnetic fields,” *Physical Review E*, vol. 68, p. 026401, 2003.

- [74] E. Esarey, B. Shadwick, P. Catravas, and W. Leemans, “Synchrotron radiation from electron beams in plasma-focusing channels,” *Physical Review E*, vol. 65, May 2002.
- [75] E. Esarey and W. P. Leemans, “Femtosecond Electron and X-Ray Generation By Laser and Plasma-Based Sources,” *Femtosecond electron and X-ray generation by laser and plasma-based sources*, pp. 146–163, 2000.
- [76] V. L. Highland, “Some practical remarks on multiple scattering,” *Nuclear Instruments and Methods*, vol. 129, pp. 497–499, 1975.
- [77] S. Karsch, J. Osterhoff, A. Popp, T. P. Rowlands-rees, Z. Major, M. Fuchs, B. Marx, R. Hörlein, K. Schmid, L. Veisz, S. Becker, U. Schramm, B. Hidding, G. Pretzler, D. Habs, F. Grüner, F. Krausz, and S. M. Hooker, “GeV-scale electron acceleration in a gas-filled capillary discharge waveguide,” *New Journal of Physics*, vol. 9, pp. 1–11, 2007.
- [78] R. Fedosejevs, X. Wang, and G. Tsakiris, “Onset of relativistic self-focusing in high density gas jet targets,” *Physical Review E*, vol. 56, pp. 4615–4639, Oct. 1997.
- [79] A. J. Gonsalves, T. P. Rowlands-rees, B. H. P. Broks, J. J. A. M. Van Der Mullen, and S. M. Hooker, “Transverse Interferometry of a Hydrogen-Filled Capillary Discharge Waveguide,” *Physical Review Letters*, vol. 98, p. 025002, 2007.

## Appendix A

# Waveguide Fabrication

## Process

The capillaries were composed of two glass pieces, one being the cap piece having a feeding hole to transport the gas in to the capillary and the other being the capillary piece having the cell design etched in it. Three different width of the capillaries were designed for processing: 100, 200 and 400 microns. The gas flowed from the location of entry to the two edges of the waveguide as shown in [Fig. 3.6a](#).

The capillaries were made by a process similar to producing a microfluidic channel. The process was carried out in the clean room of nanofabrication facility of the Electrical and Computer Engineering Department of the University of Alberta. Four inch borofloat glasses were used for fabrication using the following process. The process outlined below is shown schematically in [Fig. A.1](#)

1. The substrates were initially cleaned with a 3:1 mixture of sulfuric acid and hydrogen peroxide (called Piranha) which cleans all organic matters on the glass surfaces.

2. The substrates were then sputtered with 30 nm of chromium and 170 nm of gold layer. This was done with a DC sputtering machine(nicknamed Bob).
3. The substrates were then coated with photoresist using a spinner. The photoresist is the chemical HPR504 and the wafers spin after it is poured on them at 500 RPM for 10s in order to get a uniform layer and at 4000 RPM for 40s for it to become thin and uniform. The substrates are then baked at 115 °C for 30 minutes are left to cool for 15. At this stage the substrate is ready for pattern transformation.
4. Pattern of the cell design are transformed to the substrate by exposing them to UV light. A mask with the pattern of waveguides on it is put in contact with the 4" substrate and then it is exposed to UV light which changes the chemical bonding for exposed areas. The exact exposure time differs depending on the machine and the strength of the particular UV bulb and a nanofab technician should be consulted for the exact time. For my substrates the appropriate time was 3.2 s with the machine nicknamed Oscar.
5. Once the pattern was imprinted, the substrates were submerged in the developer liquid (HPR354) while the container was agitated for about 20 s. The developer dissolved the photoresist not exposed to the UV light, while leaving the exposed photoresist alone.
6. At this stage, the glass is exposed by removing gold and chromium using acids that are almost ineffective on the photoresist. Chromium is completely removed in about 15 s while gold needs about a minute. For both metals, the substrates need to be submerged and agitated in the etchant. The substrates should be observed under the microscope in order to ensure

the satisfactory removal of the metals before glass etching.

7. HF is used at this stage to remove the glass where it is exposed. Unfortunately at the time of this work, dry etching technology for glass substrates were not available at the nanofab. Since wet etch with HF is an isotropic etch, by the time the capillaries were etched to the desired depth, they were as wide as they were deep (see Fig. A.2 where the rising edge profile for 100  $\mu\text{m}$  deep etched glass channel is shown). Two substrates were etched either 100 or 200 microns deep. The average etch rate of about 2  $\mu\text{m}/\text{min}$  is variable depending on the temperature and agitation level of the HF and so the etch rate needs to be checked once at the beginning of each etch to determine the rate. In my experience, the etch rate varied between 1.6 and 2  $\mu\text{m}/\text{min}$ .
8. After the wet etching process, The UV exposed photoresist is removed by acetone, and the remaining metal which has remained on the substrate up to this stage were removed. At this stage, this substrate piece is ready to be bonded to the cap piece.

The cap piece which is also a four inch borofloat substrate includes 1 mm diameter holes which are drilled into it at the machine shop using a water jet drill. The software for water drilling at the machine shop accepts files with .dxf extension, but it is incompatible with modern implementations of the said extension. Therefore, it was more practical to directly draw the coordinates of the matching holes into the software at the machine shop and this is exactly what I did. A protective layer of sacrificial glass are required to be attached to borofloats before drilling in order to prevent damage to them. The sacrificial glass pieces are attached to the borofloat glass using a sticky paste called Crystalbond 590 which becomes viscous at about 150 ° C. The crystal bond is dissolved in methanol after the holes are drilled. This substrate is then cleaned

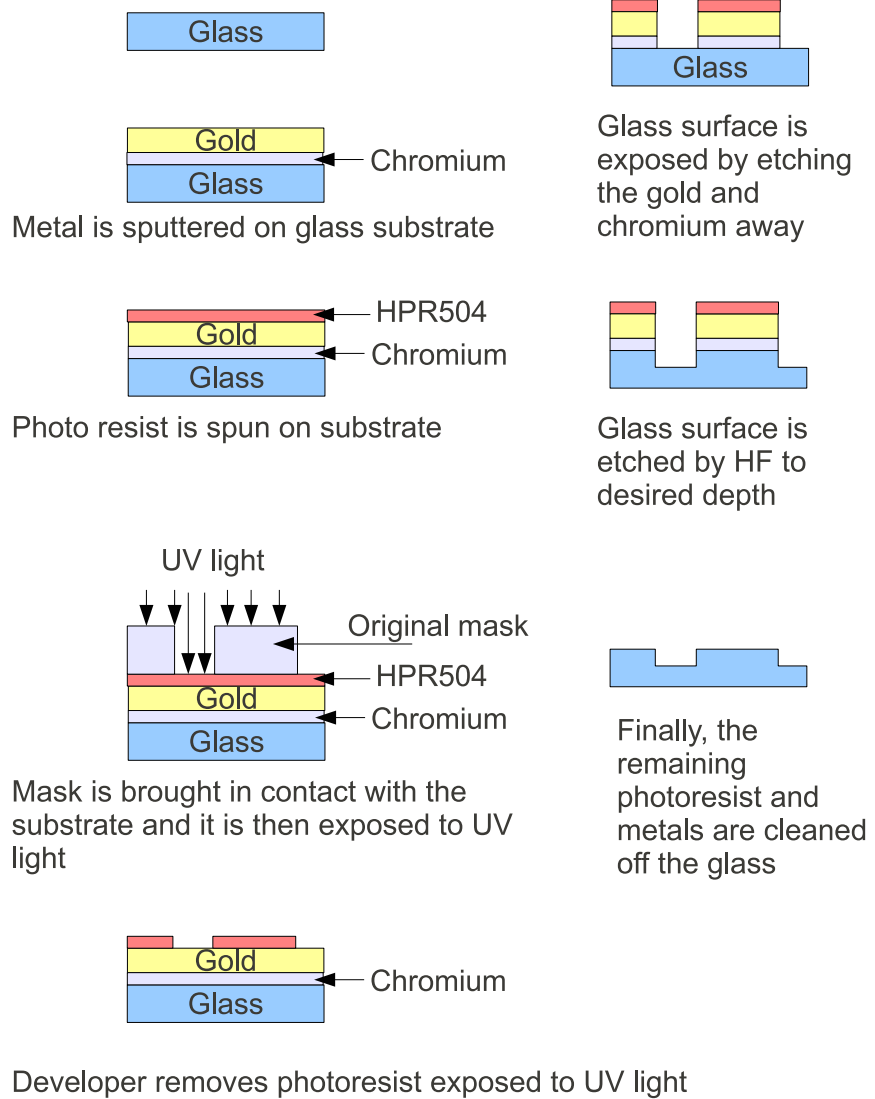


Figure A.1: Schematic outline of nanofabrication process used in digging gas path for capillaries into glass

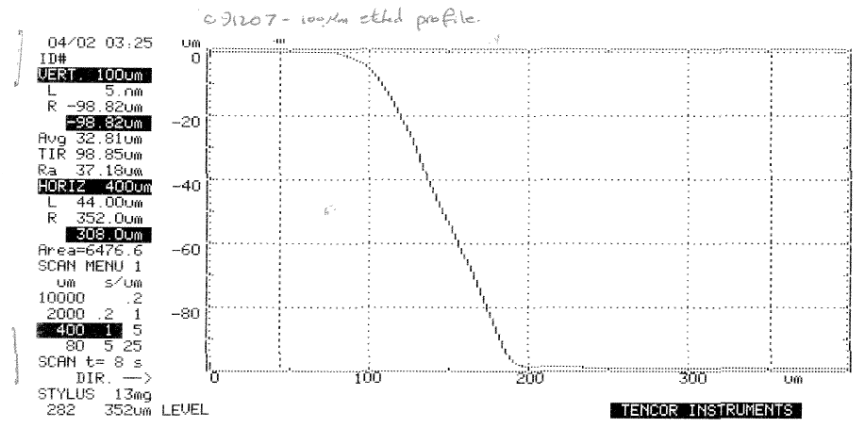


Figure A.2: Rising edge of glass channel after 100 micron was etch into the glass; dated 091207

in Piranha to make sure there is no organic residues left on it.

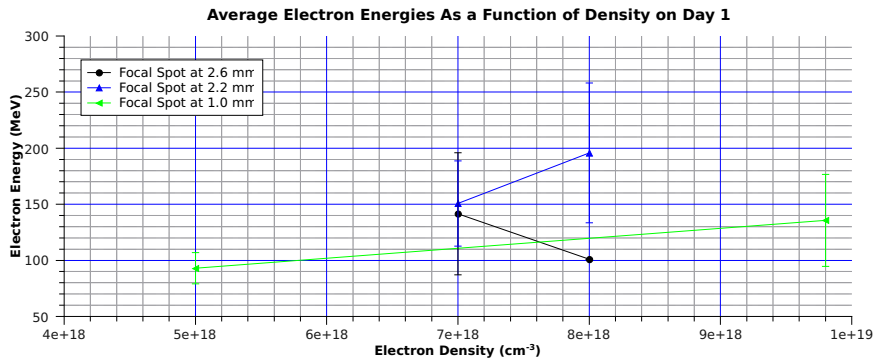
After both substrate pieces were completed, they were bonded together in the clean room. This was done by simply pushing the two together, where upon contact the two four inch pieces formed a weak bond which could be broken off by hand. To strengthen the bonds, the weakly bonded substrates were annealed in a muffle furnace where the temperature was increased to 600 °C gradually over an hour. The temperature was kept constant at 600 for two hours and left to cool to room temperature gradually.

Finally, the 4 inch square was cut into columns shown in Fig. 3.7 using a diamond saw. Five columns of waveguides resulted in this manner from each square, all having equal depths, but different lengths and widths.

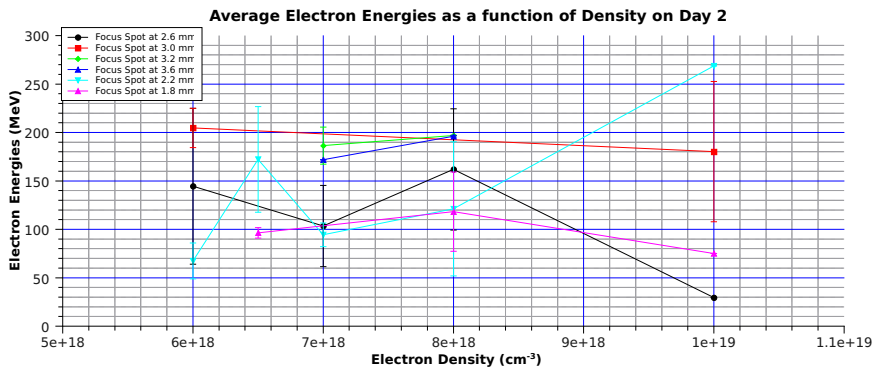
## Appendix B

# Electron Trends in Individually Grouped Parameters

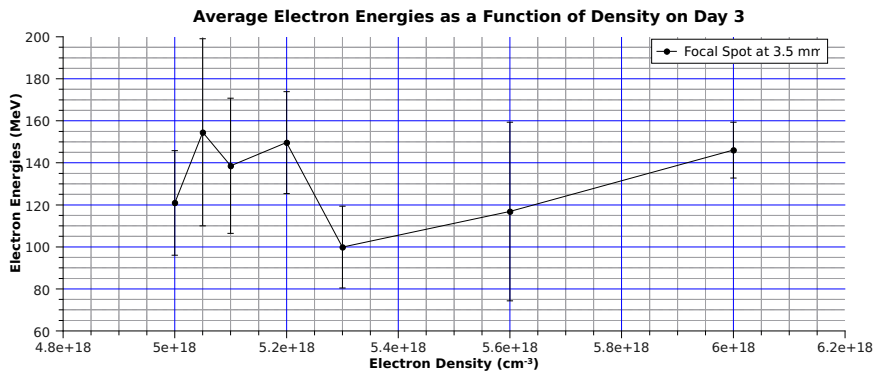
In chapter 5, the electron trends are shown as single graphs as functions of electron density or focus depth. This is in spite of the fact that electron density and focus depth were scanned simultaneously. The justification is that the electron energies for the parameter not being plotted against (e.g. focus depth in the case of a graph with x-axis being electron density) overlap. The justification is in this section. Figs. B.2 shows the average electron density for 5 mm gas jet with shots grouped for particular focus depths. Fig. B.1 shows the average electron densities as a function of focus depth for 5 mm gas jet target with shots grouped for particular electron densities. In all these images, a data point is the average energy and error bars are standard deviations of mean ( $\sigma_x/\sqrt{(N-1)}$  where  $\sigma_x$  is the standard deviation and N number of points).



(a)

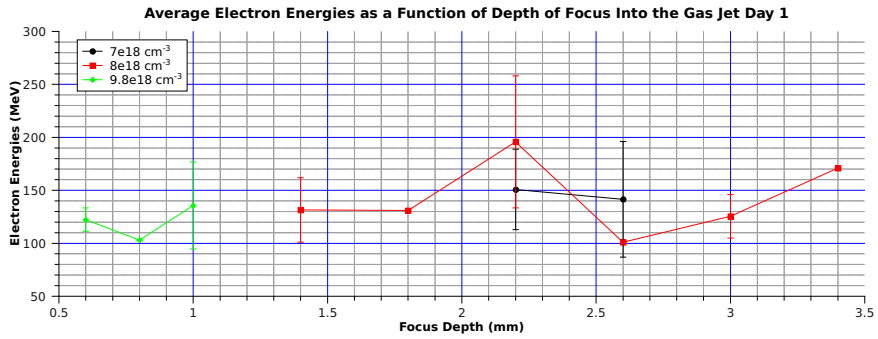


(b)

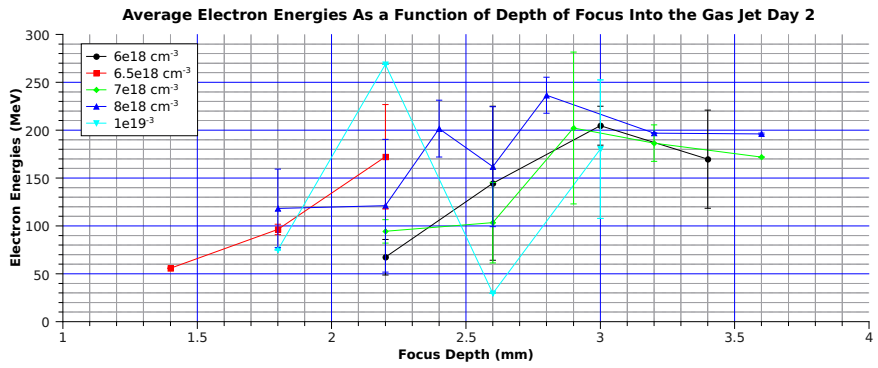


(c)

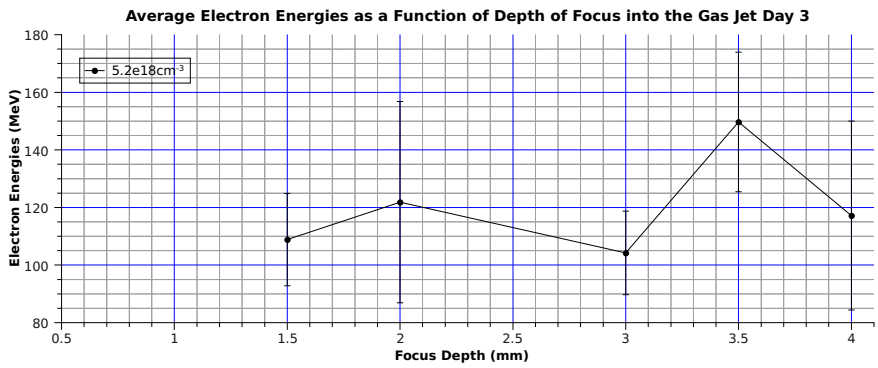
Figure B.1: Average electron density for 5 mm gas jet as a function of electron density for 100309, 100310, 100316 from top to bottom



(a)



(b)



(c)

Figure B.2: Average electron density for 5 mm gas jet as a function of focus depth for 100309, 100310, 100316 from top to bottom

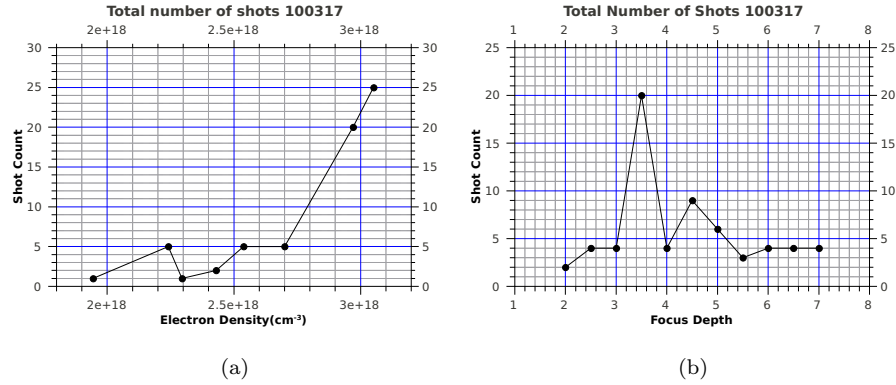
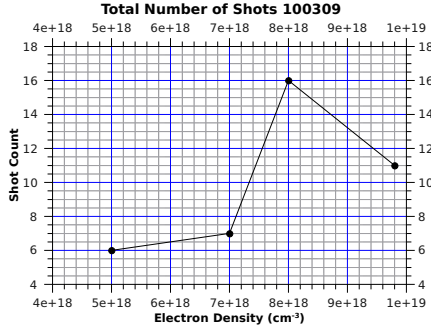
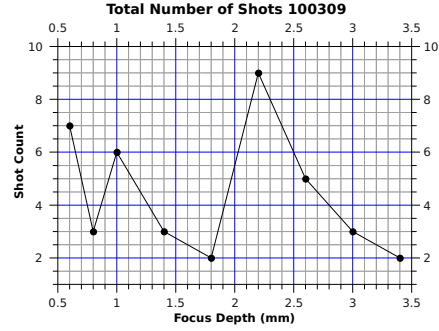


Figure B.3: Total number of shots for 100317 as a function of electron density (left) and focus depth (right)

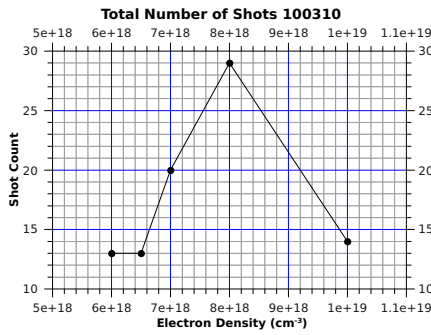
Additionally, number of shots for each experimental day as functions of the two key parameters are displayed in Figs. B.4 and B.3. In these numbers, like figures in chapter 5, the variables not under investigation are grouped together.



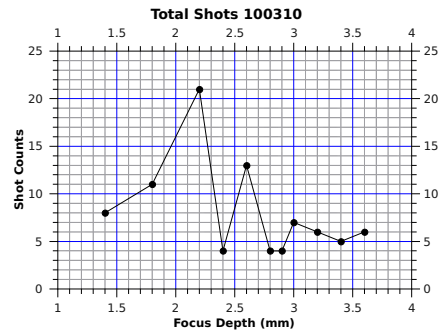
(a)



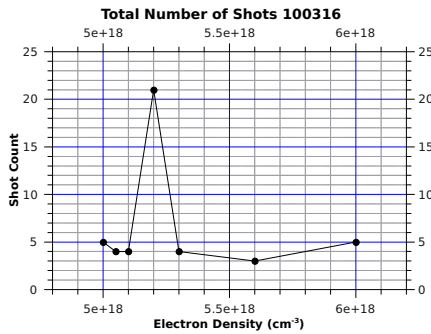
(b)



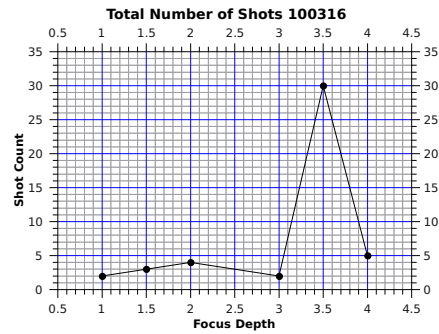
(c)



(d)



(e)



(f)

Figure B.4: Total number of shots for different days. The graphs for 100309, 100310, 100316 are shown from top to bottom. Figures on the left are plotted as a function of estimated electron density and on the right are plotted as focus depth

## Appendix C

### Shot Conditions of All

### Figures Used in Chapter 5

Relevant Figure	Shot number	Estimated $n_e$ [cm <sup>-3</sup> ]	Laser Power (TW)
5.3	100302_74	$2.1 \times 10^{19}$	77
5.6a	100302_74	$2.1 \times 10^{19}$	77
5.6b	100302_74	$2.1 \times 10^{19}$	77
5.7a	100316_90	$5.2 \times 10^{18}$	78
5.7b	100316_75	$5 \times 10^{18}$	77
5.7c	100316_36	$5.2 \times 10^{18}$	77
5.7d	100316_38	$5.2 \times 10^{18}$	77
5.9 left column	100316_33	$5.2 \times 10^{18}$	78
5.9 right column	100316_51	$5.1 \times 10^{18}$	76
5.10a	100310_065	$6.5 \times 10^{18}$	77
5.10b	100316_72	$5.3 \times 10^{18}$	76
5.11	100316_42	$6 \times 10^{18}$	76
5.14b	100316_63	$4.9 \times 10^{18}$	75
5.14c	100316_65	$4.9 \times 10^{18}$	76
5.14d	100316_66	$4.9 \times 10^{18}$	77
5.14e	100316_69	$5.3 \times 10^{18}$	76
5.14f	100316_70	$5.3 \times 10^{18}$	77
5.14g	100316_71	$5.3 \times 10^{18}$	75
5.14h	100316_72	$5.3 \times 10^{18}$	76
5.15a	100316_36	$5.2 \times 10^{18}$	77
5.15b	100316_88	$5.3 \times 10^{18}$	77
5.15c	100316_194	$5.5 \times 10^{18}$	77
5.18b	100311_31	$3.4 \times 10^{18}$	25
5.18c	100311_29	$3.4 \times 10^{18}$	35
5.18d	100311_26	$3.4 \times 10^{18}$	60
5.18e	100311_22	$3.4 \times 10^{18}$	70
5.18f	100311_20	$3.4 \times 10^{18}$	80
5.19c	100312_7	$2 \times 10^{18}$	78
5.19d	100312_83	$2 \times 10^{18}$	68
5.19e	100312_84	$2 \times 10^{18}$	69
5.19f	100312_29	$4 \times 10^{18}$	70
5.19g	100312_9	$6 \times 10^{18}$	75
5.19h	100312_67	$6 \times 10^{18}$	70
5.19i	100312_73	$8 \times 10^{18}$	68
5.19j	100312_78	$1 \times 10^{19}$	69
5.19k	100312_26	$4 \times 10^{18}$	72
5.21b	100319_20	He 30 psig	75
5.21c	100319_17	He 40 psig	76
5.21d	100319_24	He 58 psig	74
6.4	100310_110	$7 \times 10^{18}$	76

Table C.1: Conditions for different shots during the 100 TW experiment